

AD-A134 692

LASER DIAGNOSTIC DEVELOPMENT AND MEASUREMENT AND
MODELING OF TURBULENT FL. (U) DAYTON UNIV OH RESEARCH
INST L KRISHNAMURTHY ET AL JUN 83 UDR-TR-83-04

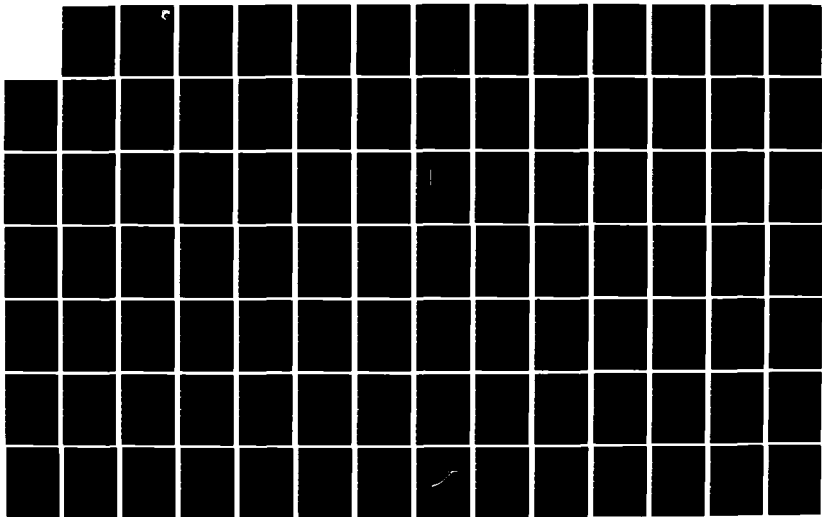
1/2

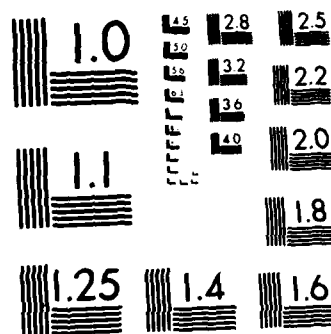
UNCLASSIFIED

AFWAL-TR-83-2044-PT-2 F33615-78-C-2005

F/G 20/4

NL





MICROCOPY RESOLUTION TEST CHART
NATIONAL BUREAU OF STANDARDS-1963-A

AFWAL-TR-83-2044
PART II

AD-A134 692



LASER DIAGNOSTIC DEVELOPMENT AND MEASUREMENT AND
MODELING OF TURBULENT FLOWFIELDS OF JETS AND WAKES

Part II
Numerical Predictions of Isothermal Flowfields
in a Ducted Centerbody Combustor

L. Krishnamurthy, S. O. Park, D. J. Wahrer, and H. S. Cochran
University of Dayton
Research Institute
Dayton, Ohio 45469

June 1983

FINAL REPORT FOR PERIOD 1 APRIL 1978 - 30 SEPTEMBER 1982

Approved for Public Release, Distribution Unlimited

AERO PROPULSION LABORATORY
AIR FORCE WRIGHT AERONAUTICAL LABORATORIES
AIR FORCE SYSTEMS COMMAND
WRIGHT-PATTERSON AIR FORCE BASE, OH 45433

T. e

OTIC FILE COPY

NOTICE

When Government drawings, specifications, or other data are used for any purpose other than in connection with a definitely related Government procurement operation, the United States Government thereby incurs no responsibility nor any obligation whatsoever; and the fact that the government may have formulated, furnished, or in any way supplied the said drawings, specifications, or other data, is not to be regarded by implication or otherwise as in any manner licensing the holder or any other person or corporation, or conveying any rights or permission to manufacture use, or sell any patented invention that may in any way be related thereto.

This report has been reviewed by the Office of Public Affairs (ASD/PA) and is releasable to the National Technical Information Service (NTIS). At NTIS, it will be available to the general public, including foreign nations.

This technical report has been reviewed and is approved for publication.

W. M. Roquemore
W. M. ROQUEMORE
Fuels Branch
Fuels and Lubrication Division
Aero Propulsion Laboratory

Arthur V. Churchill
ARTHUR V. CHURCHILL
Chief, Fuels Branch
Fuels and Lubrication Division
Aero Propulsion Laboratory

FOR THE COMMANDER

Benito P. Botteri
BENITO P. BOTTERI, Assistant Chief
Fuels and Lubrication Division
Aero Propulsion Laboratory

"If your address has changed, if you wish to be removed from our mailing list, or if the addressee is no longer employed by your organization please notify AFWAL/POSF, W-PAFB, OH 45433 to help us maintain a current mailing list".

Copies of this report should not be returned unless return is required by security considerations, contractual obligations, or notice on a specific document.

Unclassified

SECURITY CLASSIFICATION OF THIS PAGE (When Data Entered)

REPORT DOCUMENTATION PAGE		READ INSTRUCTIONS BEFORE COMPLETING FORM
1. REPORT NUMBER AFWAL-TR-83-2044, Part II	2. GOVT ACCESSION NO. A134692	3. RECIPIENT'S CATALOG NUMBER
4. TITLE and Subtitle Laser Diagnostic Development and Measurement and Modeling of Turbulent Flowfields of Jets and Wakes, Part II	5. TYPE OF REPORT & PERIOD COVERED Final Report for Period 1 Apr 1978 to 30 Sept 1982	
7. AUTHOR(s) L. Krishnamurthy, S. O. Park, D. J. Wahrer, and H. S. Cochran	6. PERFORMING ORG. REPORT NUMBER UDR-TR-83-04	
9. PERFORMING ORGANIZATION NAME AND ADDRESS University of Dayton Research Institute Dayton, OH 45469	8. CONTRACT OR GRANT NUMBER(s) F33615-78-C-2005	
11. CONTROLLING OFFICE NAME AND ADDRESS Aero Propulsion Laboratory (AFWAL/POSF) Air Force Wright Aeronautical Laboratories (AFSC) Wright-Patterson Air Force Base, Ohio 45433	10. PROGRAM ELEMENT PROJECT TASK AREA & WORK UNIT NUMBERS P.E. # 62203F, Proj. # 3048, W. U. # 30480596	
14. MONITORING AGENCY NAME & ADDRESS (if different from Controlling Office)	12. REPORT DATE June 1983	
	13. NUMBER OF PAGES 121	
	5. SECURITY CLASS. of this report Unclassified	
15a. DECLASSIFICATION DOWNGRADING SCHEDULE		
6. DISTRIBUTION STATEMENT (of this Report) Approved for Public Release, Distribution Unlimited		
17. DISTRIBUTION STATEMENT (of the abstract entered in Block 20, if different from Report)		
18. SUPPLEMENTARY NOTES Funding was provided from Program Element WU.30480596		
19. KEY WORDS (Continue on reverse side if necessary and identify by block number) Recirculating Flowfields Confined Turbulent Flows Isothermal Flows Coflowing Jets Bluff-Body Near Wake Numerical Predictions		
20. ABSTRACT (Continue on reverse side if necessary and identify by block number) Finite-difference numerical computations are presented to pre- dict the isothermal, turbulent, recirculating flowfields in a centerbody combustor configuration which involves confined dual coaxial jet mixing in the near-wake region of an axisymmetric bluff body. The calculations based upon the Reynolds-averaged Navier-Stokes equations and the k-ε turbulence model consider the influence of the annular and central flow rates on the nature of the flowfield downstream of the bluff body.		

DD FORM 1473

EDITION OF NOV 65 IS OBSOLETE

Unclassified

SECURITY CLASSIFICATION OF THIS PAGE (When Data Entered)

20. continued

The isothermal modeling calculations reported herein are performed with the "Teaching Elliptic Axisymmetrical Characteristics Heuristically" (TEACH) Code. Present calculations have employed the standard features of TEACH-type numerics; these include the use of primitive variables (velocity components and pressure) instead of the stream function-vorticity approach, "hybrid" upwind differencing, eddy-viscosity approach based upon the k- ϵ model, the Semi-Implicit Method for Pressure-Linked Equations (SIMPLE) algorithm for the pressure field, line-by-line relaxation and tri-diagonal matrix algorithm. Additional features that highlight the present calculations are the power-law differencing scheme which retains the diffusive effects for a larger cell-Peclet number range, viz., $-10 < Pe < 10$, than the "hybrid" upwind scheme; and the streamline-curvature correction in the k- ϵ model which involves a curvature-dependent (and thus nonconstant) c_μ (a parameter in the "standard" k- ϵ model having a value of 0.09). As part of the numerical investigations of the centerbody combustor flowfields, the predictions of the modeling without and with these additional features are compared.

Present numerical results show the influence of the annular and central jet flow rates on the distributions of the mean and rms velocity fields and the centerline locations of stagnation points. Moreover, the sensitivity of the predicted results to several aspects of the modeling is considered. These include the differencing schemes, inlet turbulence length scales, streamline curvature and k- ϵ model parameters.

The predicted results demonstrate the complex nature of the flowfield interactions in the near-wake region and refine the understanding of the centerbody combustor flowfields. The character of the recirculating flowfield emerging from the numerical predictions when the near-wake is dominated by the annular jet is in conformity with the experimental observations. In the reverse-flow region behind the bluff body, the present numerical results show good agreement with the recent velocity and concentration measurements and with the annular-jet data in the literature. Also, the results demonstrate that despite the complexity of the centerbody combustor flowfield, it belongs to a wider class of recirculating turbulent flowfields which obey certain similarity considerations for the mean axial velocity.

PREFACE

This final report was submitted by the University of Dayton, under Contract No. F33615-78-C-2005. The project was sponsored by the Air Force Wright Aeronautical Laboratories, Aero Propulsion Laboratory, Wright-Patterson Air Force Base, Ohio, under Project No. 3048, Task 05, Work Unit 96. Dr. William M. Roquemore, AFWAL/POSF, was Project Engineer. The program was managed by Dr. Eugene H. Gerber of the University. Dr. L. Krishnamurthy was Principal Investigator of the analysis task reported in this volume. This research task was initiated in October 1980 and completed in June 1982. This report was written by Dr. L. Krishnamurthy.

The Principal Investigator expresses his appreciation to:

- Dr. W. M. Roquemore, for fruitful discussions during this research;
- Dr. R. R. Craig, AFWAL/PORT, for making available a version of the TEACH-T computer program and for helpful discussions.
- Dr. S. O. Park, Mr. D. J. Wahrer, and Mr. H. S. Cochran, UDRI, for their technical contributions to the numerical modeling and computing activities;
- Ms. A. Kite, Ms. L. Knox, and Mr. M. Jones, UDRI, for preparing this report, and Ms. A. Cochran, UDRI, for technical editing.

Accession For	
NTIS GRA&I	<input checked="" type="checkbox"/>
DTIC TAB	<input type="checkbox"/>
Unannounced	<input type="checkbox"/>
Justification	
By	
Date	
Appr	
Dist	
A-1	

TABLE OF CONTENTS

SECTION		PAGE
1	Introduction	1
	1.1 Background	1
	1.2 Objectives	3
	1.3 Scope of Present Work	5
	1.4 Outline of Report	7
2	Governing Equations and Solution Procedure	9
	2.1 Differential Equations	9
	2.2 Turbulence Model	13
	2.3 Correction for Streamline Curvature Effect	16
	2.4 Finite-Difference Equations	19
	2.4.1 Exponential Scheme	25
	2.4.2 "Hybrid" Upwind Scheme	26
	2.4.3 Power-Law Differencing Scheme	23
	2.5 Boundary Conditions	29
	2.6 Solution Procedure	34
	2.6.1 Underrelaxation	35
	2.6.2 Convergence	36
3	Preliminary Numerical Computations	37
	3.1 APL Configuration	37
	3.1.1 Variations of Annular and Central Jet Flow Rates	39
	3.1.2 Sensitivity Tests	42
	3.1.2.1 Grid Independence of Solutions	42
	3.1.2.2 Influence of Inlet Velocity Profile	44
	3.1.2.3 Influence of Inlet Turbulence Parameters	44
	3.1.2.4 Influence of the Exit Boundary Location	47
	3.2 UCI Configuration	49
	3.2.1 Variations of Annular and Central Jet Flow Rates	49
	3.2.2 Sensitivity Tests	50
	3.2.2.1 Influence of σ_e	50
	3.2.2.2 Influence of c_u	51
	3.2.2.3 Other Effects	53
	3.3 Similarity Considerations	53
	3.3.1 Centerbody Combustor Configurations	54
	3.3.1.1 UCI Configuration	55
	3.3.1.2 APL Configuration	63
	3.3.2 Other Flowfield Configurations	65
	3.3.3 Species Concentration Fields	75

TABLE OF CONTENTS (Cont'd)

SECTION		PAGE
4	Refinements and Selected Results	79
	4.1 Influence of Differencing Schemes	79
	4.2 CO ₂ Mass Conservation	80
	4.3 Influence of Inlet Turbulence Length Scales Revisited	86
	4.4 Streamline Curvature Effects in Turbulence Modeling	93
	4.5 Comparison of Predictions with the Newer Experimental Results	98
	4.5.1 Centerline Variation of the Mean and rms Axial Velocity Fields	99
	4.5.2 Centerline Variation of CO ₂ Concentration	104
	4.5.3 Comparison of the Measured and Predicted Streamlines	107
5	Conclusions and Recommendations	113
	5.1 Conclusions	113
	5.2 Recommendations for Further Activity	116
	References	117

LIST OF ILLUSTRATIONS

FIGURE		PAGE
1	Computational Domain and Grid Point Distribution (Grid A)	20
2	Schematic of Computational Cell Structure	22
3	Influence of c_u on the Centerline Stagnation Points (UCI Combustor)	52
4	(a) - (g) Mean Axial Velocity Predictions for the (UCI) Centerbody Configuration	56-59
5	(a) - (f) Mean Axial Velocity Predictions for the (UCI) Centerbody Configuration	62-64
6	(a) - (c) Mean Axial Velocity Predictions for the (APL) Centerbody Configuration	66-67
7	Mean Axial Velocity Measurements ⁴³ for the (APL) Centerbody Configuration	68
8	Mean Axial Velocity Measurements ⁴² for the (Abramovich) Centerbody Configuration	69
9	Mean Axial Velocity Measurements ⁴⁴ for the Unconfined Annular Jet Around a Centerbody	71
10	(a) - (b) Mean Axial Velocity ⁴⁵ Measurements for the Unconfined Annular Jet Around a Disk	73-74
11	A Composite of all the Predicted and Measured Results	76
12	Radial and Axial Distributions of CO ₂ Mass Fraction	81
13	Axial Variation of the Computed Mass Flow Rates of Air and CO ₂	83
14	An Arbitrary Modification of the Grid with Increased Spatial Resolution in the Annular Region (GRID B)	85
15	The Relative Importance of Diffusion to the Total CO ₂ Mass Flow Rate at Different Axial Locations	87

LIST OF ILLUSTRATIONS (Cont'd)

FIGURE		PAGE
16	Centerline Forward and Rear Stagnation Points	90
17	Influence of Inlet Turbulence Length Scale and Curvature Correction on the Centerline Stagnation Points	92
13	Distribution of Curvature Corrected c_u	95
19	Effect of Streamline Curvature Correction on the Centerline Mean Axial Velocity Profiles	97
20	Centerline Mean and rms Axial Velocity Profiles for 2 kg/s Air Flow and Zero CO ₂ Flow	100
21	Centerline Mean and rms Axial Velocity Profiles for 2 kg/s Air Flow and 6 kg/hr CO ₂ Flow	101
22	Centerline Mean and rms Axial Velocity Profiles for 2 kg/s Air Flow and 16 kg/hr CO ₂ Flow	102
23	Centerline CO ₂ Mole Fraction for 2 kg/s Air Flow and 6 kg/hr CO ₂ Flow	105
24	Centerline CO ₂ Mole Fraction for 2 kg/s Air Flow and 16 kg/hr CO ₂ Flow	106
25	Streamline Contours for 2 kg/s Air Flow and Zero CO ₂ Flow	108

LIST OF TABLES

TABLE		PAGE
1	Governing Equations	12
2	Boundary Conditions	31
3	Specification of ϵ at the Inlet	33
4	Summary of Preliminary Computational Case Studies	39
5	Influence of Grid Spacings on (APL) Centerline Stagnation Distances	43
6	Influence of Inlet Velocity Profiles on (APL) Centerline Stagnation Distances	45
7	Influence of Inlet Turbulent Energies and Length Scales on (APL) Centerline Stagnation Distances	46
8	Influence of ALAMDA and TURBIN for 3 kg/hr CO ₂ Flow	48

LIST OF SYMBOLS

- a Coefficient for the combined convective and diffusive flux for the transport of any variable
- b Coefficients arising in the linearized form of the source term [see Eq. (14)]
- c Coefficients arising in the linearized form of the source term [see Eq. (14)]
- c_μ Constant equal to 0.09 in the "standard" k- ϵ model
- C Convective mass flux (= ρW in one-dimensional problem)
- C_1 Constant equal to 1.44 in the k- ϵ model
- C_2 Constant equal to 1.92 in the k- ϵ model
- D Diffusive mass flux (= $T/\delta z$ in one-dimensional problem), centerbody diameter
- f Mixture fraction
- H Stagnation enthalpy
- J Combined convective and diffusive flux [see Eq. (19)]
- k Turbulent kinetic energy [see Eq. (5)]
- K_1 Constants appearing in the expression for curvature-corrected (nonconstant) c_μ [see Eq. (13)]
- K_2 Constants appearing in the expression for curvature-corrected (nonconstant) c_μ [see Eq. (13)]
- λ_1 Turbulence length scale as per Eq. (7b)
- λ_2 Turbulence length scale as per Eq. (9b)
- \dot{m}_{air} Integrated mass flow rate of air per unit radian
- \dot{m}_{CO_2} Integrated mass flow rate of CO_2 per unit radian
- p Static pressure

P_{ij} Rate of production of the turbulent stress τ_{ij}
 [see Eq. (10)]

P_k Rate of generation of turbulence energy (see Table 1)

Pe Local cell Peclet number (see Paragraph 2.4.1)

r Radial coordinate in the cylindrical polar geometry

$r_{0.1}$ } Radial locations where the ratios of the difference
 $r_{0.5}$ } between the local and minimum mean axial velocities to
 $r_{0.9}$ } the difference between the maximum and minimum mean
 axial velocities are respectively equal to 0.1, 0.5
 and 0.9 (see Paragraph 3.3.1)

R_c Local radius of curvature of a streamline

R_j Radius of the central port

R_1 Radius of the Centerbody (see Figure 1)

R_2 Radius of the Confining Duct (see Figure 1)

S_ϕ Source term for the variable ϕ [see Eq. (1) and Table 1]

t_1 Time scale corresponding to the length scale λ_1 [see Eq. (3)]

u Fluctuating velocity component

U Mean radial velocity, general mean velocity

V Mean Azimuthal Velocity

V Control volume around the grid node P

W Mean Axial Velocity

x Coordinate distance [see Eq. (6)]

Y Mean species mass fraction

z Axial coordinate in the cylindrical polar geometry

α Constant equal to 1.5 appearing in the expression for the
 rate of production of the turbulent stress [see Eq. (10)]

β Constant equal to 0.6 appearing in the expression for the
 rate of production of the turbulent stress [see Eq. (10)]

Γ_ϕ	Effective exchange coefficient for the turbulent transport of the variable ϕ [see Eq. (2)]
δ	Characteristic reference length (see Table 3)
δ_{ij}	Kronecker delta [see Eq. (10)]
δz	Axial grid interval between adjacent nodal points
Δr	Normalized radial coordinate due to Abramovich ⁴² (see Paragraph 3.3.1)
ΔW	Normalized mean axial velocity due to Abramovich ⁴² (see Paragraph 3.3.1)
ϵ	Dissipation rate of turbulent kinetic energy [see Eq. (6)]
θ	Azimuthal coordinate in the cylindrical polar geometry
λ	Inlet turbulence length scale parameter appearing in Eq. (14) (FORTRAN variable ALAMDA)
μ	Absolute viscosity, molecular viscosity when not subscripted
ν	Kinematic viscosity
ρ	Mass density
σ_ϕ	Effective Prandtl/Schmidt number for variable ϕ [see Table 1 and Eq. (2)]
τ_w	Wall shear stress (arises in wall-function formulation for the specification of the boundary conditions in Paragraph 2.4)
ϕ	General dependent variable [see Eq. (1)]

SUBSCRIPTS

A	Annular jet exit plane, air
e	East face of the cell control volume
E	East nodal point
eff	Effective value
F	Central-jet exit plane, fuel

i	Index for axial computational nodes, components in orthogonal coordinate directions
in	Inlet plane of the computational domain
j	Index for radial computational nodes, components in orthogonal coordinate directions
n	North face of the cell control volume, coordinate normal to the streamline
N	North nodal point
O	Oxidant
P	General computational nodal point
s	South face of the cell control volume, coordinate along the streamline
S	South nodal point
t	Turbulent
w	West face of the cell control volume
W	West nodal point
ϕ	General dependent variable

SUPERSCRIPTS

—	Time-Mean value (Reynolds Averaging)
'	Fluctuating component (Reynolds Averaging)
*	Dependent variables to be pressure-corrected in the SIMPLE procedure (see Paragraph 2.6)

SECTION 1

INTRODUCTION

This three-part final report documents the research program performed for the Air Force Wright Aeronautical Laboratories, Aero Propulsion Laboratory, by the University of Dayton. The research had two overall objectives: (a) providing profile data that can be used to evaluate combustor and fuel combustion models and (b) evaluating the performance of combustor models and different diagnostic techniques in various combustion environments.

The technical efforts dealing with the design and development of a two-dimensional laser Doppler anemometer and the experimental data collected are described in Part I. The analysis and modeling tasks involving the numerical flowfield predictions and their comparisons with the experimental data are described in this volume, Part II. Part III describes the design, development and performance of a two-channel time-resolved laser Raman spectroscopy system.

1.1 BACKGROUND

The need to predict complex, recirculating turbulent flowfields in combustors under both nonreacting and reacting flow conditions has provided a strong incentive for the development of mathematical models and numerical procedures. These involve finite-difference calculations of the time-averaged Navier-Stokes equations and furnish the steady-state predictions of the flowfields. The predictive modeling activities have made use of several computer programs such as the "Field Relaxation Elliptic Procedure" (FREP) code¹ and the "Teaching Elliptic Axisymmetrical Characteristics Heuristically" (TEACH) code². Many of these modeling investigations have been directed at the centerbody combustor in operation at the Air Force Wright Aeronautical Laboratories, Aero Propulsion Laboratory (AFWAL/PO).³⁻⁸ The

availability of centerbody combustor experimental data from ongoing research programs, involving both intrusive and nonintrusive diagnostic techniques, has greatly facilitated the evaluation and validation of these computer codes.

The Aero Propulsion Laboratory (APL) centerbody combustor configuration represents confined dual coaxial jet mixing in the near-wake region downstream of a cylindrical bluff body. However, the interjet separation is much larger than that encountered in typical coaxial jet mixing, since the configuration involves an annular jet (flowing between the confining outer duct of 0.254 m diameter and the centerbody of 0.14 m diameter) and a central jet of 4.3×10^{-3} m diameter. This wide a separation between the jets and the concomitant presence of the bluff-body wake in the mixing region have not been encountered previously in numerical modeling. Thus, the APL configuration provides a stringent test to evaluate the predictive capability of several candidate modeling codes.

One such code that received considerable scrutiny with respect to the centerbody flowfield was the FREP code, which was evaluated in earlier modeling research studies sponsored by AFWAL/PO.³⁻⁵ One of these previous studies clearly established the complex nature of the near-wake flowfield interactions under different annular and central flow rates.⁵ The character of the centerbody flowfield emerging from the isothermal predictions when the near wake was dominated by the annular (air) jet or the central (CO₂) jet was found to conform to the APL experimental observations and with the heuristic flowfield descriptions suggested therefrom.⁹ Although the predicted results demonstrated the capability of the FREP code to provide qualitatively correct trends in the flowfield behavior, a comparison of the predictions with the measured velocity¹⁰ and the concentration¹¹ data revealed only fair to poor quantitative agreement. The major shortcoming of the FREP modeling which contributed to the poor agreement between the predicted and

measured results was known to be in the turbulence model. The numerical calculations⁵ had employed the obviously crude model which assumed a constant value of turbulent eddy viscosity, since the FREP code had encountered serious numerical difficulties with the well known two-equation ($k-\epsilon$) turbulence model.

The challenge inherent in the centerbody configuration and the availability of APL diagnostic data¹² thereon evoked the interest of a number of modelers (e.g., at AIRESEARCH,¹³ NASA-Lewis¹⁴ and Pratt and Whitney^{6,8}) in examining the centerbody configuration with their computer codes. These codes are based upon or variants of the TEACH program, originally developed by Gosman and Pun² and subsequently tested and validated by a number of investigators.¹⁵⁻¹⁹ Therefore, the TEACH code appeared to be an attractive candidate for use in our model validation studies with respect to the centerbody combustor flowfields. A version of the computer code, TEACH-T, was made available to us by the Aero Propulsion Laboratory, Ramjet Technology Branch (AFWAL/PORT).²⁰ Since this code contained an operational $k-\epsilon$ turbulence model, it became of interest to test this code for the centerbody configuration.

1.2 OBJECTIVES

The analysis task was concerned with providing the necessary theoretical framework for the interpretation of the diagnostic data on the velocity and concentration fields made available from the ongoing APL experimental program. This required numerical predictions of the flowfield variables (for both mean and fluctuating components) for various experimental conditions and their comparison with the experimental data. This procedure was also expected to facilitate the evaluation of the performance of combustor models and diagnostic techniques. The availability of computer programs that are reasonably successful in simulating

the desired flowfields was essential to the completion of the analysis task.

It was recognized at the outset that the FREP code was deficient in terms of the turbulence model and that recourse must be made to other finite-difference codes available in the public domain. The availability of the TEACH-T program from AFWAL/PORT essentially determined the course of the research program. Accordingly, the implementation of the analysis task was considered in terms of the following specific objectives:

- a. Modify the AFWAL/PORT version of the TEACH-T program for the centerbody combustor flowfield, make it operational, and verify its capability to predict the isothermal flowfields.

- b. Carry out performance assessments of the code through parameter optimizations, modifications and improvements, in comparison with other model predictions as well as experimental data.

- c. Provide the numerical predictions of the velocity and concentration fields for the desired experimental conditions.

The successful accomplishment of these objectives necessitated a close and continuous involvement with the APL experimental program. It is easy to recognize the need for such interaction for the comparison of model predictions with experimental data. In addition, the numerical modeling required input parameters appropriate for the desired experimental conditions. The selection of these input requirements (in terms of the geometric, fluid dynamic, and chemical parameters, and of the boundary conditions involving velocity, temperature, pressure, and species mass fractions) would have to be based upon data made available from the experimental program. Thus,

fulfillment of the above objectives depended on the timely availability of appropriate experimental data.

1.3 SCOPE OF PRESENT WORK

After a successful modification of the AFWAL/PORT version of the TEACH-T code for the centerbody combustor flowfield early in the program, preliminary computations of the isothermal mixing of 2 kg/s annular air flow and 2.22×10^{-3} kg/s (8 kg/hr) central CO₂ flow revealed numerous numerical instabilities, convergence failures, and nonphysical flowfield features. Since the code was written explicitly for the reacting-flow computations and also required the correct specifications of the excess air ratio to determine the air flow rate from the specified fuel flow rate, substantial changes were needed to employ the code for nonreacting calculations. Therefore, the initial phase of the modeling research was devoted to making the code operational for the isothermal predictions of the centerbody flowfields.

When the required changes were implemented in the code, the numerical computations were found to proceed smoothly, resulting in physically acceptable solutions. Converged results of the calculations for 2 kg/s air flow and several CO₂ flows (such as 1.11×10^{-3} , 2.22×10^{-3} , 3.33×10^{-3} , 4.44×10^{-3} , and 5×10^{-3} kg/s) were obtained and compared with the available experimental data on the velocity field.¹⁰ In addition, calculations were made for the extremely small CO₂ flow rate of 2.8×10^{-7} kg/s (1×10^{-3} kg/hr) and the results were considered to be a good approximation of those of the zero CO₂ flow rate case. (This approach was necessary since the initial programming of the code did not allow the specification of zero CO₂ flow rate.) These results were compared with the experimental data for zero CO₂ flow rate. These comparisons showed good qualitative agreement for the mean axial velocity and turbulence intensity profiles along the centerline. The quantitative agreement for the centerline locations of the stagnation points, however, was inadequate.

Investigation of the causes of this discrepancy required a series of sensitivity tests and optimization, since the modeling depended on a number of factors. These were the spatial resolution of the computational grid, the specifications of the inlet velocity profile, turbulence intensity and length scale, the prescription of the values of the constants in the turbulence model, and the specification of the location of the exit boundary of the computational domain. The last item is always arbitrary and subject to a trade off between the available computer resource and desirable solution accuracy. Therefore, the next phase of the modeling research examined the questions of parameter sensitivity and optimization.

Concurrent with the experimental program on the APL center-body combustor, investigations have been underway on a centerbody combustor of roughly 1/5-scale model of the APL configuration at the Combustion Laboratory of the University of California, Irvine (UCI).^{21,22} Since experimental data were becoming available for this combustor, it was of interest to obtain the numerical predictions thereon with the TEACH code. It was expected that such calculations would provide information on the question of combustor scaling (as between the large-scale APL and the small-scale UCI configurations). Moreover, these calculations also served to examine additional sensitivity tests and the question of similarity⁷ of the radial distribution of the mean axial velocity. Accordingly, these aspects represented another phase of the modeling research.

The sensitivity influence and parameter optimization did not appear to reduce the disparity between the predicted and measured¹⁰ centerline stagnation point locations. Moreover, while the model calculations⁶ at Pratt and Whitney also resulted in the underprediction of the forward stagnation point and the overprediction of the rear stagnation point, our results indicated greater degrees of under- and over-prediction. The search for an explanation of this somewhat disturbing anomaly led

to a reexamination of the influence of the inlet length scale and also to the question of incorporating a correction in the turbulence model to account for streamline curvature. These aspects formed the final phase of the modeling research within the scope of the present program.

The several phases of modeling research outlined above conformed to the first two specific objectives indicated in Paragraph 1.2. The AFWAL/PORT version of the TEACH code may now be said to be operating satisfactorily, with suitable parameter optimizations and improvements having been implemented. As seen in Section 4, the present status of our predictive modeling is good. However, the modeling research remains an ongoing activity, particularly with respect to the third objective. Extensive experimental data have become available recently from the UCI combustor.²³ These data as well as the isothermal LDA data of the APL combustor (seen in Part I of this report) necessitate further computational efforts for the comparisons with the numerical predictions. These additional computations would serve to examine the question of combustor scaling and help elucidate the distinctions between the small- and large-scale configurations.

1.4 OUTLINE OF REPORT

The governing equations and the solution procedure of the TEACH-T program are discussed briefly in Section 2. Aspects of the two-equation turbulence model, the numerical algorithms, convergence criteria etc. are highlighted in that section. In Section 3 the preliminary computational case studies are identified and the modeling details are discussed. The results of the refined computations are presented and discussed in Section 4. The numerical predictions are compared first with the earlier LDA data.¹⁰ These comparisons facilitated the implementation of a number of computational refinements. With the availability of the newer results documented in Part I, additional comparisons thereof with the computed results are

presented and the differences between the two sets of experimental data are noted. Finally, Section 5 outlines the conclusions of the present modeling research program and offers recommendations for further activity.

SECTION 2

GOVERNING EQUATIONS AND SOLUTION PROCEDURE

The numerical solution of a system of partial differential equations describing the conservation laws of mass, momentum, energy, and chemical species forms the basis of the predictive modeling of the turbulent, recirculating flowfields in the centerbody combustor configuration. This is accomplished in the TEACH code by a finite-difference computational procedure to solve the time-averaged Navier-Stokes equations. A brief discussion of the theoretical and computational aspects of the TEACH code is given below. Further details are available in References 2 and 15.

2.1 DIFFERENTIAL EQUATIONS

The TEACH-T computer program is written for steady-state flowfields in two-dimensional (planar or axisymmetric) geometries. The formulation entails an elliptic system of equations for properly describing the recirculating flows. The code has been extended by a number of investigators to apply to three-dimensional geometries and can also be easily modified to include parabolic flows. However, only the axisymmetric geometry and the elliptic formulation are of interest in the present program. Furthermore, since the present computations are concerned only with isothermal flowfields, the governing equations do not take the chemical source terms into account.

The numerical treatment of the Navier-Stokes equations in the TEACH code involves the primitive (pressure and velocity) variables instead of the stream function-vorticity formulation employed in the FREP code.¹ Therefore, a direct solution of the velocity and pressure fields cannot be avoided. The code uses a special procedure called the Semi-Implicit Method for Pressure-Linked Equations (SIMPLE)²⁴ algorithm to solve

explicitly for the velocity and pressure fields. Further details concerning the underlying theory and the computational procedure are available in References 15, 24 and 25.

For the axisymmetric configuration of interest here, we write the governing differential equations in the cylindrical polar coordinates. In view of the notation adopted in the APL experimental program, our present nomenclature for the coordinates and velocity components is different from that in the original TEACH code formulation.¹⁵ Thus \bar{U} , \bar{V} and \bar{W} are the time-mean velocity components in the radial (r), azimuthal (θ), and axial (z) directions. For the axisymmetric (in the mean) flowfield, the flow variables have no explicit dependence on θ and for the case of no swirl considered here, \bar{V} is zero. The governing equations for all the dependent variables can be expressed in the general form

$$\frac{1}{r} \left[\frac{\partial}{\partial r} (\bar{\rho} r \bar{U} \bar{\phi}) + \frac{\partial}{\partial z} (\bar{\rho} r \bar{W} \bar{\phi}) - \frac{\partial}{\partial r} (r \Gamma_{\phi} \frac{\partial \bar{\phi}}{\partial r}) - \frac{\partial}{\partial z} (r \Gamma_{\phi} \frac{\partial \bar{\phi}}{\partial z}) \right] = S_{\phi} \quad (1)$$

where $\bar{\phi}$ denotes any dependent variable (time-mean value). In Eq.(1) S_{ϕ} is the source term for the variable ϕ which includes true source terms (such as those due to chemical reactions) as well as the terms not covered by the first four terms (representing the convective and diffusive contributions). Γ_{ϕ} is the effective exchange coefficient for the transport of the variable ϕ and is given by

$$\Gamma_{\phi} = \mu_{\text{eff}} / \sigma_{\phi} \quad (2)$$

where μ_{eff} is the effective viscosity in the flowfield and σ_{ϕ} is the appropriate effective Prandtl/Schmidt number for each ϕ .

In a general formulation of the problem dealing with three-dimensional, reacting flowfields, the dependent variable ϕ denotes U, V, W , the stagnation enthalpy H , fuel mass fraction Y_F , oxidant mass fraction Y_O , mixture fraction f , turbulent kinetic energy k , its dissipation rate ϵ , the mean square fluctuations of concentrations (such as $\overline{f'^2}$, $\overline{Y_F'^2}$ and $\overline{Y_O'^2}$), and any other variable such as $\overline{Y_F'Y_O'}$ (e.g., see Reference 26). Present calculations, however, deal with the nonreacting flowfields (as arising in the turbulent mixing of the annular air stream and the central CO_2 stream in the centerbody configuration). Therefore, for the species conservation equation dealing with the variable \bar{Y}_F (which is now a passive scalar), the source term due to chemical reaction vanishes. For the energy conservation equation in the AFWAL/PORT version of the code, the dependent variable is the static enthalpy. For the isothermal flowfields under consideration here, it is not necessary to compute the static enthalpy or the temperature. Thus, the dependent variables of present interest are $\bar{U}, \bar{W}, \bar{\rho}, \bar{Y}_F, k$ and ϵ . The last two variables are discussed in detail in Paragraph 2.2. The appropriate values of σ_ϕ and the details of S_ϕ for the dependent variables of interest are shown in Table 1. The one remaining unknown variable is the pressure p , for which there is no additional governing equation. The SIMPLE algorithm²⁴ provides a special procedure for obtaining the pressure field in the TEACH code. Briefly, the momentum equations are first solved by estimating a pressure field, and then the computed velocity field is used to correct the pressure field by ensuring that the continuity equation is satisfied.

The effective viscosity μ_{eff} , appearing in Eq. (2) remains to be determined. In our formulation, μ_{eff} is the exchange coefficient for the transport of momentum in the turbulent flowfield. Thus, for the dependent variables \bar{U} and \bar{W} , Γ_ϕ is given by μ_{eff} , which is different from and much larger than the molecular viscosity μ of the fluid of interest. Since we deal with the

TABLE 1
GOVERNING EQUATIONS

Equation	$\bar{\rho}$	Γ_p	S_p
Continuity	1	0	0
Axial (Mean) Momentum	\bar{W}	μ_{eff}	$-\frac{\partial \bar{p}}{\partial z} + \frac{\partial}{\partial z} (\mu_{eff} \frac{\partial \bar{W}}{\partial z}) + \frac{1}{r} \frac{\partial}{\partial r} (r \mu_{eff} \frac{\partial \bar{U}}{\partial z})$
Radial (Mean) Momentum	\bar{U}	μ_{eff}	$-\frac{\partial \bar{p}}{\partial r} + \frac{\partial}{\partial z} (\mu_{eff} \frac{\partial \bar{W}}{\partial r}) + \frac{1}{r} \frac{\partial}{\partial r} (r \mu_{eff} \frac{\partial \bar{U}}{\partial r}) - \frac{2 \mu_{eff} \bar{U}}{r^2}$
Species (Passive Scalar) Mass Fraction	\bar{Y}_F	μ_{eff}/σ_F	0
Turbulence Kinetic Energy	k	μ_{eff}/σ_k	$P_k - \bar{\rho} \epsilon$
Turbulence Energy Dissipation	ϵ	$\mu_{eff}/\sigma_\epsilon$	$C_1 (\epsilon/k) P_k - C_2 \bar{\rho} \epsilon^2/k$

σ_F	σ_k	σ_ϵ	C_1	C_2
1	1	1.3	1.44	1.92

$$P_k \equiv \mu_{eff} \left\{ 2 \left[\left(\frac{\partial \bar{W}}{\partial z} \right)^2 + \left(\frac{\partial \bar{U}}{\partial r} \right)^2 + \left(\frac{\bar{U}}{r} \right)^2 \right] + \left(\frac{\partial \bar{W}}{\partial r} + \frac{\partial \bar{U}}{\partial z} \right)^2 \right\}$$

time-averaged equations, the process of time averaging introduces correlations of fluctuating velocity components as unknowns in the mean momentum equations. Also, the numerical solutions involve computational cell sizes that are much larger than the length scales of importance in the actual turbulent motion. The method of approximating the unknown correlations in terms of the known quantities gives rise to turbulence modeling. This aspect is discussed next.

2.2 TURBULENCE MODEL

The effective viscosity μ_{eff} appearing in Eq. (2) is expressed as the sum of the molecular (or the laminar) viscosity μ of the fluid and a turbulent eddy viscosity μ_t , i.e.,

$$\mu_{eff} = \mu + \mu_t. \quad (3)$$

The TEACH code employs the so-called two-equation turbulence model which relates μ_t to two scalar properties of turbulence, k and ϵ as

$$\mu_t = c_\mu \bar{\rho} k^2/\epsilon, \quad (4)$$

where c_μ is usually taken to be a constant equal to 0.09. The above procedure involves the introduction of two partial differential equations for k and ϵ which are solved together with the conservation equations for mass, momentum, and energy. We note that the inclusion of these additional equations has been anticipated in the general formulation of Eq. (1) and in Table 1. It is stressed here that the pressure fluctuations are not considered and that the source terms S_p for \bar{W} , \bar{U} , k , and ϵ in Table 1 are those appropriate for incompressible flow, since the AFWAL/PORT version of the code is explicitly written for that case. Therefore, overbars for ρ and p are superfluous. The

required modifications to compressible flow may be found in References 26 and 27.

Formally, the turbulence kinetic energy k is taken to characterize the intensity of turbulent fluctuations, i.e.,

$$k \equiv \overline{u_i u_i} / 2 \quad (5)$$

where u_i 's are the fluctuating velocity components in the three orthogonal directions. In Eq. (5) the familiar convention of summation on repeated indices is adopted. A number of authors have modeled the transport equation for k (see e.g., Launder and Spalding²⁸). The modeled equation appropriate for the axisymmetric geometry without swirl considered here is shown in Eq. (1) and Table 1.

The rate of viscous dissipation of turbulence kinetic energy is the second turbulence scalar of interest. For large Reynolds numbers, this variable may be defined as

$$\epsilon \equiv \nu \overline{\left(\frac{\partial u_i}{\partial x_j} \right) \left(\frac{\partial u_i}{\partial x_j} \right)} \quad (6)$$

where ν is the kinematic viscosity ($\equiv \mu/\rho$), the x_j 's are the distances along the coordinates r , θ and z , and the summation convention is used. The modeled form of the transport equation for ϵ given by Eq. (1) is that appropriate for high-Reynolds-number, axisymmetric recirculating flows without swirl.

The standard k - ϵ model discussed in the foregoing enables the calculation of the turbulent eddy viscosity through Eq. (4). However, the knowledge of k and ϵ alone does not describe the structure of the turbulence. Still it is possible to deduce some information on the characteristic length and time scales of

turbulence from k and ϵ . This procedure is facilitated by the use of the Prandtl-Kolmogorov relation,

$$\mu_t = c_\mu \bar{\rho} k^{1/2} \lambda_1 \quad (7a)$$

from which the length scale λ_1 is related to ϵ through Eq. (4) as

$$\lambda_1 = k^{3/2}/\epsilon. \quad (7b)$$

The corresponding time scale t_1 which is given by $\lambda_1/k^{1/2}$ is obtained from

$$t_1 = k/\epsilon. \quad (8)$$

The formulation illustrated by Eqs. (7a) and (7b) has found application in some earlier studies (e.g., see References 29 and 30). Often, instead of Eqs. (7), an alternative formulation is employed (e.g., see Reference 31), according to which

$$\mu_t = \bar{\rho} k^{1/2} \lambda_2 \quad (9a)$$

and

$$\lambda_2 = c_\mu k^{3/2}/\epsilon. \quad (9b)$$

We note that the AFWAL/PORT version of the TEACH Code employs the former formulation, while the recent calculations of Sturgess and Syed⁶ are based upon the latter formulation. An inspection of Eqs. (7) and (9) reveals that the length scales λ_1 and λ_2 differ by a factor of c_μ . This distinction must be taken into account when the inlet boundary condition for ϵ (see paragraph 2.4) is specified through the prescription of the inlet length scale. Indeed, this is the only circumstance when the length scale comes into play in the calculations, since μ_t is calculated by Eq. (4) for the distributions of k and ϵ obtained

by solving Eq. (1) and the set of Eqs. (7) or (9) is not directly involved in the computations.

2.3 CORRECTION FOR STREAMLINE CURVATURE EFFECT

It is well known that the streamline curvature has a strong influence on the shear-flow turbulence. This topic has been extensively discussed by Bradshaw,³² whose review of some experimental studies shows that the turbulent shear stress and the degree of anisotropy between the normal stresses are very sensitive to curvature. Numerical predictions of the size of the recirculation regions encountered in such turbulent recirculating flows as the centerbody and sudden expansion geometries also appeared to depend strongly on the turbulence activity in the curved shear layers bordering the recirculation region. The standard $k-\epsilon$ model discussed in Paragraph 2.2 does not account for streamline curvature effects. It can therefore be expected that this failure may be partly responsible for the discrepancy between the predicted and measured recirculation lengths.

Curvature modifications to the standard $k-\epsilon$ model have been attempted by a number of authors (e.g., see References 33 through 35). All these corrections are ad hoc, and their physical basis and range of applicability are open to doubt. Further research is needed to provide a more rigorous framework for the incorporation of curvature correction in the turbulence models. In our present program, however, we have introduced a curvature-dependent (and hence nonconstant) c_μ into the standard $k-\epsilon$ model, along the lines suggested by Leschziner and Rodi.³³ This modification is briefly described below.

The streamline curvature modification in Reference 33 is based upon the algebraic stress model of Gibson³⁶ which essentially consists of a set of algebraic equations resulting from the deletion of all transport terms in the differential equations

governing the transport of the Reynolds stresses.³⁷ These equations can be shown in a general form as

$$P_{ij} = \alpha \frac{\varepsilon}{k} (\overline{u_i u_j} - \frac{2}{3} \delta_{ij} k) + \beta (P_{ij} - \frac{2}{3} \delta_{ij} P_k) + \frac{2}{3} \varepsilon \delta_{ij} \quad (10)$$

where P_{ij} is the rate of production of the turbulent stress $\overline{u_i u_j}$, P_k (shown in Table 1) is the generation of turbulence energy by the interaction of mean velocity gradients and turbulence stresses, δ_{ij} is the Kronecker delta, and α and β are constants having the values of 1.5 and 0.6 respectively (as in Reference 37). With the assumption of local equilibrium of turbulence energy between production and dissipation (expressed by $P_k = \varepsilon$), Eq. (10) takes the simplified form

$$\frac{\overline{u_i u_j}}{k} = \frac{1-\beta}{\alpha \varepsilon} P_{ij} - \frac{2}{3} \frac{\delta_{ij}}{\alpha} (1-\alpha-\beta) . \quad (11)$$

Equation (11) reveals the effect of curvature on the stresses if (i,j) are taken as the streamline coordinates (s,n) where s is the coordinate along the streamline and n is the coordinate along the local normal to the streamline. Then P_{ij} becomes

$$P_{ss} = -2 \overline{u_s^2} \frac{\partial U_s}{\partial s} - 2 \overline{u_s u_n} \left(\frac{\partial U_s}{\partial n} + \frac{U_s}{R_c} \right) \quad (12a)$$

$$P_{nn} = -2 \overline{u_n^2} \frac{\partial U_n}{\partial n} + 4 \overline{u_n u_s} \frac{U_s}{R_c} \quad (12b)$$

$$P_{sn} = - \overline{u_n^2} \frac{\partial U_s}{\partial n} + (2\overline{u_s^2} - \overline{u_n^2}) \frac{U_s}{R_c} + \overline{u_n u_s} \frac{U_r}{r} . \quad (12c)$$

In Eq. (12) R_C is the local radius of curvature, r is the radial distance from the axis of symmetry (for the axially symmetric flow considered here) and U_s , U_n and U_r are respectively the velocity components along the s , n , and r directions. We can determine the stresses $\overline{u_n^2}$, $\overline{u_s^2}$ and $\overline{u_n u_s}$ from Eqs. (11) and (12) if the mean-velocity field, k , and ϵ are known or determinable. However, the shear stress $\overline{u_n u_s}$ is the dominant stress term in the momentum equations in a curved shear layer. Therefore, it would suffice to focus our attention on $\overline{u_n u_s}$, obtain an expression which relates this term to the respective rate of strain ($\partial U_s / \partial n + U_s / R_C$), and thereby extract a curvature-dependent c_μ . This result is shown as

$$c_\mu = - K_1 K_2 / [1 + 8 K_1^2 \frac{k^2}{\epsilon^2} (\frac{\partial U_s}{\partial n} + \frac{U_s}{R_C}) \frac{U_s}{R_C}] \quad (13)$$

where $K_1 \equiv (1-\beta)/\alpha$ and $K_2 \equiv (2/3) (1-\alpha-\beta)/\alpha$.

Equation (13) shows that c_μ is no longer a constant but is a function of streamline curvature. If the terms $\partial U_s / \partial n$ and U_s / R_C are known along with k and ϵ , c_μ is evaluated from Eq. (13). In Reference 33 $\partial U_s / \partial n$ and U_s / R_C are evaluated from \bar{W} , \bar{U} and their derivatives in z and r directions, as part of the main solution algorithm. These details are not included here.

Before we conclude this topic, it is worthwhile to emphasize the ad hoc nature of the c_μ correction derived here. According to the specified values of α and β , $K_1 K_2 = -0.13$. Thus, when Eq. (13) is used with the k - ϵ model and for negligible correction for curvature effects [the denominator in Eq. (13) approaches unity], c_μ reduces to 0.13, in contrast with the standard value of 0.09. To avoid this inconsistency, Reference 33 assumes $-K_1 K_2 / c_\mu = 1$ (instead of 1.5) in the actual calculations. But the value of $8 K_1^2$ in the denominator of Eq. (13) is determined from the specified values of α and β . This inconsistency clearly introduces

certain arbitrariness; as indicated in Reference 35, a more consistent approach would be to determine $8K_1^2$ from the condition $-K_1K_2 = 0.09$. Another feature in Eq. (13) that deserves comment is that c_u may become negative when $(\partial U_s / \partial n) / (U_s / R_c)$ is negative and sufficiently large in magnitude. This will be physically absurd in view of Eq. (4). Thus, the actual computational algorithm imposes an arbitrary positive lower bound on c_u . This aspect is discussed later in Paragraph 4.4.

2.4 FINITE-DIFFERENCE EQUATIONS

The differential equations describing the conservation laws are represented by Eq. (1). The solution of these equations is obtained numerically. This procedure consists of specifying a computational grid distribution for the flow domain, obtaining a set of finite-difference algebraic equations derived from discretizing the differential equations on all the grid nodes and solving the algebraic equations by standard numerical methods. The finite-difference equations can also be directly obtained from a control-volume analysis of the conservation laws (see Reference 15 for details). The accuracy of the numerical solution depends on how closely the set of finite-difference equations approximates the original differential equations. In general this is governed by the number of computational grid nodes which represent the flowfield.

Figure 1 shows the computational domain and the grid-point distribution initially adopted in the numerical calculations. The chosen grid consists of 41 axial nodes and 34 radial nodes, and viewed in the r - z plane, is regular and rectangular with nonuniform grid spacing in both axial and radial directions. As pointed out earlier, the location of the exit boundary is arbitrary and the present location of 30 cm from the face of the centerbody has been based upon extensive computational experience. To ensure adequate spatial resolution in flowfield

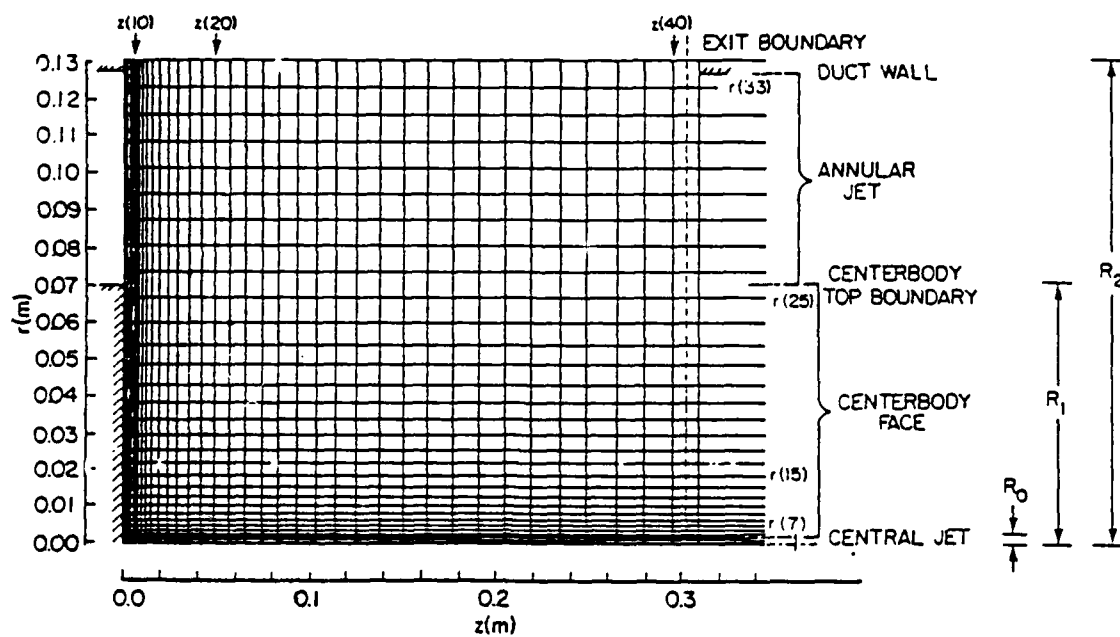


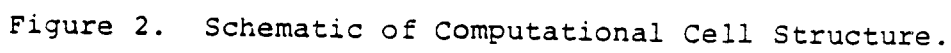
Figure 1. Computational Domain and Grid Point Distribution (GRID A).

regions with large gradients of the flow variables, the grid-point distribution is more densely populated toward the centerbody face and the axis of symmetry than toward the exit boundary and the duct wall. All the salient locations such as the axis of symmetry, the central-tube boundary, the centerbody top boundary and trailing face, duct wall boundary, and the exit-plane boundary are located midway between the adjacent grid nodes.

Figure 2 shows the schematic of the grid arrangement employed in the formulation of the finite-difference equations. All the dependent variables, except \bar{U} and \bar{W} , are referred to at the grid nodes (e.g., the node denoted by P). \bar{U} and \bar{W} are calculated at locations midway between the grid nodes, as illustrated by the dotted lines. In other words, a staggered-grid arrangement has been employed. This has the advantages of (a) evaluating the pressure gradients (which drive the velocities \bar{U} and \bar{W}) at the locations where the velocities are calculated and (b) determining the velocities where they are needed for the calculation of the convective fluxes into and out of each cell (viz., at the cell boundaries).

The set of finite-difference equations for Eq. (1), excluding the continuity equation which receives special treatment, is derived by integrating Eq. (1) over a control volume surrounding each grid node. This procedure requires appropriate assumptions to describe the relation between the nodal value ϕ_p , the rate of creation/destruction of ϕ within the control volume, and the transport of convective and diffusive fluxes of ϕ across the boundaries of the control volume. The source term S_ϕ in Eq. (1) (see Table 1 for the form of S_ϕ for various dependent variables) can be represented in a linearized form as

$$\int_V S_\phi dV = b \phi_p + c \quad (14)$$



where the control volume around the grid node P is denoted by V . In Eq. (14) b and c are in general functions of ϕ . The representation of the convective and diffusive fluxes requires some elaboration, especially since present research has implemented some improvements in the original formulation of the TEACH code. We discuss this aspect in detail later but indicate now the general form which represents Eq. (1), after the flux values at the control volume faces are approximated in terms of ϕ values at the neighboring nodes. For the control volume under consideration we have

$$(a_p - b) \phi_p = \sum_n a_n \phi_n + c, \quad (15)$$

where $a_p = \sum_n a_n$, \sum_n denotes the summation over the neighboring nodes N, E, S and W, and the a_n 's and ϕ_n 's are respectively a_N, \dots, a_W and ϕ_N, \dots, ϕ_W . Note that the a_n 's represent the coefficients for the combined convective and diffusive fluxes of ϕ .

Equations similar to Eq. (15) can be written for each of the dependent variables ϕ at every node P in the interior of the computational domain. Appropriate modifications to the expressions for the fluxes are necessary when the nodes adjoining the boundaries of the domain are encountered (see Paragraph 2.5). The resulting system of equations can be solved for the unknown ϕ by an iterative procedure, if the needed boundary data are available. A brief discussion of the boundary conditions is presented in Paragraph 2.5. The iterative procedure yields an acceptable solution when a certain convergence criterion is satisfied. Although this question is considered when we discuss

the solution algorithms in Paragraph 2.6, we point out that a sufficient condition for convergence for each p is that

$$|a_p - b| > \sum_n |a_n| \quad (16a)$$

for all equations, and

$$|a_p - b| > \sum_n |a_n| \quad (16b)$$

for at least one equation. These conditions are satisfied if all the a_n 's are positive (since $\sum a_n = a_p$) and b is negative. The latter requires that the linearization in Eq. (14) be such that b is negative.

The pressure field is determined from an equation obtained by combining the continuity and momentum equations. This procedure yields a finite-difference pressure-correction equation similar to Eq. (15), with c now representing the local mass imbalance in the prevailing velocity field.

We now return to the question of evaluating the convective and diffusive fluxes of p . Following is a discussion of differencing schemes.

The derivation of the fluxes in the TEACH code can be better understood by considering the steady, one-dimensional equation for the convection-diffusion balance described by

$$\frac{d}{dz} (\rho W \phi) = \frac{d}{dz} \left(\Gamma \frac{d\phi}{dz} \right) \quad (17)$$

Applying this to the one-dimensional grid points and control volume, we obtain

$$(\rho W \phi)_e - (\rho W \phi)_w + \left(\Gamma \frac{d\phi}{dz} \right)_w - \left(\Gamma \frac{d\phi}{dz} \right)_e = 0, \quad (18)$$

where the subscripts e and w respectively denote east and west faces of the control volume. If ϕ and $d\phi/dz$ are expressed at control volume faces in terms of the nodal values of ϕ , i.e., ϕ_w , ϕ_p and ϕ_E , Eq. (18) leads to the algebraic equation for the unknown ϕ_p , given by Eq. (15).

2.4.1 Exponential Scheme

A good starting point of the face-value approximation is an analytical solution of Eq. (17), which is easily obtained when $\rho W = \text{constant}$ and $\Gamma = \text{constant}$. Applying the analytical solution to the intervals E-P and W-P, we obtain the fluxes into the right and left boundaries of the control volume, given respectively by,³⁸

$$J_e = (\rho W \phi - \Gamma \frac{d\phi}{dz})_e = (\rho W)_e \left\{ \phi_p + (\phi_p - \phi_E) / [\exp(Pe_e) - 1] \right\}; \quad (19a)$$

and

$$J_w = (\rho W \phi - \Gamma \frac{d\phi}{dz})_w = (\rho W)_w \left\{ \phi_w + (\phi_w - \phi_p) / [\exp(Pe_w) - 1] \right\}, \quad (19b)$$

where Pe_e and Pe_w are the local Peclet numbers. These are defined as $Pe_e \equiv (\rho W)_e (\delta z_{PE}) / \Gamma_e$ and $Pe_w \equiv (\rho W)_w (\delta z_{WP}) / \Gamma_w$ (δz denotes the axial grid interval between adjacent nodes). Note that for nonuniform ρ and Γ , average values must be used. Expressing the local Peclet numbers in terms of the convective and diffusive coefficients $C \equiv \rho W$ and $D \equiv \Gamma / \delta z$, we obtain $Pe_e = C_e / D_e$ and $Pe_w = C_w / D_w$. Through the use of Eqs. (19) and the foregoing definitions, Eq. (18) can be cast as

$$a_p \phi_p = a_E \phi_E + a_w \phi_w, \quad (20)$$

where $a_E \equiv C_e / [\exp(Pe_e) - 1]$, $a_w \equiv C_w \exp(Pe_w) / [\exp(Pe_w) - 1]$ and $a_p \equiv a_E + a_w$. In obtaining the last identity, use is made of the equality $C_e = C_w$ in view of the one-dimensional mass conservation. Note that Eq. (20) is just the one-dimensional analog of Eq. (15), without the source terms $b_p + c$.

The foregoing development describes the exponential scheme for the one-dimensional problem where it provides the exact solution. In spite of its highly desirable features, however, the exponential scheme has not been widely used in numerical computations, because the exponentials are expensive to compute. Moreover, the scheme does not apply exactly in two- or three-dimensional situations, and for nonzero source terms. Therefore, the extra computational expense inherent in the exponential scheme does not justify its extension to the two-dimensional problem at hand.

2.4.2 "Hybrid" Upwind Scheme

Accordingly, the developers of the TEACH code have exploited a "hybrid" differencing scheme, in which the face values of the fluxes are approximated as follows:³⁹

$$\begin{aligned}
 J_w &= \begin{cases} (C_w/2 + D_w) \phi_W + (C_w/2 - D_w) \phi_P, & \text{for } -2 < Pe_w < 2 \\ C_w \phi_W, & \text{for } Pe_w > 2 \\ C_w \phi_P, & \text{for } Pe_w < -2 \end{cases} \\
 J_e &= \begin{cases} (C_e/2 + D_e) \phi_P + (C_e/2 - D_e) \phi_E, & \text{for } -2 < Pe_e < 2 \\ C_e \phi_P, & \text{for } Pe_e > 2 \\ C_e \phi_E, & \text{for } Pe_e < -2 \end{cases} \quad (21)
 \end{aligned}$$

We note that in obtaining Eq. (21), the exponentials in Eqs. (19) have been approximated by piece-wise linear representations. The resulting expressions for the fluxes in Eq. (21) correspond to the central differencing when $-2 < Pe < 2$ and the upwind differencing (with the diffusive contributions being neglected) when $|Pe| > 2$, thus the designation "hybrid." In terms of the

standard formulation of Eq. (20), the coefficients for the combined convective and diffusive fluxes in the "hybrid" upwind scheme become

$$a_E = \begin{cases} D_e - C_e/2, & \text{for } -2 < Pe_e < 2 \\ 0, & \text{for } Pe_e > 2 \\ -C_e, & \text{for } Pe_e < -2 \end{cases}$$

and

$$a_W = \begin{cases} D_w + C_w/2, & \text{for } -2 < Pe_w < 2 \\ C_w, & \text{for } Pe_w > 2 \\ 0, & \text{for } Pe_w < -2. \end{cases}$$

A comparison of the exponential scheme and the "hybrid" upwind scheme is given by Patankar⁴⁰ in graphic form. This comparison is better facilitated by the introduction of the nondimensional coefficients a_E/D_e and a_W/D_w . We obtain

$$a_E/D_e = Pe_e / [\exp(Pe_e) - 1] \quad (22a)$$

for the exponential scheme and

$$a_E/D_e = \begin{cases} 1 - Pe_e/2, & \text{for } -2 < Pe_e < 2 \\ 0, & \text{for } Pe_e > 2 \\ -Pe_e, & \text{for } Pe_e < -2 \end{cases} \quad (22b)$$

for the "hybrid" upwind scheme.

The use of the "hybrid" upwind differencing scheme has been generally accepted by the TEACH-code modelers and little loss of accuracy has been claimed in following this scheme. It should be noted, however, that the "hybrid" scheme yields, according to Eq. (22b), a value of 0 at $Pe_e = 2$ and a value of 2 at $Pe_e = -2$ for a_E/D_e . The exact values from the exponential scheme, according to Eq. (22a), are respectively 0.3130 and 2.313. Thus, at $|Pe_e| = 2$ the departure of the "hybrid" upwind solution from the exact (exponential) solution of the one-dimensional convection-diffusion equation is rather large.⁴⁰ Furthermore, it is clearly arbitrary to neglect the diffusion effects as soon as $|Pe|$ exceeds 2 [(see Eq. (21)].

2.4.3 Power-Law Differencing Scheme

A better approximation to the exact solution has been obtained by the power-law differencing scheme, which is described in Patankar.⁴¹ A comparison of the "hybrid" upwind and power-law schemes in Reference 40 shows that the solutions become identical for $|Pe| > 10$. For example, the nondimensional coefficient a_E/D_e for power-law scheme is given by

$$a_E/D_e = \begin{cases} -Pe_e, & \text{for } Pe_e < -10 \\ (1+0.1 Pe_e)^5 - Pe_e, & \text{for } -10 < Pe_e < 0 \\ (1-0.1 Pe_e)^5, & \text{for } 0 < Pe_e < 10 \\ 0, & \text{for } Pe_e > 10 \end{cases} \quad (22c)$$

From Eq. (22c) it is obvious that the power-law scheme solutions are much closer to the exponential-scheme solutions than the "hybrid" upwind solutions, for $-10 < Pe_e < 0$ and for $0 < Pe_e < 10$. We noted earlier that at $|Pe_e| = 2$, the "hybrid" upwind solution is the farthest from the exponential solution. On the other hand, Eq. (22c) yields that a_E/D_e is 2.328 at

$Pe_g = -2$ and is 0.3277 at $Pe_g = 2$. Thus, the power-law scheme provides an extremely good representation of the exponential behavior for the Peclet-number range where the "hybrid" scheme is not satisfactory.

From the foregoing comparisons, it appears that for the one-dimensional diffusion-convection equation the power-law scheme is superior to the "hybrid" upwind scheme. Moreover, the diffusive effects are retained in the power-law scheme for a larger Peclet-number range, viz., $|Pe| < 10$. In view of these advantages and since the power-law expressions are not particularly expensive to compute, we have employed the two-dimensional extension of the power-law scheme (due to Patankar⁴⁰) in our calculations with the TEACH code. As part of our numerical computations of the centerbody combustor flowfields, we have compared the predictions of the "hybrid" upwind and power-law schemes. This aspect is discussed in Section 4.

2.5 BOUNDARY CONDITIONS

The solution of Eq. (1) requires the specification of appropriate boundary conditions for each of the dependent variables. Since the governing equation is elliptic, the boundary conditions must be prescribed on all the boundaries of the computational domain shown schematically in Figure 1. Note that because of symmetry only the top half of the centerbody combustor configuration is represented by the computational domain.

The top boundary of the computational domain is the duct wall and the bottom boundary is the axis of symmetry. The left boundary represents the inflow boundary and consists of the annular air inlet, the centerbody face, and the central fuel inlet. The right boundary is the outflow boundary, the location of which is unknown a priori. Therefore, the specification of

the location of this boundary is essentially arbitrary and, as discussed in Section 1, it is essential to ensure that the sensitivity of the computed solutions to the specification of this boundary location is not significant.

The boundary conditions selected in our computations are shown in Table 2. Some general observations can be made with respect to the conditions at the four boundaries. Along the bottom boundary representing the centerline, symmetry considerations require that $\partial \bar{p} / \partial r = 0$ for all \bar{p} ; in addition, because of symmetry, the radial velocity \bar{U} vanishes on the centerline. Along the top boundary representing a rigid impermeable wall, the velocity components are set equal to zero (due to the no-slip requirement on \bar{W} and the nonmoving wall for \bar{U}). However, to minimize the computer storage and run time, the dependent variables at the wall are linked to those at the grid node adjacent to the wall by equations which are consistent with the logarithmic law of the wall. For the tangential velocity (\bar{W} in this case), this results in a condition on the wall shear stress τ_w in the calculations. Wall-function formulations also govern the boundary conditions of k and ϵ . For the species mass fraction \bar{Y}_F , the impermeable boundary requires the normal derivative ($\partial \bar{Y}_F / \partial r$ at the top boundary) to vanish. In the code's finite-difference formulation, this is accomplished through setting the coefficient a_N to zero for the cell whose north boundary coincides with the top boundary. Along the left boundary, similar considerations apply to the rigid impermeable boundary representing the centerbody face: for the \bar{U} velocity the law of the wall is employed to express τ_w . For k and ϵ the wall functions are used. The vanishing of $\partial \bar{Y}_F / \partial z$ along this boundary is implied by setting the coefficient a_W to zero for the cells with the west boundaries coinciding with the centerbody face. Along the inlet ports in the left boundary, the conditions are specified through experimental measurements. The inlet profiles of

TABLE 2
BOUNDARY CONDITIONS

$\bar{\phi}$	Top Boundary (Duct Wall)	Bottom Boundary (Axis of Symmetry)	Left Boundary		Right Boundary (Outflow)
			Inlets	Centerbody Face	
\bar{W}	Law of the Wall to Relate the Wall Shear Stress τ_w	$\frac{\partial \bar{W}}{\partial r} = 0$	\bar{W} Specified = W_{in}	$\bar{W} = 0$	Overall Mass Conservation
\bar{U}	$\bar{U} = 0$	$\bar{U} = 0$	$\bar{U} = 0$	Law of the Wall to Relate the Wall Shear Stress τ_w	$\frac{\partial \bar{U}}{\partial z} = 0$
\bar{Y}_F	$\frac{\partial \bar{Y}_F}{\partial r} = 0$	$\frac{\partial \bar{Y}_F}{\partial r} = 0$	\bar{Y}_F Specified (1 for Central and 0 for Annular Inlets)	$\frac{\partial \bar{Y}_F}{\partial z} = 0$	$\frac{\partial \bar{Y}_F}{\partial z} = 0$
k	Given by Wall Functions	$\frac{\partial k}{\partial r} = 0$	k Specified = (TURBIN)(W_{in}) ²	Given by Wall Functions	$\frac{\partial k}{\partial z} = 0$
ϵ		$\frac{\partial \epsilon}{\partial r} = 0$	ϵ (see Table 3)		$\frac{\partial \epsilon}{\partial z} = 0$

\bar{W} are obtained from experiments. For well-designed inlets, the radial velocity \bar{U} is typically close to zero. Any nonzero radial velocity distribution, if specified, must satisfy the continuity equation at the inlet. The inlet distributions of species mass fraction \bar{Y}_F are usually assumed to be uniform across the respective (central) fuel and (annular) oxidant ports.

The distributions of k and ϵ remain to be specified at the inlet. The specification of k entails the prescription of appropriate value of the parameter TURBIN (FORTRAN variable in the TEACH code). The inlet profile of k is obtained from

$$k = \text{TURBIN} \times \bar{W}_{in}^2, \quad (23)$$

where \bar{W}_{in} denotes the mean axial velocity at the inlet. A value of 0.03 is considered typical for TURBIN. Note that experimental data on the turbulence intensity measurements in the inlet provide a basis for selecting the appropriate value of TURBIN. Of course, in the absence of the turbulence intensity measurements in all three orthogonal coordinate directions, recourse must be made to the assumption of isotropy in determining k from the turbulence intensity results in one or two directions.

The specification of the inlet distributions of ϵ is not yet possible from the measurement of the dissipation rate. As discussed in Paragraph 2.2, it becomes necessary to introduce certain assumptions on the turbulence length scale in the inlet. Depending on the choice of the length scale λ_1 [see Eq. (7b)] or λ_2 [see Eq. (9b)], appropriate values of the parameter λ (denoted by the FORTRAN variable ALAMDA in the TEACH code) must be selected. Table 3 shows some examples of the length scales used by different authors. It is clear that the length scales in different flow configurations differ considerably. This observation should hardly be surprising, since no single length scale of turbulence can be expected to represent all types of turbulent

TABLE 3
SPECIFICATION OF ϵ AT THE INLET

AUTHOR	FLOW GEOMETRY	CHARACTERISTIC LENGTH	LENGTH SCALE l_1 or l_2 $= \lambda \cdot \delta$	ϵ
Sturgess and Syed ⁶	Centerbody Combustor	$\delta = R_2 - R_1$ (see Figure 2)	$l_2 = 0.03\delta$	$c_p k^{3/2} / l_2$
Leschziner and Rodi ³³	Unconfined Jet	$\delta = \text{Jet HalfWidth}$	$l_1 = 0.56\delta$	$k^{3/2} / l_1$
Humphrey and Pourahmadi ³⁴	Pipe Flow	$\delta = \text{PipeDiameter}$	$l_1 = 0.01\delta$	$k^{3/2} / l_1$
Krishnamurthy and Park (Present Work)	Centerbody Combustor	$\delta = R_2 - R_1$	0.3333δ $l_1 = 0.5556\delta$	$k^{3/2} / l_1$

flows. What is crucially important, however, is to determine how strongly the flowfield predictions depend on the inlet length scale. Our numerical results discussed in Sections III and IV address this question.

For the centerbody configuration, the rate of dissipation at the inlet is given by Eq. (7b), with the length scale l_1 given by

$$l_1 = \lambda \delta, \quad (24)$$

where δ is a characteristic reference length (see Table 3). For the central port, the reference length is the tube radius R_0 . For the annular port, the reference length is the so-called hydraulic mean radius which is given by $R_2 - R_1$, where R_2 is the duct radius and R_1 is the centerbody radius. We note that the value of 0.03 for λ used by Sturgess and Syed⁶ corresponds to a value of 0.3333 when Eqs. (7a) and (7b) are used (as in the present study) instead of Eqs. (9a) and (9b).

2.6 SOLUTION PROCEDURE

Writing Eq. (15) for each node in the domain of our interest, systems of algebraic equations for each dependent variable ϕ are obtained. The resulting large nonlinear coupled systems naturally require an iterative solution procedure. This involves:

- (a) solving the system of equations for one dependent variable with linearization (inner iteration), and
- (b) connecting properly the inner iteration for all ϕ 's until the converged solution is obtained (outer iteration).

The outer iteration loop consists of the following sequence:⁴⁰

- (a) guess the pressure field p ,
- (b) solve the momentum equations to obtain W^* , U^* ,
- (c) solve the pressure correction equation (based on mass conservation) to obtain the correction to the pressure field,
- (d) update W^* and U^* based on the pressure correction and update p^* to get W , U , and p ,
- (e) solve the systems for other ϕ 's,
- (f) treat ϕ as p^* and return to step (b), and repeat the whole procedure until convergence is achieved.

The inner iteration loop employs a line-by-line solution procedure, for which the well known Tri-diagonal Matrix Algorithm (Thomas Algorithm) is used. For each ϕ , the number of sweeps is specified. One sweep is composed of an east-west sweep and a north-south sweep. The number of sweeps for each variable ϕ is set in the main program by the user.

Currently, the number of sweeps for pressure correction is set at 4, while that of all the other variables is set at 2.

It should be noted that the specification of large number of sweeps is not desirable, since the solution is only tentative after all.

2.6.1 Underrelaxation

Underrelaxation is usually employed for nonlinear problems to avoid divergence in the iterative solution process.

For all the dependent variables other than pressure, the underrelaxation comes through the modification of the coefficients of Eq. (15), that is, the underrelaxed equations are solved by the line-by-line solver.

Let α be the underrelaxation factor. It can be readily shown that the underrelaxed form of Eq. (15) is given as

$$\frac{a_p'}{\alpha} \phi_p = \sum_n a_n \phi_n + c + (1-\alpha) \frac{a_p'}{\alpha} \phi_p^*,$$

where $a_p' = a_p - b$. This is the equation which is actually solved by the line-by-line solver.

The pressure density and viscosity (effective viscosity) are underrelaxed via

$$\phi_{\text{new}} = \alpha \phi_{\text{new}} + (1-\alpha) \phi_{\text{old}}.$$

In the present calculations, all the underrelaxation factors are set at 0.5.

2.6.2 Convergence

The convergence criterion is somewhat arbitrary and is supplied by the user. The present code uses the discretized Eq. (15) to derive the convergence criterion. From Eq. (15) a residual R is defined as

$$R = \sum_n a_n \phi_n + c - (a_p - b) \phi_p.$$

Hence, if the discretized equation is satisfied, R will be zero. Presently, the sum of all $|R|$'s over the interior grid points is normalized by appropriate reference value for each ϕ , and the resulting values are used to test convergence. All the residuals are monitored to see the convergence history. Numerical calculations reported here are based on the criterion that the maximum of the normalized residuals be less than 10^{-4} for flows involving a single species, and be less than 10^{-2} for flows involving two species.

SECTION 3

PRELIMINARY NUMERICAL COMPUTATIONS

As indicated in Paragraph 1.3, the numerical modeling of the centerbody combustor flowfields represented several phases and addressed a number of aspects. These ranged from preliminary computations directed toward the familiarization and examination of the AFWAL/PORT version of the TEACH-T program to full-fledged numerical simulation and comparison with experimental data. A summary of the preliminary calculations completed in the present modeling efforts is presented in Table 4. In this section we discuss the details of these preliminary computations. Further modeling refinements and selected results are discussed in the next section.

3.1 APL CONFIGURATION

The initial computations for the isothermal flowfield with 2 kg/s air and 8 kg/hr CO₂ flows resulted in numerical instabilities, convergence failures, and nonphysical flowfields. These computations used the two-equation turbulence model in the code. Careful examination of the code revealed that the AFWAL/PORT version of the code was written only for the reacting-flowfield computations. At the suggestion of Dr. Roquemore, we contacted Mr. Russ Claus¹⁴ of NASA/Lewis who had been operating a version of the "TEACH" Code to predict the APL combustor flowfields. It turned out that this version was specifically written for nonreacting-flowfield computations involving one-component fluid.

Accordingly, we decided to modify the AFWAL/PORT version to perform the nonreacting-flowfield computations. For this purpose, we resorted to the artifice of specifying zero heat of formation for the "fuel" (i.e., CO₂). This resulted in the desired isothermal flowfield as evidenced by the computed

TABLE 4
SUMMARY OF PRELIMINARY COMPUTATIONAL CASE STUDIES

CONFIGURATION	FLOW TYPE	VARIATIONS OF ANNULAR & CENTRAL FLOWS		PARAMETER SENSITIVITY TESTS	
		ANNULAR AIR FLOW kg/s	CENTRAL CO ₂ FLOW kg/hr	AIR FLOW 2 kg/s	CO ₂ FLOW kg/hr
APL	Isothermal Air/CO ₂	0	4, 8, 12, 16	Nonuniform Inlet Velocity Profiles	4, 8, 12
		0.05	4, 8, 12, 16	Cruder Computational Grid Spacings	4, 8, 12
		0.5	~ 0, 1, 2, 4, 8, 12, 16	TURBIN - 0.06 ALAMDA - 0.05	4, 8, 12
		1	~ 0, 2, 4, 6, 8, 12, 16		
		2	~ 0, 4, 8, 12, 16, 18, 20, 22	TURBIN - 0.06 ALAMDA - 0.01	8
		3	4, 6, 8, 12, 16, 18	TURBIN = 0.03 ALAMDA = 0.01	8
UCI	Isothermal Air/CO ₂	2	2	P&W AXIAL GRID (Uniform Velocity)	4
				P&W AXIAL GRID (Nonuniform Velocity)	4, 8, 12
		ANNULAR AIR VEL. m/s	CENTRAL CO ₂ VELOCITY, m/s	ANNULAR AIR VELOCITY, 10.77 m/s CENTRAL CO ₂ VELOCITY, 11.04 m/s	
		10.77	~ 0, 5, 10, 15, 20, 25, 30	Variation of σ_c	0.8, 0.9, 1, 1.1, 1.21, 1.3, 1.4
		4.31	~ 0, 2.5, 5, 7.5, 10, 15	Variation of σ_p	0.09, 0.12, 0.15, 0.25, 0.35, 0.5, 1.2
				Cruder Computational Grid Spacing Air Velocity 10.77 m/s	
UCI	Isothermal Air/CO ₂			ALAMDA - 0.005	CO ₂ Velocity 11.04, 20
				ALAMDA - 0.05	CO ₂ Velocity 11.04, 20

temperature field. Also, the value of the underrelaxation factors (see Paragraph 2.6.1) for all the dependent variables was changed to 0.5 to ensure better convergence. However, the computed fields of axial velocity and CO₂ mass fraction revealed nonphysical characteristics. Further examination of the code became necessary to determine the source of these uncertainties. We found that the AFWAL/PORT version requires correct specification of excess air to determine the air flow rate from the specified "fuel" flow rate. Thus, even when nonreacting calculations are performed, depending on the flow rates of air and CO₂ used in the computations, the appropriate value of the excess air must be determined and furnished as input to the program. Once this requirement was satisfied, the mass-flow calculations became consistent with the inlet velocity profiles and the numerical computations proceeded smoothly.

3.1.1 Variations of Annular and Central Jet Flow Rates

The appropriately modified version of the TEACH Code was used to compute the isothermal flowfields of the centerbody combustor for different combinations of annular and central-jet flow rates. Thus, the completed predictive modeling calculations correspond to (a) zero annular flow and 4, 8, 12, and 16 kg/hr central CO₂ flow; (b) 0.05 kg/s annular air flow and 4, 8, 12, and 16 kg/hr central CO₂ flow; (c) 0.5 kg/s annular air flow and 0 (actually 10⁻³), 1, 2, 4, 8, 12, and 16 kg/hr central CO₂ flow; (d) 1 kg/s annular air flow and 0, 2, 4, 6, 8, 12, and 16 kg/hr central CO₂ flow; (e) 2 kg/s annular air flow and 0, 4, 8, 12, 16, 18, 20, and 22 kg/hr central CO₂ flow; and (f) 3 kg/s annular air flow and 4, 6, 8, 12, 16, and 18 kg/hr central CO₂ flow. In (b) above, calculations were also made for 1 x 10⁻⁵ kg/s annular air flow and 4 kg/hr CO₂ flow. These calculations yielded results identical with those of the zero annular flow and 4 kg/hr central flow. Finally, reacting flowfield modeling was done for 2 kg/s air flow and propane flow in the central jet.

Only the case of 2 kg/hr propane resulted in converged solutions that were physically acceptable.

All these modeling calculations were conducted for the 41-x-34 computational grid with nonuniform grid spacing in both axial and radial directions. The axial extent of the computational domain was 0.3 m. In both the annular and central-jet inlets, only uniform axial velocity profiles were used. In the two-equation turbulence model, standard values for the various "constants" were used. Finally, for the specification of the values of the turbulent kinetic energy and the dissipation rate (through the specification of the inlet length scale), only the default values (TURBIN = 0.03 and ALAMDA = 0.005) in the code were used.

The computed flowfields for the two-jet flows (2 kg/s annular air flow and several CO₂ central-jet flows) exhibited trends that were in conformity with the earlier Laser Doppler Anemometer measurements. Quantitatively, however, the calculations underpredicted the centerline forward stagnation-point distances and overpredicted the rear stagnation-point distances. It appeared that better agreement between the predicted and measured results could be obtained by varying the inlet turbulence length scales.

Some of the calculated results were plotted. These included the axial profiles of the centerline mean velocities, turbulence intensities, and CO₂ mass fractions. The radial profiles of the axial velocity at an axial location of 12 cm from the centerbody face were plotted for the central flow rates of 0, 8, and 16 kg/hr. All these profiles showed the trends observed experimentally. The axial profiles were, with respect to the axial distance, normalized by the centerbody diameter. The centerline mean velocity profiles were also obtained by normalizing the axial distance with the centerline rear stagnation point distance. However, the quantitative agreement between the prediction and measurement was poor.

The single-jet calculations (with zero annular flow) showed that the results correspond to those of a free jet. The centerline axial velocity profiles (velocity normalized by the jet exit velocity and the axial distance normalized by the initial jet diameter) exhibited on a log-log plot clearly indicated the free turbulent-jet behavior. The results for the four central flow rates of 4, 8, 12, and 16 kg/hr correspond to a single curve which showed a potential core up to 5 diameters, a slope of -1 between 7 and 55 diameters, and an axial velocity decaying to 10 percent of the initial velocity in 55 diameters. The axial variation of the centerline turbulent intensity was also plotted. When the turbulence intensity was normalized with respect to the initial jet velocity, the axial profile showed an initial decay in the potential core, a rapid rise between 5 and 10 diameters, and a rapid decay beyond. However, when the normalization was with respect to the local values of the centerline mean axial velocity, there was a slow decay (from 8 to 10 percent to 2 to 4 percent) up to four diameters, a rapid rise to 30 percent (between 10 and 20 diameters), and a gradual rise to 32 percent beyond. While it is not clear if the initial decay is real, the rapid rise and the plateauing are consistent with the earlier LDA results. Because of the boundary condition representing the confined duct, in the absence of annular air flow the centerline CO₂ mass fraction did not show any significant decay downstream of the jet exit. Calculations for 4 kg/hr CO₂ flow with 1×10^{-5} kg/s annular air flow showed identical results.

To examine the concentration decay at small annular air flows, two-jet calculations were made for 0.05 kg/s annular air flow and 4, 8, 12, and 16 kg/hr CO₂ flow. The computed results for this set also showed the free-jet behavior for the centerline axial velocity (normalized with respect to the initial velocity) and the centerline CO₂ mass fraction. Indeed, both profiles appeared to be identical (with the results of the four flow rates coinciding).

The reacting flowfield calculations for 2 kg/hr propane flow showed that the centerline variation of mean axial velocity, turbulent intensity, CO₂ concentration, and temperature was consistent with the expected trends. Higher central flow rates did not yield convergent results.

Our preliminary experience with the TEACH Code indicated reasonably correct trends in predicting the centerbody combustor flowfields. Further computations of the isothermal flowfields with different grid spacings, with nonuniform inlet velocity profiles, and with appropriate inlet length scales were necessary before improvements in quantitative predictions and scaling criteria could be obtained. Accordingly, questions relating to the grid independence of the computed solutions, boundary-layer development in the inlets, and inlet turbulence intensity and length scales were addressed in several sensitivity tests.

3.1.2 Sensitivity Tests

Our calculations with 2 kg/s air flow rate and 4, 3, and 12 kg/hr CO₂ flow rates examined each of the above questions separately, as discussed in the following paragraphs.

3.1.2.1 Grid Independence of Solutions

Numerical experiments were carried out with the uniform inlet velocity profiles and default values for the inlet kinetic energy and length scale parameters; however, nonuniform grid intervals 50 percent larger than the earlier ones were employed. The results of the centerline stagnation points (distances in meters) are shown in Table 5.

The earlier results with finer grid spacings had underpredicted the locations of the forward stagnation points and overpredicted those of the rear stagnation points. The use of cruder grid intervals, however, decreases both stagnation distances, thereby making the disagreement between measurement and prediction for the forward stagnation distance worse (except the

TABLE 5
INFLUENCE OF GRID SPACINGS
ON (APL) CENTERLINE STAGNATION DISTANCES

CENTRAL JET FLOW RATE kg/hr	CENTERLINE STAGNATION DISTANCES, m			
	FORWARD STAGNATION		REAR STAGNATION	
	INITIAL GRID	50% LARGER (CRUDER)	INITIAL GRID	50% LARGER
4	0.0198	0.0185	0.184	0.176
8	0.0562	0.0548	0.189	0.180
12	0.0854	0.0871	0.191	0.183

12 kg/hr case). All the same, the changes due to the cruder grid intervals are only on the order of five percent. Thus, it would seem that the computations do exhibit adequate grid independence in the range of grid intervals investigated in the computations.

3.1.2.2 Influence of Inlet Velocity Profile

The effect of the boundary-layer development in the inlets is shown in Table 6. For this purpose, the inlet velocity profiles employed were uniform everywhere except at the grid nodes adjacent to the inlet walls where the velocities were 95 percent of the uniform values. The older grid intervals and default values of TURBIN and ALAMDA were used.

The boundary-layer growth in the inlets tends to increase both stagnation distances. While this is in the desired direction for the forward stagnation distance, it makes the departure from the measurement for rear stagnation distance worse. However, the change in the latter case is only on the order of three percent, thus showing that the effect on the rear stagnation point is very small. In the case of the forward stagnation point, the change is about seven percent for 4 kg/hr, four percent for 8 kg/hr, and five percent for 12 kg/hr. It may be recalled that the departure of the prediction from the measurement is also higher at lower central flow rates. Thus, it appears that the use of the nonuniform inlet velocity profiles would result in better agreement between measured and predicted forward stagnation distances, without causing significantly greater disagreement for the rear stagnation distances.

3.1.2.3 Influence of Inlet Turbulence Parameters

Computations that examined the influence of inlet turbulent kinetic energies and length scales employed the values of 0.06 for TURBIN and 0.05 for ALAMDA (λ). These are respectively twice and ten times the default values for these parameters. Flat inlet velocity profiles and finer grid intervals were used. Table 7 presents the results.

TABLE 6
INFLUENCE OF INLET VELOCITY PROFILES
ON (APL) CENTERLINE STAGNATION DISTANCES

CENTRAL JET FLOW RATE kg/hr	CENTERLINE STAGNATION DISTANCES, m			
	FORWARD STAGNATION		REAR STAGNATION	
	FLAT PROFILE	95% PROFILE	FLAT PROFILE	95% PROFILE
4	0.0198	0.0212	0.184	0.189
8	0.0562	0.0582	0.189	0.193
12	0.0854	0.0898	0.191	0.196

TABLE 7
INFLUENCE OF INLET TURBULENT ENERGIES AND LENGTH SCALES
ON (APL) CENTERLINE STAGNATION DISTANCES

CENTRAL JET FLOW RATE kg/hr	CENTERLINE STAGNATION DISTANCES, m			
	FORWARD STAGNATION		REAR STAGNATION	
	0.03/0.005	0.06/0.05	0.03/0.005	0.06/0.05
4	0.0198	0.0205	0.184	0.185
8	0.0562	0.0574	0.189	0.191
12	0.0854	0.0861	0.191	0.193

It is clear that the effect on the rear stagnation distance is on the order of only one percent. For the forward stagnation distance, the change decreases from about 3.5 percent at the lowest central flow rate to about 0.8 percent at the highest. Again, the perceived changes favor the forward stagnation distances. To isolate the influence of the length scales from that of the turbulent energies, calculations were made for different values of TURBIN and ALAMDA for the central flow rate of 8 kg/hr. These results are shown in Table 8.

It is seen that doubling the length scale increases the forward stagnation distance by 0.9 percent and the rear stagnation distance by 0.5 percent. However, doubling the turbulent kinetic energy (although at the larger length scales) increases the forward stagnation distance by 1.4 percent and the rear stagnation distance by 1.6 percent. Doubling the kinetic energy and increasing the length scales by ten times appear to be better than doubling both the kinetic energy and the length scales in the sense that, in the former case, the increase in forward stagnation distance is accompanied by a lesser increase in rear stagnation distance. However, it must be reiterated that the perceived changes are too small to be significant, especially at higher central flow rates.

3.1.2.4 Influence of the Exit Boundary Location

A single computation for the central flow rate of 4 kg/hr was made with flat inlet velocity profiles and default values of ALAMDA and TURBIN but with an axial computational extent of 1.2 m. This corresponded to the 39-x-39 computational grid of Sturgess and Syed.⁶ Since the radial extent is fixed by the duct radius (of 12.7 cm), the radial grid intervals were kept the same as our earlier (finer) grid but the axial grid points were those of the 39-x-39 grid. This resulted in a forward stagnation distance of 0.0209 m and a rear stagnation distance of 0.18 m (as compared to our benchmark values of 0.0198 m and 0.184 m). To

TABLE 8
INFLUENCE OF ALAMDA AND TURBIN FOR 3 kg/hr CO₂ FLOW

TURBIN	ALAMDA	LENGTH SCALES, mm		CENTERLINE STAGNATION DISTANCES, m	
		CENTRAL	ANNULAR	FORWARD	REAR
0.03	0.005	0.012	0.285	0.0562	0.189
0.03	0.01	0.024	0.57	0.0567	0.190
0.06	0.01	0.024	0.57	0.0575	0.193
0.06	0.05	0.12	2.85	0.0574	0.191

investigate this computational grid further, flowfield computations were completed for the three central jet CO₂ flow rates of 4, 8, and 12 kg/hr. Nonuniform inlet velocity profiles of the type used earlier and the values of 0.05 and 0.06 respectively for ALAMDA and TURBIN were employed in these calculations. The centerline distances of the forward and rear stagnation points are as follows: 4 kg/hr : 0.0216 m and 0.188 m; 8 kg/hr : 0.0634 m and 0.195 m; 12 kg/hr : 0.0964 m and 0.196 m. Thus, it became clear that all these computations predicted centerline rear stagnation distances typically 50 percent larger than the measured distances.¹⁰ Perceived influences of changes in grid intervals, inlet velocity profiles, inlet turbulent energies and inlet length scales did not result in better agreement between the predicted and measured values.

3.2 UCI CONFIGURATION

A centerbody combustor of roughly 1/5 scale model of the APL configuration is being operated at the University of California, Irvine. Since some experimental data were available for this combustor,²¹ it was of interest to obtain the predictions with our TEACH code. For this purpose, the computations have employed values of 50.8 mm, 28 mm, and 1.27 mm respectively for the diameters of the duct, the centerbody, and the fuel tube. Subsequently, we were told that the actual UCI dimensions were slightly different, viz., 51 mm, 30.5 mm, and 1.3 mm. It is noted that neither set exactly corresponds to a 1/5 scale model of the APL combustor. Our computations were carried out with respect to the former set of dimensions.

3.2.1 Variations of Annular and Central Jet Flow Rates

The slight difference in the dimensions of the configuration indicated earlier meant that a reference duct velocity of 7.5 m/s corresponds to an annulus velocity of 11.7 m/s in the UCI experiments and an annulus velocity of 10.77 m/s in our calculations.

All the calculations for sensitivity tests were done for the annulus air velocity of 10.77 m/s. The UCI experimental results were reported in terms of the overall equivalence ratios. Thus, for an equivalence ratio of 0.02 and annular air velocity of 10.77 m/s, the central CO₂ inlet velocity was 11.04 m/s. For this value of CO₂ velocity and an equivalence ratio of 0.05, the annular air velocity was 4.31 m/s. Accordingly, the predictive calculations corresponded to (a) annular air velocity of 10.77 m/s and central CO₂ velocities of 0, 5, 10, 15, 20, 25 and 30 m/s; (b) annular air velocity of 4.31 m/s and central CO₂ velocities of 0, 2.5, 5, 7.5, 10 and 15 m/s. In both of the above cases, the highest CO₂ velocity cases resulted in the complete penetration of the recirculation region by the central jet.

3.2.2 Sensitivity Tests

The numerical calculations that examined the sensitivity of model parameters were based upon the annular air velocity of 10.77 m/s and central CO₂ velocity of 11.04 m/s. The two major tests related to the turbulence Schmidt number σ_ϵ for the dissipation equation (see Table 1) and the constant c_μ in the k- ϵ model [see Eq. (4)].

3.2.2.1 Influence of σ_ϵ

In the TEACH code, the eddy viscosity (the momentum exchange coefficient) is computed from Eq. (4). The exchange coefficients for other variables are obtained by prescribing the values of the appropriate Schmidt numbers, σ . Thus, as shown in Table 1, constant values of 1 and 1.3 are used for σ_k and σ_ϵ , corresponding to the variables k and ϵ . The default value used for σ_ϵ in the AFWAL/PORT TEACH version, however, was 1.21 and all the earlier computations had been performed for this value. We wanted to find out if the prediction of the rear stagnation point is influenced by σ_ϵ . For $\sigma_\epsilon = 1.21$, the normalized forward and

rear stagnation distances (normalized with respect to the centerbody diameter) were found to be 0.4565 and 1.2569. Variation of σ_ε from 0.80 to 1.40 in steps of 0.10 showed that, except for $\sigma_\varepsilon = 0.80$ (when both fore and aft stagnation points moved farther downstream), the value of σ_ε did not have much effect on the predictions. In particular, for $\sigma_\varepsilon = 1.3$, the fore and aft stagnation points were at the normalized distances of 0.4508 and 1.2575. In terms of the ratio of the stagnation distances and the ratio of inlet velocities, this result corresponded to $z_F/z_A = 0.3585$ and $W_F/W_A = 1.025$. While the results for $\sigma_\varepsilon = 1.21$ and $\sigma_\varepsilon = 1.3$ did not differ significantly, from the viewpoint of comparisons with other TEACH predictions all the subsequent predictive results were obtained for $\sigma_\varepsilon = 1.3$.

3.2.2.2 Influence of c_μ

To examine the influence of c_μ a set of computations was carried out for the same air and CO_2 velocities as selected earlier. The value of σ_ε was kept at 1.21. The values of c_μ tested were 0.12, 0.15, 0.25, 0.35, 0.90, and 1.20. As seen in Figure 3, c_μ has a very strong influence on the results. Increasing the value of c_μ resulted in decreasing both the fore and aft stagnation distances. Thus, we get for $c_\mu = 0.12$, the values of 0.3745, 1.1308, and 0.3312, and for $c_\mu = 0.15$, the values of 0.3308, 1.0509, and 0.3148 as the normalized forward stagnation distance, the normalized rear stagnation distance, and their ratios. It is interesting to note that an air stagnation distance of roughly one centerbody diameter can result from a c_μ value less than twice the accepted value of 0.09. Since an increase in c_μ leads to an increase in the turbulent eddy viscosity, it would seem that this can result in an enhanced turbulent mixing rate in the recirculation region, which tends to mitigate the overprediction of the rear stagnation point. No doubt this is a rather crude explanation, in view of the fact that the influence of c_μ is pervasive in the differential equations for

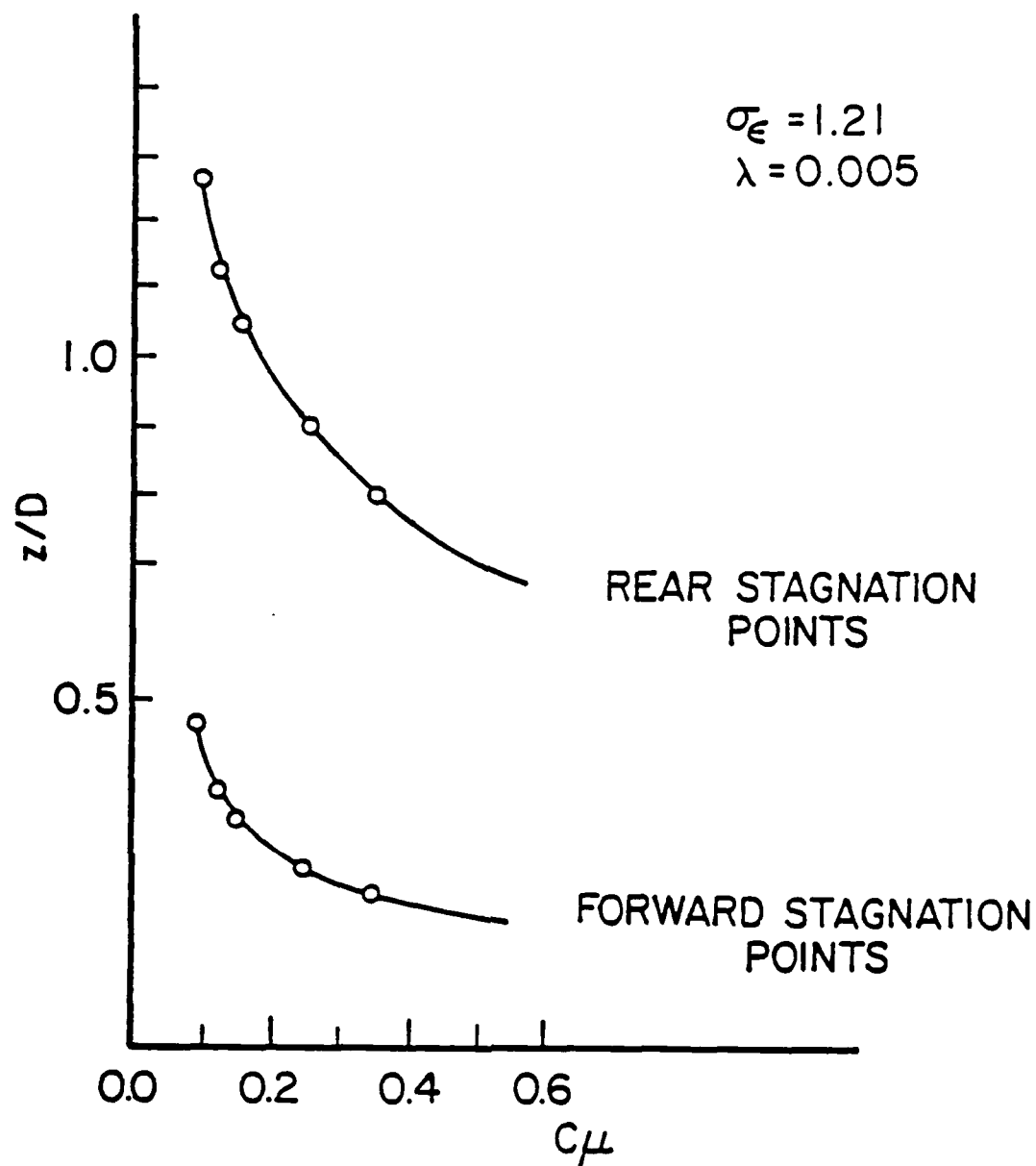


Figure 3. Influence of c_μ on the Centerline Stagnation Points (UCI Combustor).

axial and radial momentum, turbulent kinetic energy, and turbulent dissipation.

3.2.2.3 Other Effects

All the above computations were performed with the 41-x-34 grid and with the exit-plane boundary of the computational domain being located a distance of 6.2 cm from the face of the centerbody. The parameter TURBIN for the inlet turbulent kinetic energy was specified as 0.03 and the parameter ALAMDA for the inlet turbulent length scale was specified as 0.005. A limited number of sensitivity tests were conducted to ascertain the influence of grid size and of the length-scale parameter ALAMDA. The value of ALAMDA employed for this purpose was 0.05 and the coarse axial grid intervals corresponded to roughly 1.6 times the previous grid intervals. This yielded an exit-plane boundary location of 10 cm. These tests used $\sigma_\epsilon = 1.3$ and $c_\mu = 0.09$. The general effect of the ten-fold increase in the inlet turbulence length scale, or of the cruder grid size, or of the farther exit boundary was to move both the forward and rear stagnation points slightly upstream. The changes were relatively insignificant, and this conclusion conformed to the results of the sensitivity testing reported in Paragraph 3.1.2 for the APL configuration.

3.3 SIMILARITY CONSIDERATIONS

The preliminary studies of the centerbody configuration indicated that the numerical predictions resulted in qualitatively correct flowfield characteristics. This observation was essentially based upon the axial variation of the centerline mean axial velocity and turbulence kinetic energy. For the entire range of central jet flow rates from the annular jet dominant regime (where the central jet is completely turned back toward the centerbody) to the central jet dominant regime (where the central jet completely penetrates the near-wake recirculation

region), the numerical results were consistent with the experimental trends. However, as emphasized earlier, the quantitative results of the centerline stagnation points were not satisfactory. In particular, the numerical calculations underpredicted the forward stagnation points and overpredicted the rear stagnation points. Since the parameter sensitivity tests failed to explain this discrepancy between the predictions and measurements, it was of interest to ascertain whether the numerical calculations demonstrate internal consistency with respect to certain well-known characteristics of free turbulent shear flows.

Of special interest was the radial variation of the mean axial velocity field. Sufficient experimental evidence exists for the similarity of mean velocity profiles in free turbulent shear flows as occurring in jets and wakes. In successive axial stations in the downstream direction, the mean axial velocity profile in the radial direction exhibits the more or less bell-shaped curves under suitable normalizations of the velocity field and lateral distance. Since the similarity of mean axial velocity field is the necessary condition for correctly predicting the flowfield behavior, our preliminary numerical results of the centerbody flowfields remained to be checked for this aspect.

3.3.1 Centerbody Combustor Configurations

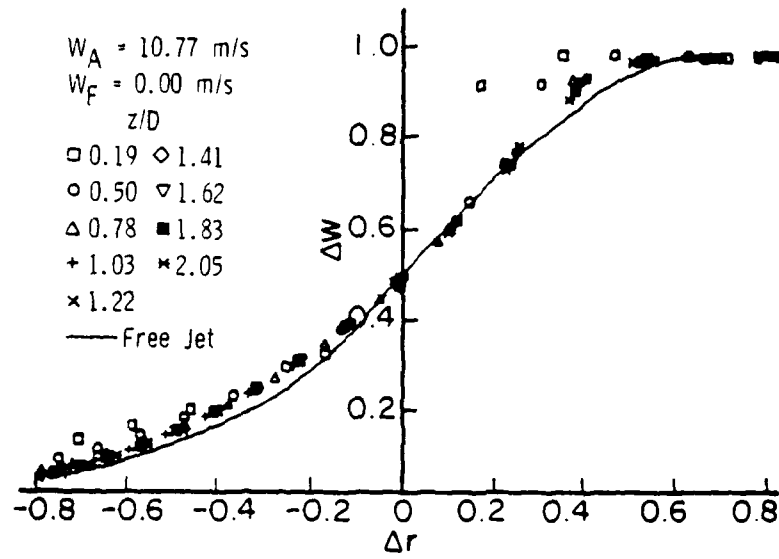
The TEACH code predictions of the radial variation of the mean axial velocity in both the APL and UCI configurations were examined from the viewpoint of obtaining universal profiles. For this purpose, the data of radial coordinates, r , and axial velocities, $W(r)$, were normalized following the suggestion of Abramovich.⁴² The normalized radial coordinate is defined as $\Delta r \equiv (r - r_{0.5}) / (r_{0.9} - r_{0.1})$ and the normalized axial velocity is defined as $\Delta W \equiv [W(r) - W_{\min}] / (W_{\max} - W_{\min})$. Here, W_{\max} and W_{\min} are

the maximum and minimum axial velocities at any given axial station. The values of $r_{0.9}$, $r_{0.5}$, and $r_{0.1}$ correspond to the radial locations (at any given axial station) where $(W-W_{min})$ is respectively equal to 90, 50, and 10 percent of $(W_{max}-W_{min})$ (at the same axial station).

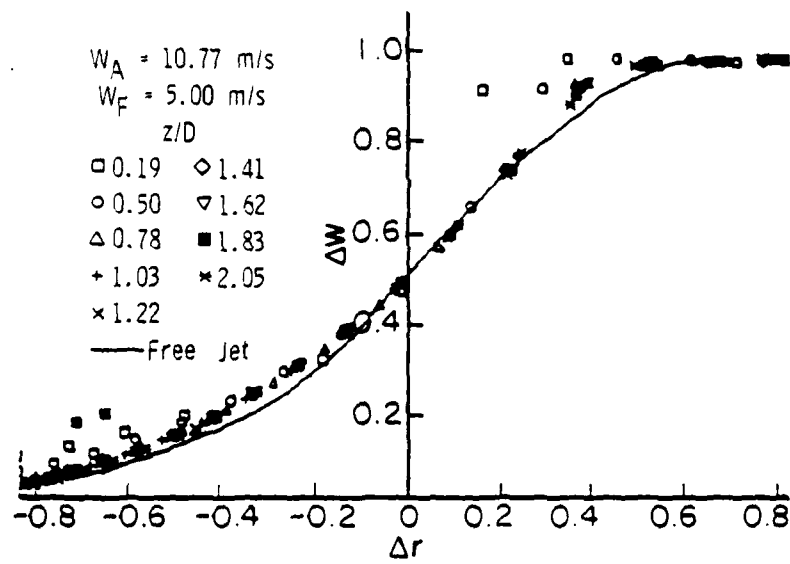
3.3.1.1 UCI Configuration

For the UCI configuration, experimental conditions in Reference 21 corresponded to a reference velocity in the duct of 7.5 m/s and overall equivalence ratios of 0.02 and 0.05. For numerical modeling, two different annular air flow rates were considered, corresponding to the values of 10.77 m/s and 4.31 m/s for the annular air velocities. Figures 4(a) through (g) present the results for the air velocity of 10.77 m/s. The central-jet exit velocity for CO_2 ranged from nearly zero to 30 m/s, in steps of 5 m/s. For all cases except the highest CO_2 flow, reverse air flow occurred, giving rise to two stagnation points on the centerline. As anticipated from the extrapolated results for the centerline peak negative axial velocity as a function of CO_2 exit velocity which gave a value of 28 m/s for the "breakthrough" velocity, the centerline reverse flow was completely eliminated for the 30 m/s case.

We note that the above results cover the entire range of conditions from the annular jet dominant case to the central jet dominant case. With the centerline rear stagnation point (when it exists) being located at normalized axial distances (z/D) of 1.22 through 1.31, the radial profiles presented correspond to both inside and outside the recirculation region. Finally, in Figure 4(c) through (f) (for CO_2 exit velocities 10 through 25 m/s), the axial stations considered are upstream and downstream of the centerline forward stagnation point. An inspection of the normalized radial profiles of the mean axial velocity reveals the tendency toward a universal similarity

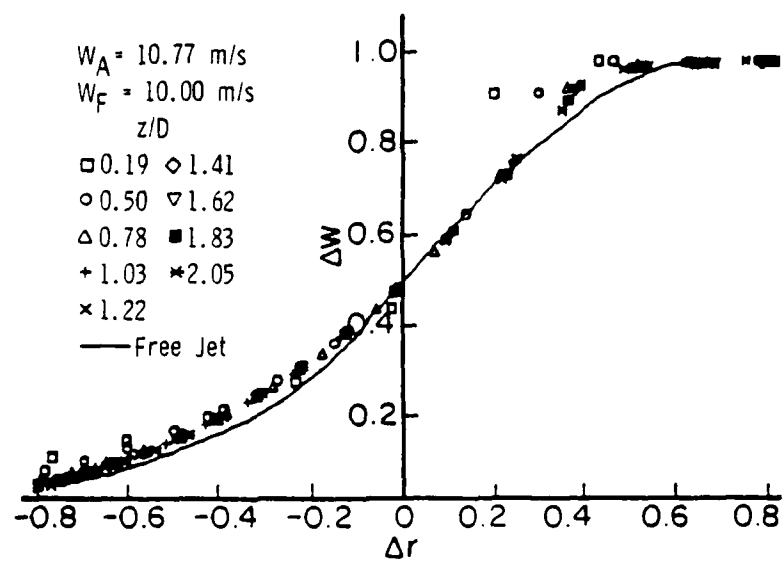


(a)

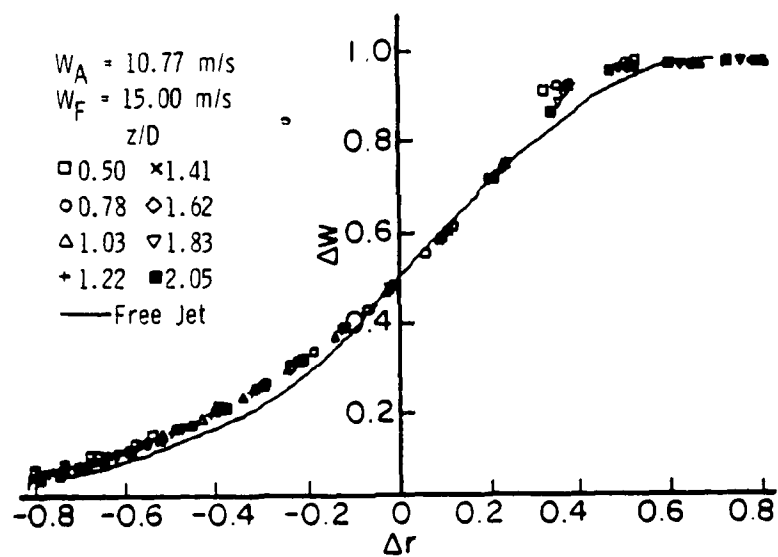


(b)

Figure 4. Mean Axial Velocity Predictions for the (UCI) Centerbody Configuration.

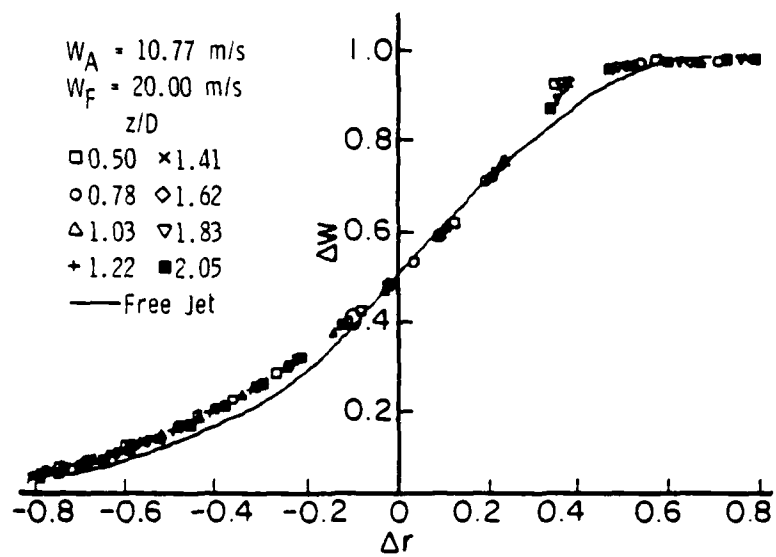


(c)

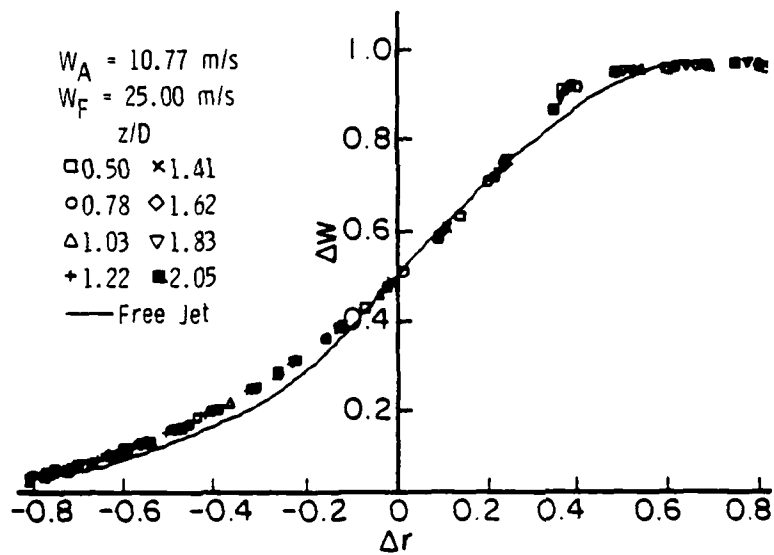


(d)

Figure 4. Mean Axial Velocity Predictions for the (UCI) Centerbody Configuration.



(e)



(f)

Figure 4. Mean Axial Velocity Predictions for the (UCI) Centerbody Configuration.

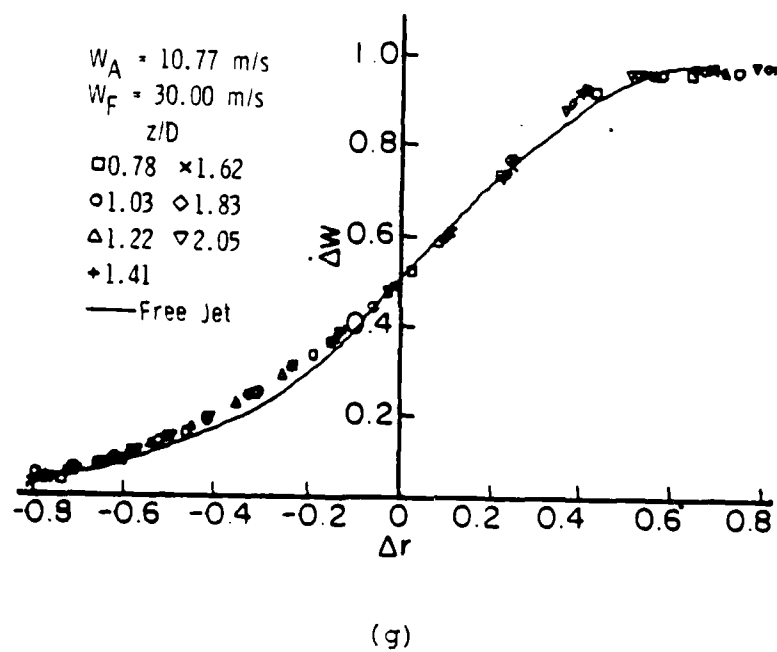


Figure 4. Mean Axial Velocity Predictions for the (UCI) Centerbody Configuration.

profile. The solid line in all these figures is the result for a free jet (reproduced from Abramovich).⁴²

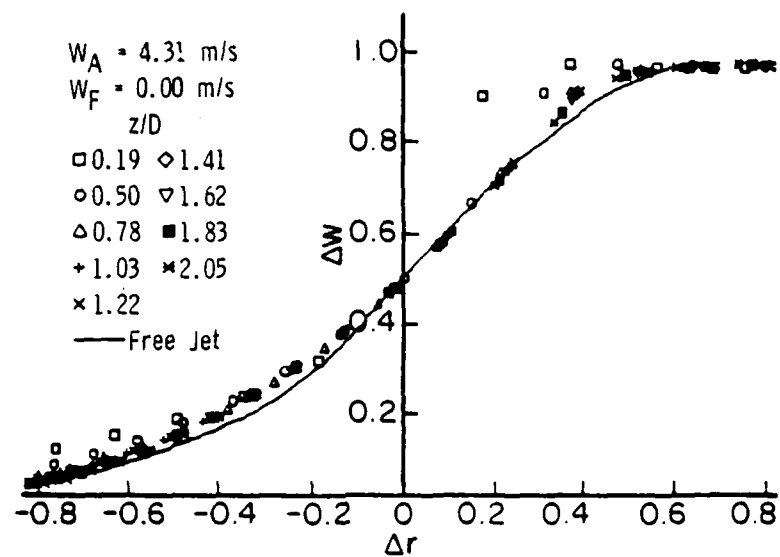
It must be noted here that although it is not explicitly pointed out in Abramovich,⁴² some care is required in obtaining the set of radii $r_{0.1}$, $r_{0.5}$, and $r_{0.9}$. It appears that monotonicity is a necessary condition in that either of the inequalities $r_{0.1} > r_{0.5} > r_{0.9}$ or $r_{0.1} < r_{0.5} < r_{0.9}$ must be strictly valid for the normalization $(r-r_{0.5})/(r_{0.9}-r_{0.1})$ to be unambiguous. It is easy to see that the former inequality applies for the annular jet near the confining duct and the latter inequality applies for the central jet near the centerline. While at some axial stations and under certain flow conditions a single set of radii may suffice all the way from the centerline to the duct wall, in general it has been found that upstream of the rear stagnation point both inequalities occur. When two such sets of radii exist, the resulting normalizations conform properly to the universal profile in their respective regions and deviate from it in the other. For example, one set of radii is appropriate for $-1.25 < \Delta r < 0$ and the other for $0 < \Delta r < 1.25$. The results presented here are the composites of two such normalizations with the deviant portions of the curve being deleted in the figures. Although the implications of these observations are not clear, it seems that jet-like and wake-like behaviors occur in the appropriate regions.

Furthermore, for the free jet issuing into a quiescent region, W_{\max} occurs at the centerline and W_{\min} ($= 0$) occurs asymptotically at the "edge" of the jet. Thus, both ΔW and Δr are unambiguous. The juxtaposition, however, of the confining duct, annular jet, centerbody-wake region, and central jet does introduce an essential element of nonuniqueness. For example, when the central jet still retains its forward momentum, the centerline axial velocity is positive and is also greater than

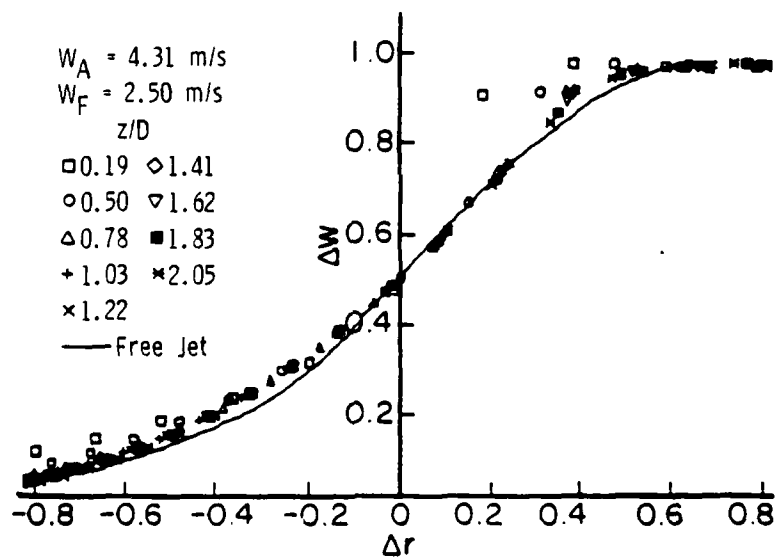
the axial velocities at neighboring off-centerline radial locations. Thus, the centerline velocities represent W_{\max} at those axial stations. Downstream of the forward stagnation point, the centerline axial velocities are negative and correspond to W_{\min} for the axial locations between the forward and rear stagnation points. It is also easy to see that upstream of the forward stagnation point there are off-centerline radial locations where the axial velocities are negative and represent W_{\min} at those axial locations. Similar off-centerline observations can be made when the central jet has eliminated the reverse flow on the centerline. These differences account for the discrepancies between the normalized curves for the free jet and the centerbody flowfield.

The above comments are further confirmed when we examine the behavior of the universal curve as a function of the exit velocity of the CO_2 jet. With increasing central jet velocity, the tendency of the predicted data to show greater conformity with the free jet curve is unmistakable. Also, we notice the velocity "overshoot" for $0.25 < \Delta r < 0.50$ for the different axial locations (the closer the axial location to the centerbody, the larger the discrepancy). An examination of the raw data shows that this region denotes the entrainment of the CO_2 jet by the shear layer of the annular jet. Clearly this effect should diminish as the strength of the central jet increases. This is evident from Figure 4(f) and (g).

In Figures 5(a) through (f), the predicted results for the air velocity of 4.31 m/s are shown for the central-jet exit velocity for CO_2 ranging from nearly zero to 15 m/s. Since the critical exit velocity for "breaking through" the recirculation region is found to be 12 m/s by extrapolation, the flowfield for 15 m/s CO_2 exit velocity represents the central jet dominant

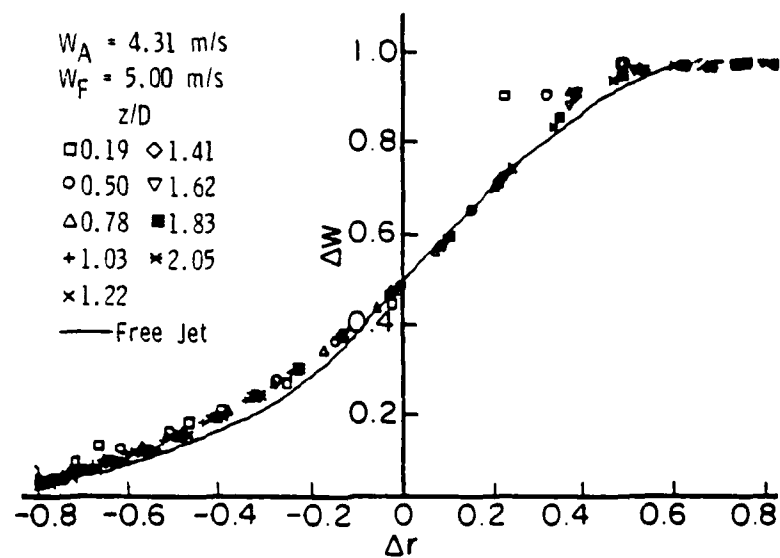


(a)

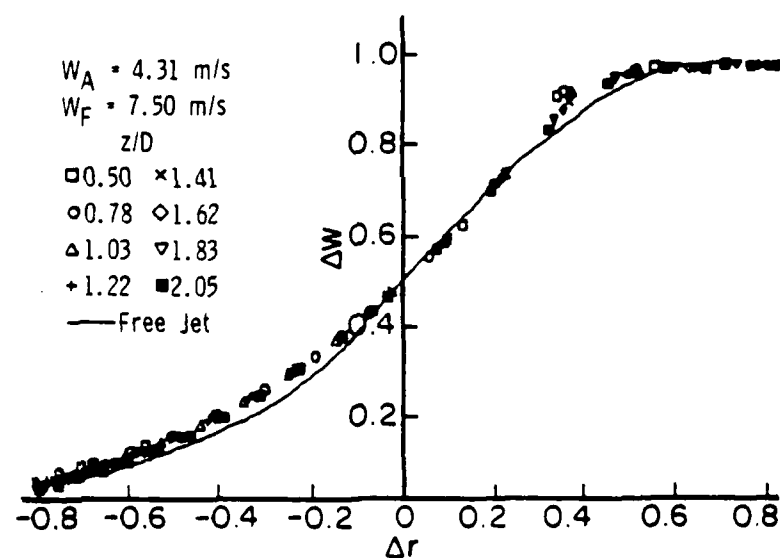


(b)

Figure 5. Mean Axial Velocity Predictions for the (UCI) Centerbody Configuration.

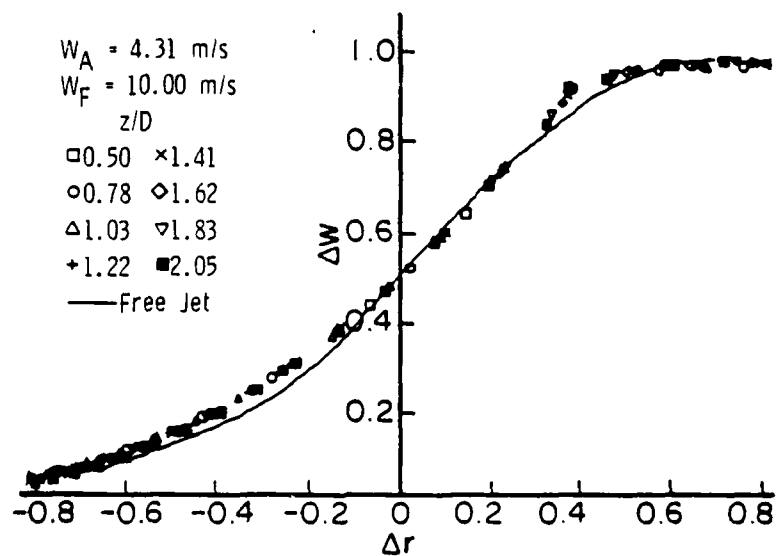


(c)

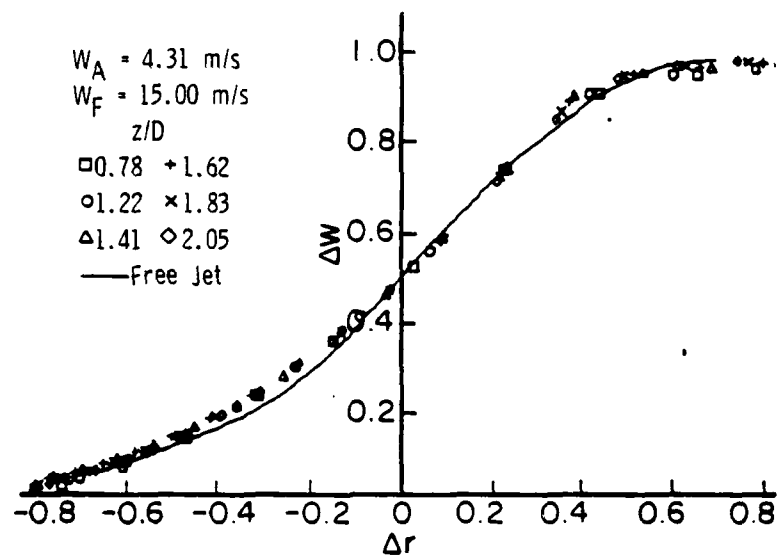


(d)

Figure 5. Mean Axial Velocity Predictions for the (UCI) Centerbody Configuration.



(e)



(f)

Figure 5. Mean Axial Velocity Predictions for the (UCI) Centerbody Configuration.

regime wherein the reverse flow along the centerline is eliminated. The normalized profiles exhibit similarity as before and these data also confirm that the universality of the velocity profile holds at different annular air velocities as well.

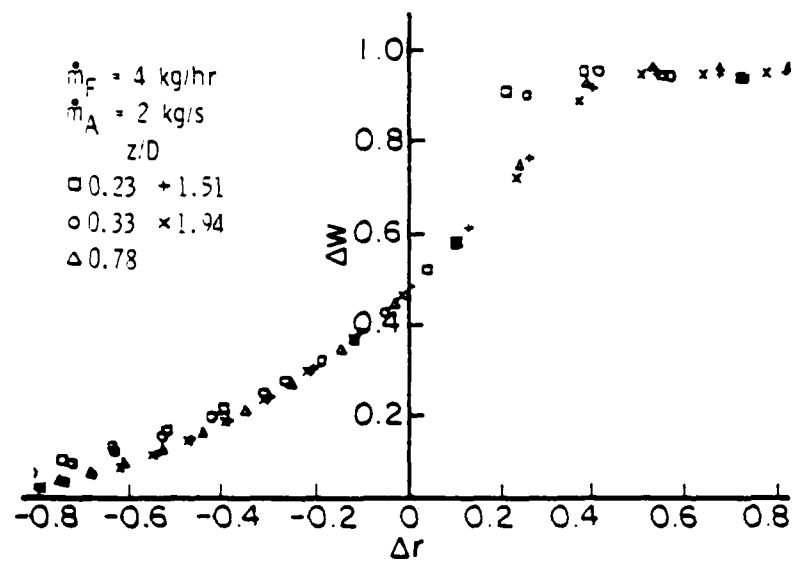
3.3.1.2 APL Configuration

The predicted results for the APL configuration are shown in Figures 6(a) through (c). Here, the flowfields considered are those for the annular air mass flow of 2 kg/s and central CO₂ mass flows of 4, 8, and 16 kg/hr. Although TEACH computations were completed for other annular air mass flows of 0.07, 0.5, 1, and 3 kg/s and for a large range of CO₂ mass flows in each case, Abramovich-type normalizations were not done for all these cases. However, from the smaller subset seen in Figure 6, it is clear that combustor scaling preserves the similarity of the radial profile of the mean axial velocities.

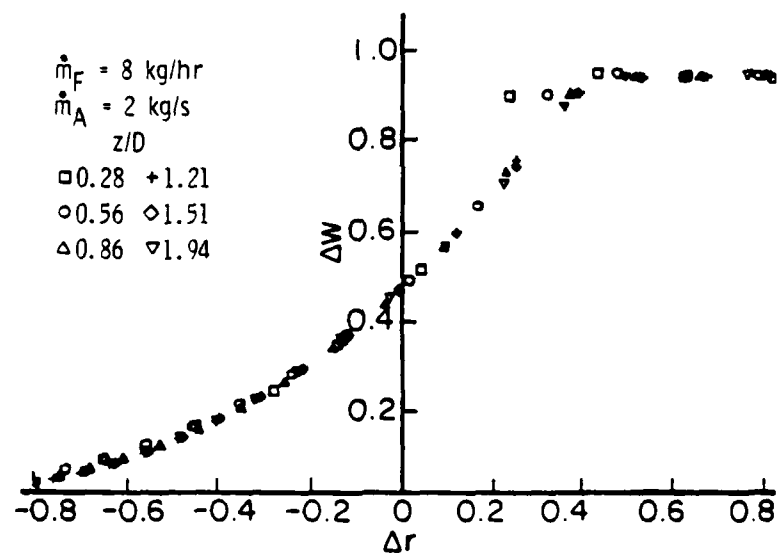
The foregoing observations based upon TEACH code predictions are strengthened by an examination of experimental data of the profile measurements in the APL configuration. The normalization of all the available data^{12,43} for annular air mass flow of 2 kg/s is seen in Figure 7. It is clear from these data that the predicted behavior is real in the centerbody configuration.

3.3.2 Other Flowfield Configurations

In view of the observed universal nature of the radial variation of the axial velocity in the centerbody configuration, it is of interest to examine other flowfields investigated in the literature. Figure 8, which shows the configuration and the normalized results of Abramovich and Vafin,⁴² forms the basis of our line of inquiry. This configuration is quite similar to that of the centerbody combustor. It differs only in the absence of the central jet and in the much shorter length-to-diameter ratio of the centerbody. The previously noted departure of



(a)



(b)

Figure 6. Mean Axial Velocity Predictions for the (APL) Centerbody Configuration.

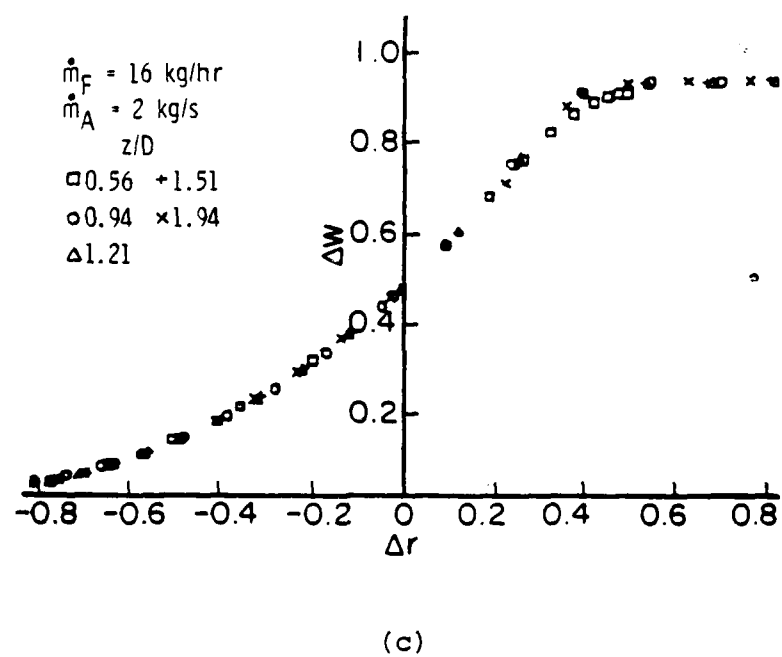


Figure 6. Mean Axial Velocity Predictions for the (APL) Centerbody Configuration.

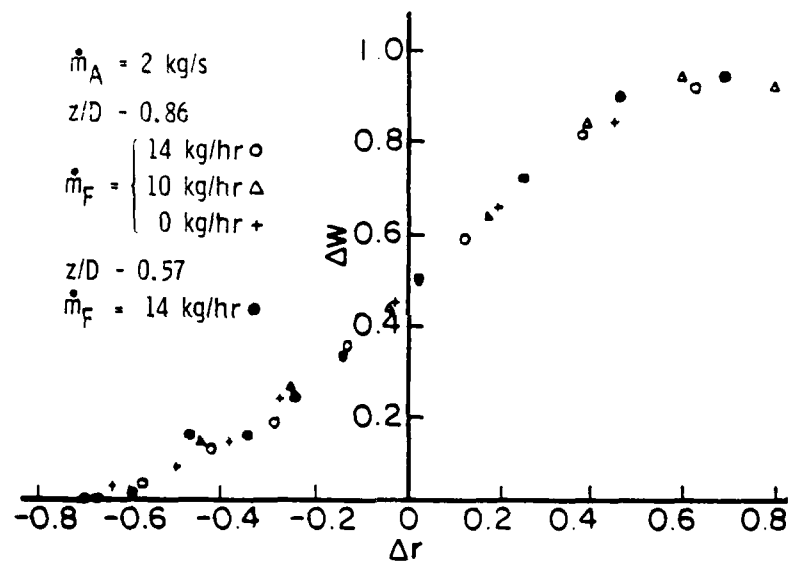


Figure 7. Mean Axial Velocity Measurements⁴³ for the (APL) Centerbody Configuration.

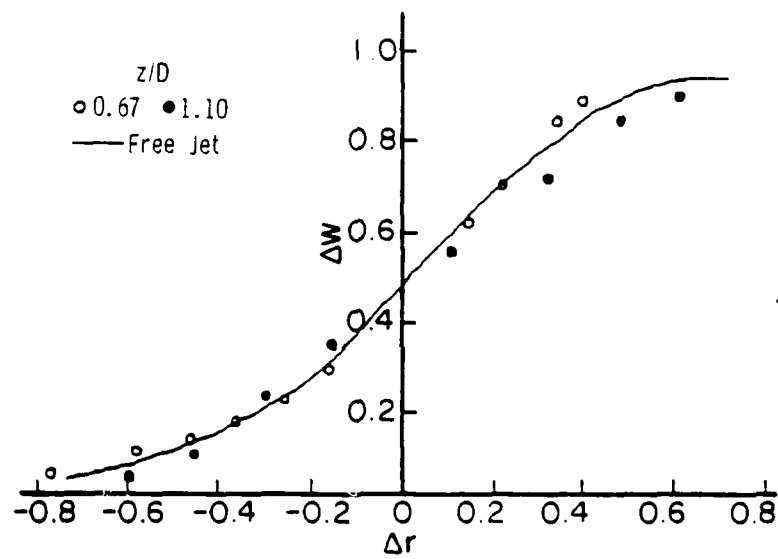
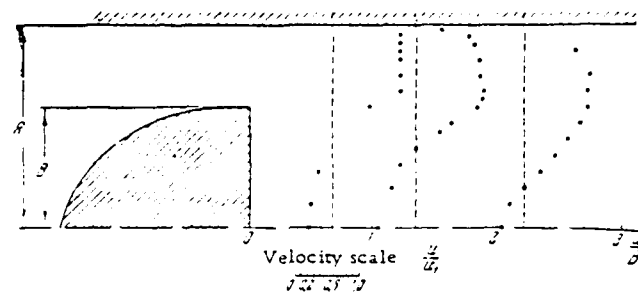


Figure 8. Mean Axial Velocity Measurements⁴² for the (Abramovich) Centerbody Configuration.

experimental data from the free jet behavior is clearly observed here. Furthermore, one notices the large acceleration of the annular flow and the consequent reduction of the boundary-layer growth in this configuration. It appears that from the results of our centerbody configuration, which has a greater propensity for boundary-layer growth, the similarity of the mean velocity profiles does not depend strongly on the presence of the centerbody boundary layer.

The flowfields discussed thus far represent confined flows because of the presence of the outer duct wall. An example of an unconfined flowfield is that downstream of an annular nozzle, investigated by Ko and Chan.⁴⁴ While the complete details of their configuration are not available, the annular jet is formed by the flow of a uniform stream over one end of a long cylinder, with its axis aligned parallel to the direction of the stream and located concentrically inside a converging duct. The trailing end of the cylinder is made flush with the exit plane of the duct (see the upper part of Figure 9). The outer diameter, D_o , of the annular jet is 6.2 cm and the inner diameter, D_i , (which is the diameter of the cylinder) is 2.8 cm, giving a blockage ratio ($= 1 - D_i^2/D_o^2$) of 0.80 (the value quoted in the paper is 0.78). For the APL configuration, the blockage ratio is 0.70.

The hot-wire measurements of the axial velocity as a function of the radial position at different axial locations are shown in the normalized coordinates in the lower part of Figure 9. Ko and Chan superimposed the confined annular jet results of Abramovich and Vafin⁴² as well as the results of the single jet and demonstrated the existence of similarity of the mean velocity profiles for their unconfined configuration. We note that the farthest axial station of their measurements is at 1.1 cylinder diameter, just short of the centerline reattachment point (located at 1.11 cylinder diameter). Our predictions for the

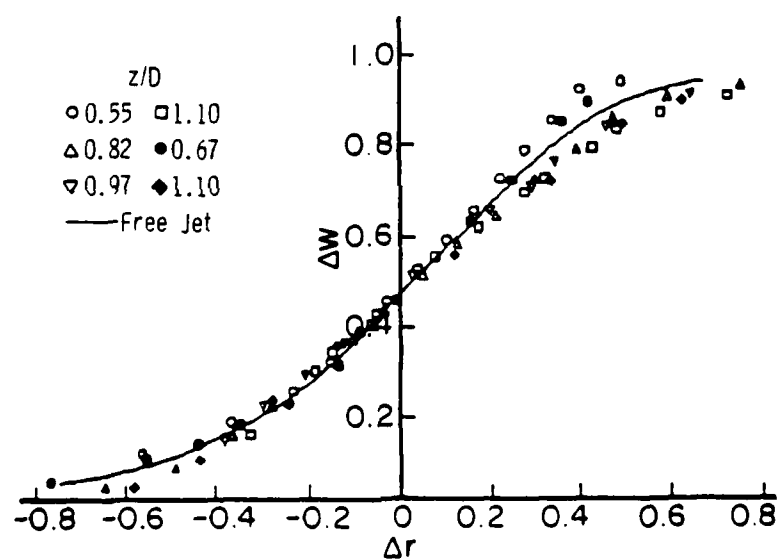
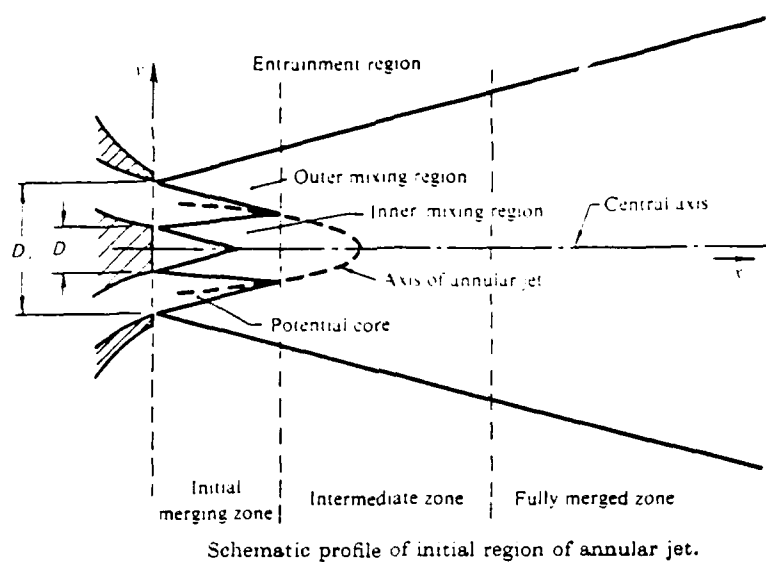
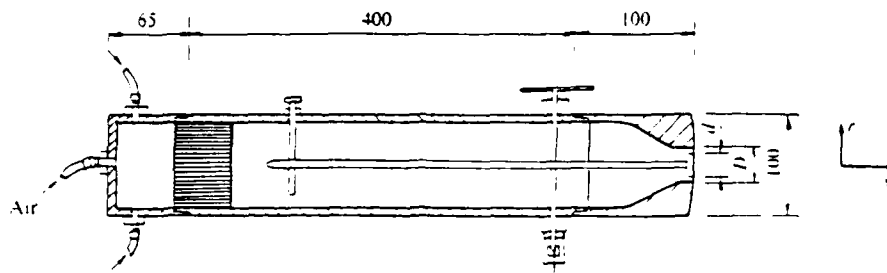


Figure 9. Mean Axial Velocity Measurements⁴⁴ for the Unconfined Annular Jet Around a Centerbody.

centerbody configurations, however, extend to more than two diameters of the centerbody (thus, farther downstream of the reattachment point) and still retain the similarity of the axial velocity field.

Although the upstream details of the forebody and the outer converging nozzle are not provided by Ko and Chan, we may conclude that their annular jet stream is nearly axial at the exit plane. While the boundary-layer growth on the inner wall of the nozzle is expected to be minimal, there can be appreciable boundary-layer development on the cylinder, depending on how long it is. An exit configuration exhibiting little boundary-layer effects but which introduces a radial velocity component at the exit plane is the annular jet of Durão and Whitelaw,⁴⁵ illustrated in the upper part of Figure 10(a). This is again an unconfined flowfield, downstream of a disk concentrically located inside a converging nozzle. Laser Doppler velocimetry was employed to furnish the axial and radial velocity components downstream of the disk. The exit-plane measurements revealed a significant radial velocity component. We have presented their raw data of the radial variation of the mean axial velocity in the normalized form, as seen in the lower part of Figure 10(a). The results shown here pertain to the disk of 14.2 mm diameter (giving a blockage ratio of 0.50) and an exit axial velocity of 26.8 m/s. For these conditions, the centerline reattachment point is located at one disk diameter downstream. The normalized results show that the velocity profiles in the near field (upstream of the stagnation point) do not exhibit similarity. The deletion of the data corresponding to the first two axial stations (i.e., at 0.14 and 0.42 disk diameters) as illustrated in Figure 10(b) clarifies this point. We believe that the presence of significant outward radial velocity component in the annular stream very close to the exit plane distinguishes this configuration from all the other configurations discussed earlier



Annular-jet configuration. Dimensions in mm. $U_0 = 39.5, 26.3, 16.9$ or 9.4 m/s;
 $D = 20.0$ mm; $d = 14.2, 12.5$ or 8.9 mm; disks manufactured with sharp edges.

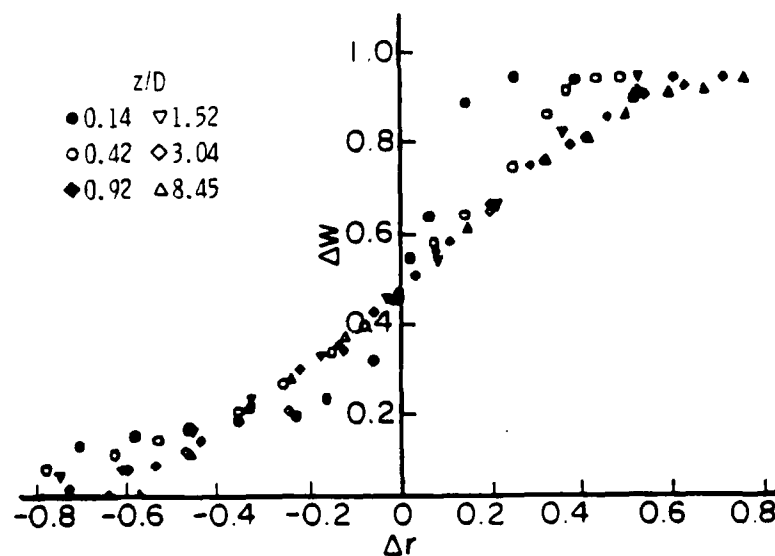
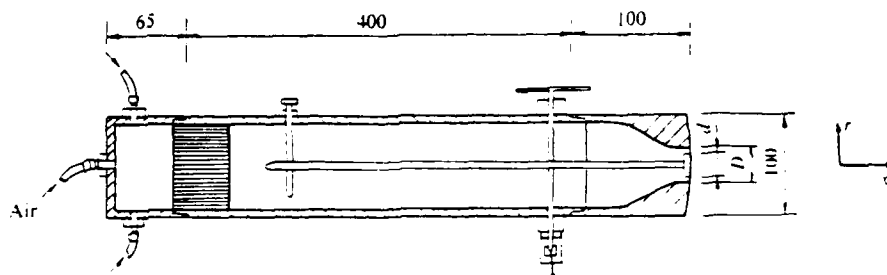


Figure 10 (a). Mean Axial Velocity Measurements⁴⁵ for the
 Unconfined Annular Jet Around a Disk.



Annular-jet configuration. Dimensions in mm. $U_0 = 39.5, 26.8, 16.9$ or 9.4 m/s;
 $D = 20.0$ mm; $d = 14.2, 12.5$ or 8.9 mm; disks manufactured with sharp edges.

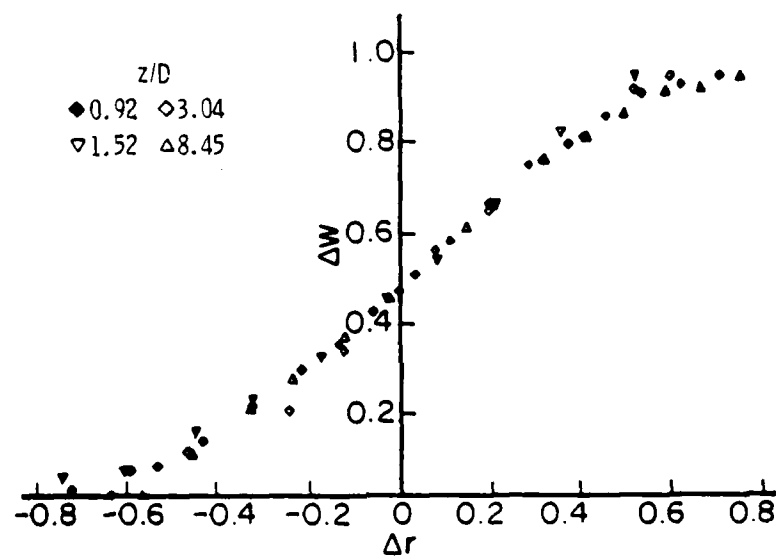


Figure 10 (b). Mean Axial Velocity Measurements⁴⁵ for the
 Unconfined Annular Jet Around a Disk.

and thereby contributes to the marked departure from similarity. Farther downstream, where the radial velocity components are directed inward (toward the centerline), the flowfield begins to resemble all the near-wake flows considered earlier (presumably, the downstream flow development no longer retains the memory of the initial profile at the exit plane).

The foregoing lends support to our viewpoint that all the flowfields investigated so far belong to one class of turbulent flows which obeys certain similarity considerations for the mean axial velocity. The composite of all the data (predictions and measurements) for all the configurations displayed in Figure 11 vividly demonstrates this point.

3.3.3 Species Concentration Fields

Previous fluid dynamic studies have shown that when temperature and species concentration effects are present, suitably normalized temperature and concentration variables also exhibit similarity (see Ref. 42, for example). In our isothermal predictive modeling of the turbulent mixing of air and CO_2 , the results of the radial variation of CO_2 mass fractions at different axial locations are available. Abramovich-type normalizations for the mass fraction profiles, however, have failed to yield the universal profiles. Profiles of variables such as the mole fractions of CO_2 or the concentration (in moles/unit volume) of CO_2 have also been unable to conform to similarity considerations.

We found these results somewhat puzzling. Having established the similarity of axial velocity fields, it was difficult to accept that the species field behaves differently. A possible source of this discrepancy is the use of unity Schmidt number for determining the turbulence exchange coefficient for the species field from the values of turbulent eddy viscosity in the predictive calculations. However, this effect is expected to

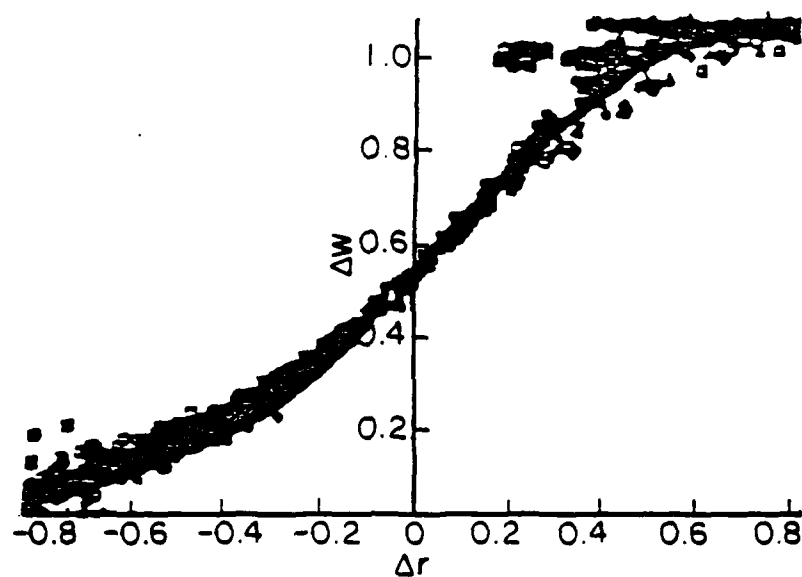


Figure 11. A Composite of all the Predicted and Measured Results.

be generally insignificant. A more serious pitfall may be the rather small amount of CO_2 present (compare a 2 kg/s air mass flow with an 8 kg/hr CO_2 mass flow). The numerical results indicated that the conservation of CO_2 mass was not satisfied over the duct cross section at each axial location--the CO_2 mass flow was underestimated by as much as 50 percent, especially near the forward stagnation point. While the velocity field remained largely unaffected (as evidenced by the similarity) by the failure of the CO_2 mass conservation (in view of the trace amount of CO_2 overall), this was not likely to be true of the radial variation of CO_2 concentrations. Clearly this aspect needed further study. Whether the lack of similarity for CO_2 concentrations was due to the inadequacy of numerical modeling may perhaps be ascertained by examining the APL experimental data (of probe sampling of CO_2) for Abramovich-type normalizations.

SECTION 4

REFINEMENTS AND SELECTED RESULTS

Although the computational results reported in the previous section demonstrated that the TEACH-type numerics and the $k-\epsilon$ turbulence model possessed the capability to predict physically correct flowfields in the centerbody combustor configuration, the comparison with the experimental data found these predictions wanting. Further computational investigations were necessary for obtaining improved predictions. Several areas of refinement were examined and these are discussed in this section.

4.1 INFLUENCE OF DIFFERENCING SCHEMES

Some TEACH code calculations were carried out to study the effects of different differencing schemes on the centerline locations of stagnation points. It had been noted earlier that the TEACH code results underpredicted the forward stagnation point and overpredicted the rear stagnation point. While the latter is expected to be affected by the strong streamline curvature in the vicinity of the rear stagnation point and the failure of the standard $k-\epsilon$ model to include this effect, the amount of numerical diffusion inherent in various differencing schemes appears to affect significantly the former.

In the TEACH code, the convective terms have been discretized through the "hybrid" upwind differencing scheme (see Paragraph 2.4.2). We completed some calculations by replacing this scheme with the power-law differencing scheme (see Paragraph 2.4.3). For the case of 2 kg/s air flow and 8 kg/hr CO₂ flow, the centerline locations of the forward and rear stagnation points (in terms of the centerbody diameter) were as follows. Forward: 0.401 for "hybrid" upwind with fine grid, and 0.428 and 0.44 for power law with fine and coarse grids respectively. Rear: 1.347 for "hybrid" upwind with fine grid, and 1.340 and

1.314 for power-law with fine and coarse grids respectively. We note that the power-law scheme results in 7 to 10 percent increase in the forward stagnation point distance and 0.5 to 2.5 percent decrease in the rear stagnation point distance. Both these changes are in the desired direction but, as pointed out earlier, the rear stagnation point is less sensitive to the change in the differencing scheme.

4.2 CO₂ MASS CONSERVATION

Additional computations were carried out to examine the mass entrainment of one jet by the other. For the ducted flows exemplified by the centerbody combustor configuration, the concept of entrainment is different from that of unconfined (free) jet flows where additional mass is entrained from the ambient fluid. Here, the confining boundary implies that there is no additional mass being entrained, but due to turbulent convection and diffusion, there is a redistribution of the air and CO₂ mass fluxes at different axial and radial locations. This is readily seen in Figure 12. We note that when the annular air flow dominates the flowfield (encountered typically at air flow rates of 2 kg/s and CO₂ flow rates of 4 or 8 kg/hr), the central CO₂ flow is brought to rest on the centerline by the reverse flow of air, carried radially outward, and entrained by the inner region of the annular air.

Before these local redistributions can be quantified, it was necessary to assure ourselves that the global mass conservation was satisfied. Unfortunately, our integrated mass-flow results revealed that while the annular air mass flow is conserved at all axial locations, the central CO₂ mass flow failed to satisfy mass conservation. At axial locations in the vicinity of the centerline forward stagnation point, the integrated CO₂ mass flow was underestimated by as much as 50 percent. Our preliminary results indicated that this discrepancy arose in both "hybrid"-upwind and power-law differencing schemes.

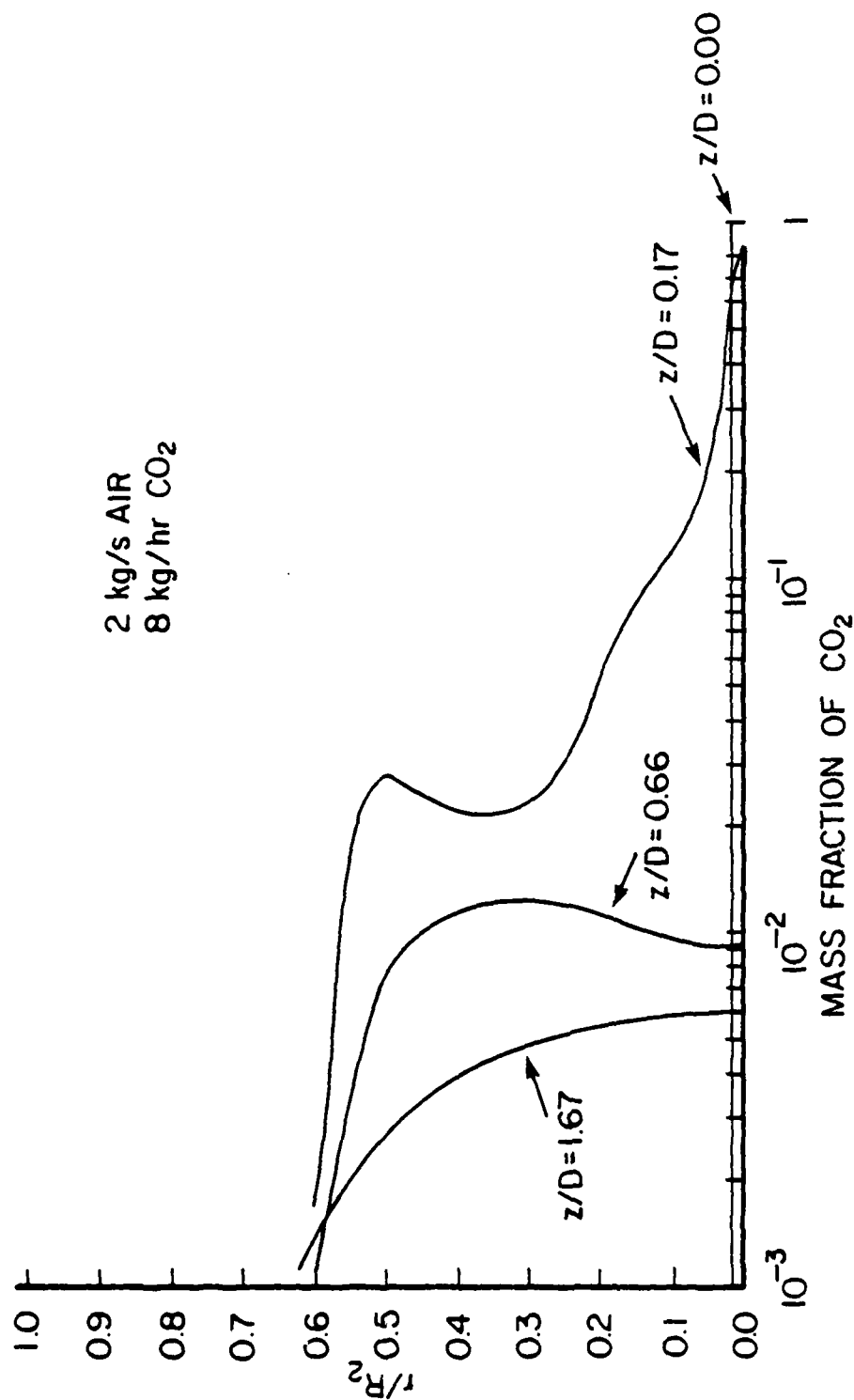


Figure 12. Radial and Axial Distributions of CO₂ Mass Fraction.

An examination of the code showed that the mass conservation was satisfied only for the air/CO₂ mixture through the overall continuity equation in the so-called SIMPLE procedure²⁴ for pressure correction. Note that for CO₂ mass flows of 8 kg/hr and less, the ratio of CO₂ mass flow to air mass flow is of the order of 10^{-3} when the air flow is 2 kg/s. Thus, it appeared that the failure to satisfy CO₂ mass conservation might be traceable to the insignificant contribution made by the CO₂ jet to the total mass flow. Figure 13 shows the integrated axial mass flow of air and CO₂ (per unit radian of the cross section) at different axial locations. Our first set of TEACH code computations employed the value of 0.05 for the inlet turbulence-length-scale parameter λ and the computational grid denoted A. The nodal distribution of this grid is shown in Figure 1. Figure 13 shows that air mass flow satisfies the conservation requirement very well. The CO₂ mass flow, however, increasingly diverges from the conserved value and is off by nearly 20 percent (of the inlet value) at the exit boundary of the computational domain. At the cross section corresponding to the centerline forward stagnation point, the integrated CO₂ mass flow attains a minimum.

It seemed to us that the observed discrepancy in CO₂ mass conservation may be due, at least in part, to poor spatial resolution of the computational grid. In Figure 1 we see that the grid A is characterized by densely populated grid nodes near the centerline and centerbody face and rather sparsely populated nodes near the duct boundary and exit. In particular, the annular region has only eight interior grid points in the radial direction. Although the spatial resolution is quite good toward the bottom left of the computational domain, which is normally the region of interest for the CO₂ jet, under the annular dominant regime considered here the CO₂ jet is turned into the annular region. Thus, the calculations for the CO₂ mass fraction and the integrated mass flow are greatly affected by the poor

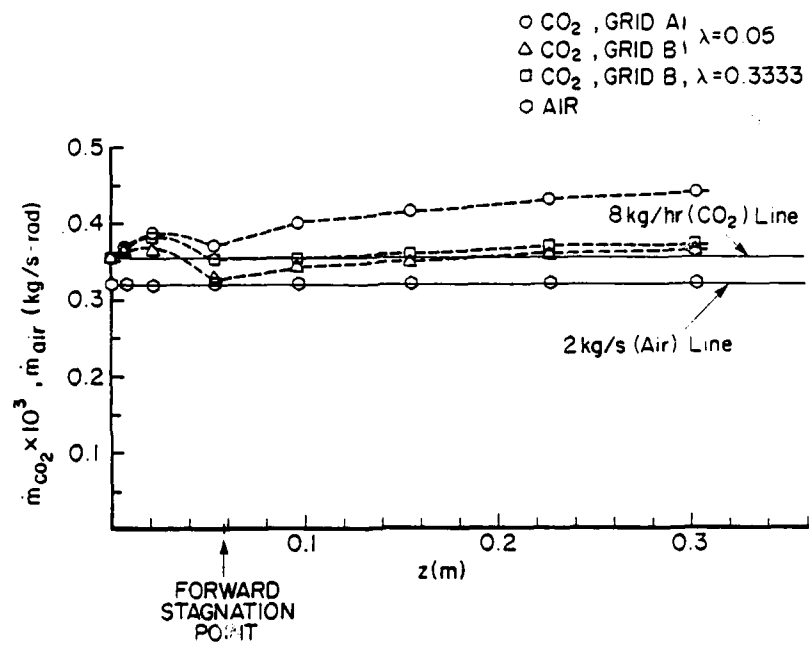


Figure 13. Axial Variation of the Computed Mass Flow Rates of Air and CO₂.

AD-A134 692

LASER DIAGNOSTIC DEVELOPMENT AND MEASUREMENT AND
MODELING OF TURBULENT FL. (U) DAYTON UNIV OH RESEARCH
INST L KRISHNAMURTHY ET AL. JUN 83 UDR-TR-83-04

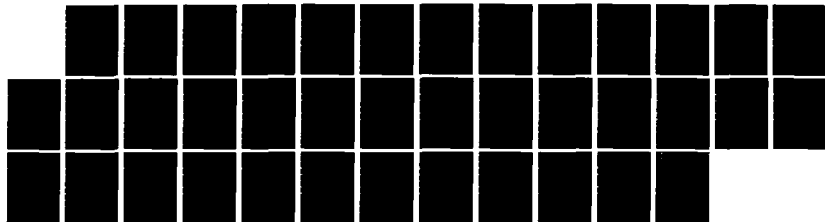
2/2

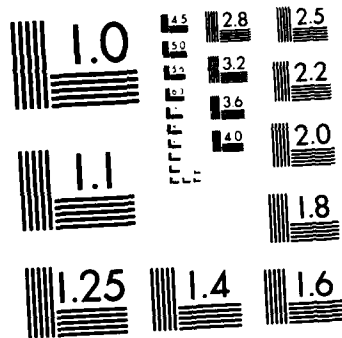
UNCLASSIFIED

AFWAL-TR-83-2044-PT-2 F33615-78-C-2005

F/G 20/4

NL





MICROCOPY RESOLUTION TEST CHART
NATIONAL BUREAU OF STANDARDS-1963-A

spatial resolution in this region, especially in view of the rather small value of CO_2 mass flux. Therefore, a distribution of grid nodes showing better spatial resolution in the annular region can be expected to result in less discrepancy with the conservation requirement. This conjecture also seemed plausible in view of the calculations for the central jet dominant regime (wherein the CO_2 jet "breaks through" the bluff-body recirculation region) which satisfied the mass conservation requirement.

To test this hypothesis, we completed calculations with the grid denoted B shown in Figure 14. By a redistribution of the grid nodes in the radial direction, grid B resulted in thirteen nodes in the interior of the annular region. The results for this case (for $\lambda = 0.05$) seen in Figure 13 indicate that our conjecture is essentially correct. The conservation of CO_2 mass flow is much better everywhere, except near the forward stagnation point. That the spatial resolution of the computational grid may not be the only factor contributing to the question of mass conservation was confirmed by the results shown in Figure 13 for $\lambda = 0.3333$ (the rationale for specifying this value is presented subsequently). However, unlike the grid distribution whose influence is largely numerical, the increase in λ implies large inlet turbulence length scale which results in enhanced turbulence activity in the flowfield. This is expected to augment the turbulent diffusion near the forward stagnation point, thereby reducing the discrepancy in mass conservation in that vicinity.

From the above discussion it would seem that the predictive results would benefit by increased spatial resolution and thus by the use of a greater number of grid nodes than have been employed in our numerical experiments. The observed minimum at the forward stagnation point and the peak between the jet exit and the

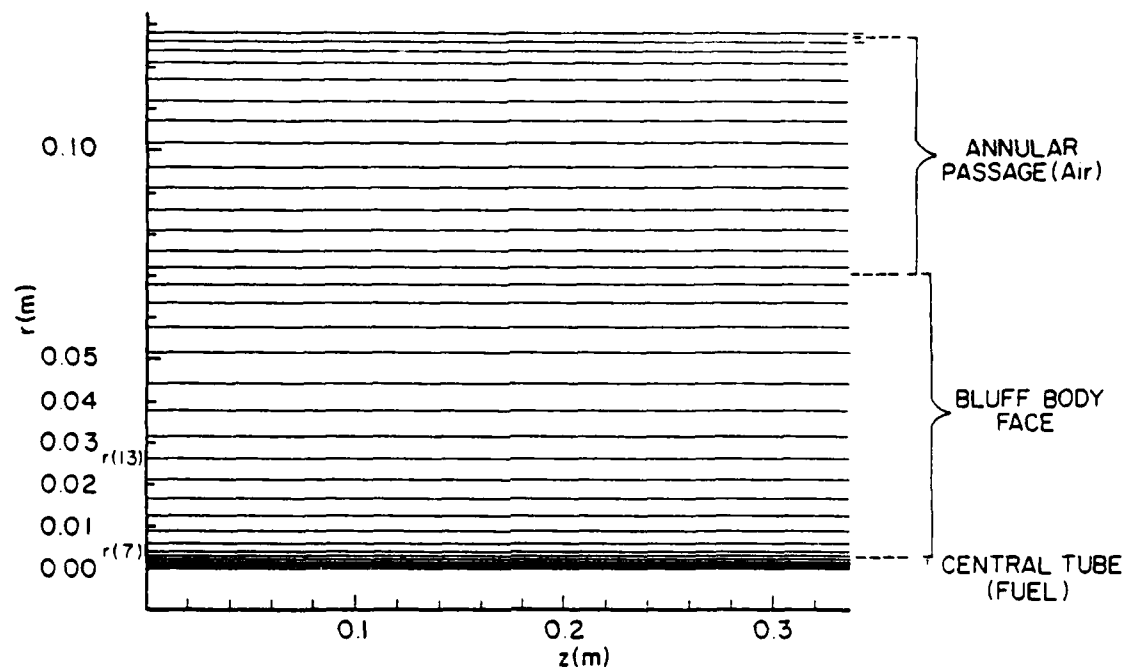


Figure 14. An Arbitrary Modification of the Grid with Increased Spatial Resolution in the Annular Region (GRID B).

forward stagnation point, however, do not seem to be entirely related to the question of spatial resolution.

To explore this aspect further, we have shown in Figure 15 the relative contribution of the diffusive and convective fluxes to the integrated CO_2 mass flow at different axial locations. This shows that at the cross section near the forward stagnation point, the influence of diffusion is the highest, and that while the CO_2 mass flow in the axial direction is largely due to convective transport in a large part of the flowfield, there exist regions where diffusive contribution is no longer negligible. Neglect of diffusive flux can result in a large discrepancy in the CO_2 mass conservation, and was seen to result in as much as 50 percent underprediction of the integrated CO_2 mass flow near the forward stagnation point, as mentioned previously. The results in Figure 13, however, include the diffusive contribution to the total CO_2 mass flow. Thus, the peculiar trend observed upstream of the forward stagnation point remains unclear, except for possible spurious effects arising from numerical diffusion.

4.3 INFLUENCE OF INLET TURBULENCE LENGTH SCALES REVISITED

A number of recent turbulent recirculating flowfield calculations have underpredicted the extent of the recirculation region, the degree of underprediction depending on the configuration, and the turbulence model employed. Our isothermal flowfield modeling of the centerbody configuration with the version of the TEACH code available to us, however, has resulted in an overprediction of the centerline location of the reattachment point due to the annular jet around the centerbody. At the same time, a second stagnation point located farther upstream, due to the introduction of a weak central jet, has been generally underpredicted. The numerical results reported by Sturgess and Syed⁶ also exhibit this overprediction of the rear stagnation point and underprediction of the forward stagnation point. But

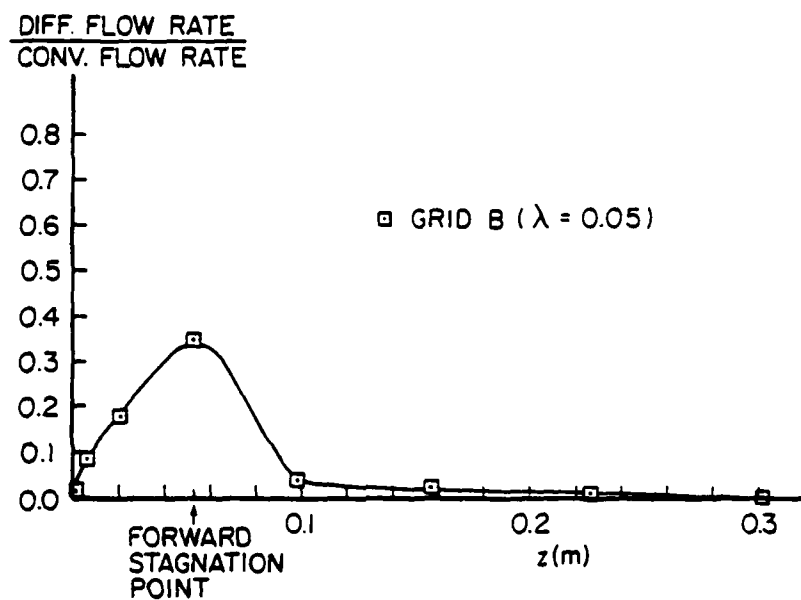


Figure 15. The Relative Importance of Diffusion to the Total CO_2 Mass Flow Rate at Different Axial Locations.

the degree of overprediction of the rear stagnation point location was much less than that seen in our results. Since our preliminary sensitivity tests (discussed in Paragraphs 3.1.2 and 3.2.2) with respect to several parameters of the numerical model had not explained the source of the discrepancy, it was of interest to examine this question further.

Our subsequent examination of the code and the $k-\epsilon$ model therein revealed that the answer to the above difficulty lay in the specification of the inlet turbulence length scales. This subject has been discussed at length in Paragraphs 2.2 and 2.4 and it was essential that the distinction between the length scales ℓ_1 and ℓ_2 [see Eqs. (7b) and (9b) respectively] be taken into account in the proper specification of the inlet length scale.

It was reported by Sturgess and Syed⁶ that the rear stagnation point location on the centerline is very sensitive to the inlet length scale and hence the value of λ . The value of λ used in their calculations was 0.03. Our earlier sensitivity tests examined the range of 0.005 to 0.05 (see Tables 7 and 8) for the value of λ and discerned very little influence on the stagnation point location. However, as noted previously, different formulations (ℓ_1 or ℓ_2) have been used in these studies. Since $\ell_1 = \ell_2 / C_\mu$ [and $\ell_2 = 0.03 (R_2 - R_1)$], our previous parametric range of 0.005 through 0.05 was very much smaller than a value of $\lambda = 0.3333$ which arises from the requirement for consistency [i.e., $\ell_1 = \lambda (R_2 - R_1) = \ell_2 / 0.09 = 0.03 (R_2 - R_1) / 0.09 = 0.3333 (R_2 - R_1)$]. Accordingly, the problem of centerline axial velocity characteristics and stagnation-point locations was reexamined, in anticipation that the TEACH predictions would show better comparison with the experimental data.¹⁰

Numerical experiments were conducted with different values of λ , viz., 0.05, 0.3333, and 0.5556. Note that these

corresponded respectively to the arbitrarily small value used in our earlier studies, the "standard" value of Sturgess and Syed⁶ and the value used by Leschziner and Rodi.³³ Furthermore, with $c_\mu = 0.09$, $\lambda = 0.3333$ corresponds to the length scale of three percent of the reference length and $\lambda = 0.5556$ corresponds to five percent of it ($0.05/0.09 = 0.5556$).

Figure 16 shows the results of the centerline forward and rear stagnation points for a fixed annular air flow of 2 kg/s and a number of central CO₂ flow rates. Identical values of ALAMDA and TURBIN (0.03) in our numerical experiments and those of Sturgess and Syed⁶ facilitate the comparison. The grid systems A and B in our experiments are those denoted in Figures 1 and 14 (B displaying a more dense grid in the annular region than A). We note that our results with the grid system A show good agreement with those of Sturgess and Syed.⁶ It would seem that their grid system is very similar to ours. However, it should be noted that their results are based upon the computational domain with the exit-plane boundary located at 0.8 m from the centerbody face.⁶ However, this boundary is only 0.3 m away in our calculations. Therefore, it appears that the computed results are not significantly affected over this range of exit-plane locations, so long as the exit boundary is located sufficiently downstream of the rear stagnation point. To the extent that numerical predictions show excellent agreement with each other, the degrees of their underprediction of the forward stagnation points and the overprediction of the rear stagnation points with respect to the measured data¹⁰ are similar.

Our results with the two different grid systems indicate the appreciable grid sensitivity, especially for the rear stagnation points. Although the choice of grid B resulted in improved CO₂ mass conservation (see Figure 13), its predictions of the rear stagnation points are worse than those of grid A. In view of the

$\lambda=0.3333$, TURBIN 0.03
 ◇ GRID SYSTEM A (41 x 34)
 ○ GRID SYSTEM B (41 x 34)
 — STURGESS & SYED (39 x 39) (Reference 6)
 ●, ■ EXPERIMENT (Reference 10)

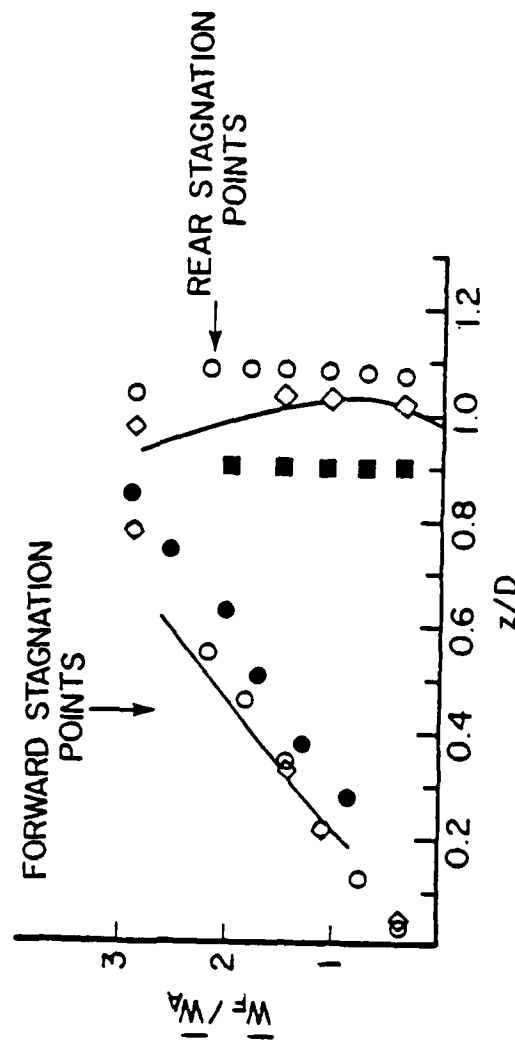


Figure 16. Centerline Forward and Rear Stagnation Points.

fixed number of grid nodes employed in these two grid systems, a mere redistribution of the grid points over different regions of the flowfield can only result in different aspects of the flowfield predictions displaying varying degrees of "success." What is clearly established here is that the numerical modeling could do better with increased spatial resolution everywhere in the computational domain. That the predictions of the forward stagnation points by the two grid systems do not significantly differ from each other is merely a consequence of the fact that the spatial resolution in the vicinity of the central jet is essentially the same for both grid systems.

Figure 17 presents the centerline stagnation point results for different values of λ . The grid system B is chosen in this comparison in anticipation of the subsequent discussion on the curvature correction (whose performance is better evaluated with the poorer predictions of grid B). We observe that as λ increases, the rear stagnation point moves upstream significantly. This behavior has been noticed by Sturgess and Syed⁶ also. The effect on the forward stagnation point is not that strong, especially since the curvature correction with $\lambda = 0.5556$ tends to result in an opposite effect (although in better agreement with the experimental data¹⁰). Of greater significance is the dramatic reduction in the overprediction of the rear stagnation point as λ increases from 0.05 (a value used in our earlier studies) to 0.3333. Thus, a major discrepancy noted earlier between our TEACH predictions and those reported elsewhere⁶ has been resolved to our satisfaction.

We note here that the influence of the inlet length scale on the forward and rear stagnation points recalls our earlier numerical experiments (discussed in Paragraph 3.2.2.2) to determine the effect of c_u . These calculations were carried out for the UCI configuration which is roughly a 1/5-scale model of

TURBIN 0.03, GRID SYSTEM B
(2kg/s Air)

○ $\lambda = 0.3333$

□ $\lambda = 0.05$

△ $\lambda = 0.5556$ (With Curvature Correction)

●, ■ EXPERIMENT (Reference 10)

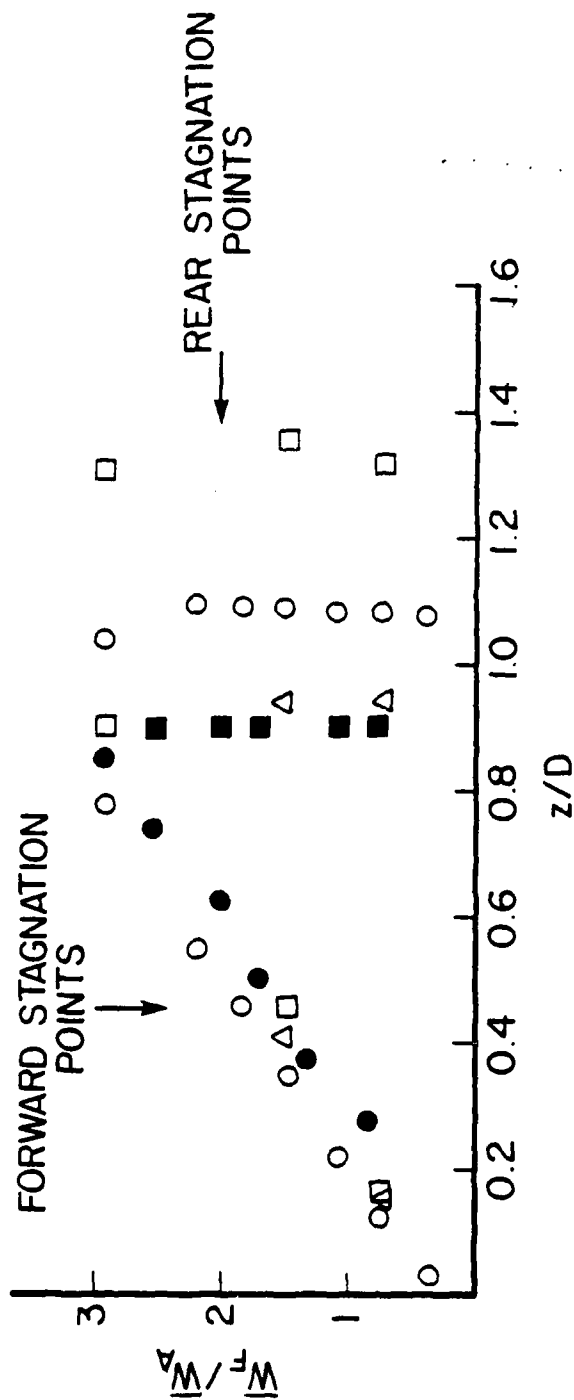


Figure 17. Influence of Inlet Turbulence Length Scale and Curvature Correction on the Centerline Stagnation Points.

the APL configuration. These results are shown in Figure 3. We note that although the values of λ and σ_ϵ employed in this experiment are different from those in Figure 17, the trend is similar to the length-scale experiment, in that both stagnation points move upstream, with the rear stagnation point more strongly affected than the forward stagnation point. However, it must be pointed out that in the $k-\epsilon$ model, the equilibrium-turbulence assumption implies that the two constants c_μ and c_D vary together, so that $c_\mu \cdot c_D = 0.09$ (see Reference 28). Our computational experiment varied only c_μ .

It seems that larger values of c_μ or larger values of inlet-length scale imply higher values of turbulence eddy viscosity. Therefore, the results obtained with the variation of c_μ or λ (Figures 3 and 17) suggest that a higher level of turbulence activity results in shorter recirculation length. There seems to be some experimental evidence to support this conclusion. For example, an experimental comparison⁴⁶ of cold-flow and combustor-flow recirculation lengths revealed that the turbulence level was much lower and the recirculation length was much larger in combustor flows than in cold flows. The centerline measurements¹⁰ of the axial components of the mean velocity and turbulent intensity in isothermal and combustor flows on the centerbody combustor configuration, however, do not demonstrate this behavior. While the recirculation lengths are indeed larger in combustor flows than in cold flows, there is no clear evidence that the combustor flows indicate decreased turbulence activity in comparison with the cold flow.

4.4 STREAMLINE CURVATURE EFFECTS IN TURBULENCE MODELING

That the streamline curvature has a strong influence on the shear-flow turbulence is well known in the literature. Indeed, this was the topic in the comprehensive monograph by Bradshaw.³² Since the size of the recirculation region appeared to depend

strongly on the turbulence activity (as indicated in the previous section) in the curved shear layers bordering this region, and since the "standard" $k-\epsilon$ model (discussed in Paragraph 2.2) does not account for the curvature effects, it was considered worthwhile to reexamine the discrepancies between predicted and measured results in the light of streamline-curvature corrections implemented in the code (as outlined in Paragraph 2.3).

Numerical calculations were carried out by introducing a curvature-dependent c_μ (see Paragraph 2.3 for details) into the "standard" $k-\epsilon$ model, along the lines suggested by Leschziner and Rodi.³³ We emphasized earlier the ad hoc nature of these corrections. Furthermore, our numerical experiments are not complete and only a limited parametric range of centerbody-flowfield conditions has been considered so far. However, the results reported here do indicate that the curvature modification we have incorporated results in changes in the desired direction.

The computed contour of the curvature-dependent c_μ is seen in Figure 18. It is clear that the constant value of 0.09 for c_μ is valid only in a limited region of the flowfield (and outside the recirculation region). To the right of the $c_\mu = 0.09$ contour, there are local regions of higher values of c_μ (up to 0.18). Inside the recirculation region, however, the constancy of c_μ is seen to break down dramatically. We note that the correction leads to a significant reduction in c_μ in the vicinity of the separated streamline (i.e., in the curved shear layer bordering the recirculation region). The value of $c_\mu = 0.025$ was (as noted in Paragraph 2.3) an arbitrarily chosen lower limit in the computations, without which c_μ would become zero or even negative within the shaded region (where the concept of local equilibrium of turbulence, on which the curvature correction is based, is unlikely to remain valid). Our computed c_μ contour is quite similar to that obtained for the axisymmetric, unconfined

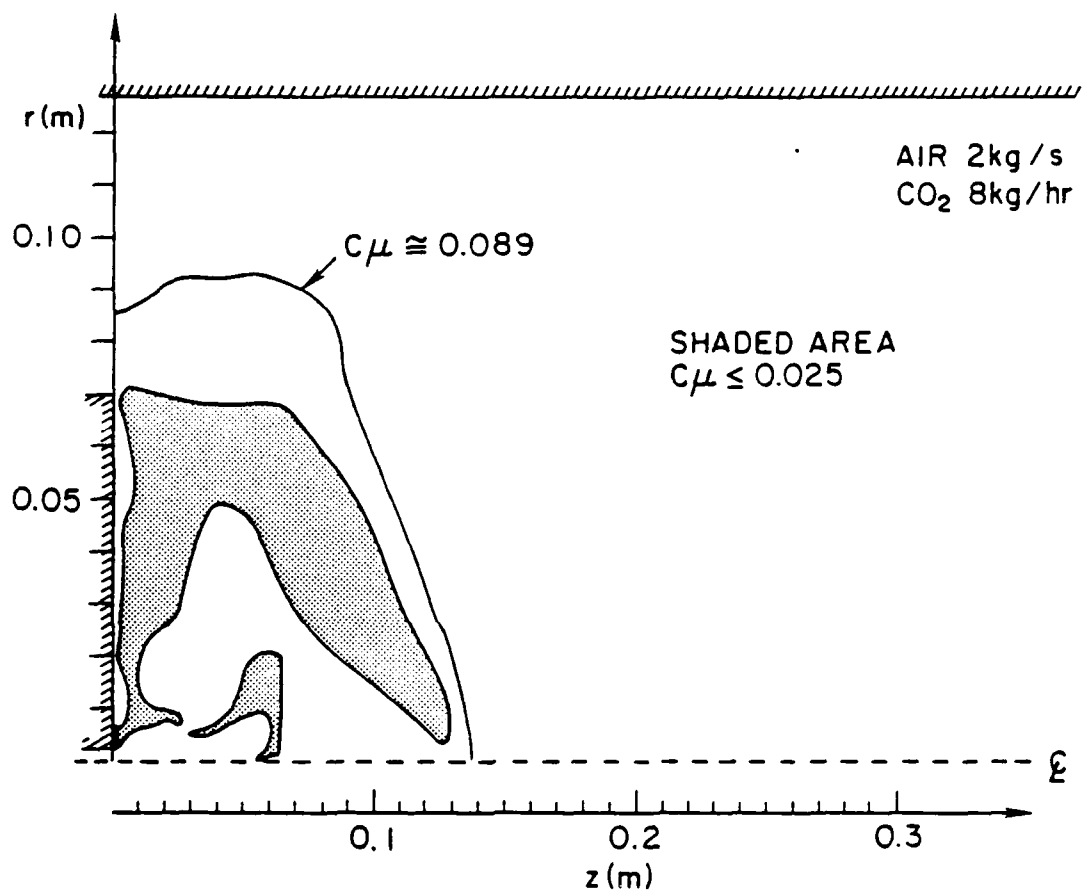


Figure 18. Distribution of Curvature Corrected c_{μ} .

annular jet of Reference 33, except for the more complicated nature of the contour near the centerline which results from the presence of the central jet in our configuration. Note that the centerline location near the forward stagnation point is characterized by the low c_u region. This appears to confirm our suspicions that the underprediction of the forward stagnation point is traceable to too high a c_u value (see Figure 3) employed there under the constant c_u model.

The centerline stagnation point results with the curvature correction are seen in Figure 17. For the two data points (viz., CO_2 flow of 4 and 8 kg/hr) shown in the figure, the effect of curvature correction is somewhat masked by the increase in the inlet length-scale parameter λ from 0.3333 to 0.5556. However, the effect of increasing λ (without curvature correction) is to move monotonically both the forward and rear stagnation points upstream. This results in much greater underprediction of the forward stagnation point. When the curvature correction is introduced, the forward stagnation point is moved farther downstream and closer to the measured value. Clearly, the prediction with $\lambda = 0.5556$ is better than that with $\lambda = 0.3333$. In the case of the centerline rear stagnation points, the effect of the increase in λ and the curvature correction is to reduce the degree of overprediction and to lead to better agreement with measured values. This observation becomes clearer from an inspection of Figure 19 which presents the centerline decay of the mean axial velocity. For the case of 8 kg/hr CO_2 flow, we see that the mean axial velocity profile shows better agreement between prediction and measurement with curvature correction (for $\lambda = 0.5556$) than without it. Also noticeable is the reduced underprediction of the forward stagnation point and the reduced overprediction of the rear stagnation point due to the introduction of the curvature correction. Of course, in the reverse-flow region, the uncorrected profile seems to be in better agreement

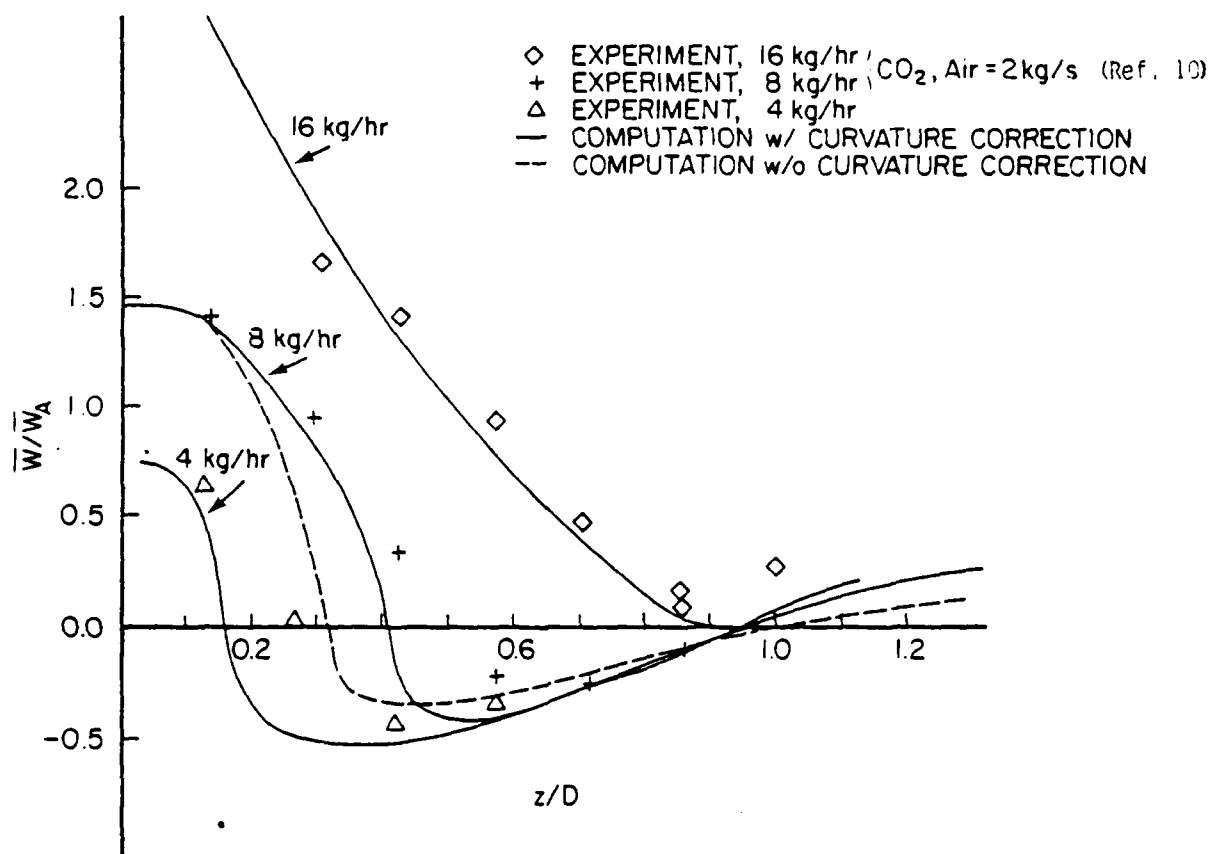


Figure 19. Effect of Streamline Curvature Correction on the Centerline Mean Axial Velocity Profiles.

with measurements in the vicinity of $z/D \sim 0.6$. This emphasizes the ad hoc nature of the curvature correction.

The other noteworthy feature of Figure 19 is the excellent agreement between the measured and predicted profiles for the CO_2 flow of 16 kg/hr. As seen in Figure 17, this flow rate is predicted to result in the occurrence of centerline reverse flow (with both stagnation points being present) for $\lambda = 0.3333$ and without curvature correction. However, in Figure 19 it is seen that for $\lambda = 0.5556$ and with correction for curvature effects, the 16 kg/hr CO_2 flow just achieves "breakthrough" of the recirculation region. Since the experiments¹⁰ implied a "breakthrough" flow rate of 14.7 kg/hr, the curvature-corrected results exhibit better agreement with the experimental data than did the uncorrected predictions. Indeed, the present LDA results (e.g., see Figure 32 of Reference 47) show that the centerline flow reversal is still present at the CO_2 flow rate of 16 kg/hr. Thus, the earlier implication that the "breakthrough" occurred at a flow rate of 14.7 kg/hr is incorrect. In the light of the recent experimental data, it also appears that the "standard" $k-\epsilon$ model (i.e., without accounting for streamline curvature effects) predicts the APL flowfield better than the comparison with the earlier measurements¹⁰ had indicated. This becomes clear in the following discussion.

4.5 COMPARISON OF PREDICTIONS WITH THE NEWER EXPERIMENTAL RESULTS

In the previous paragraphs the influence of the differencing schemes, inlet turbulence-length scales and streamline-curvature effects on the numerical predictions was discussed. Before we conclude this section, the numerical predictions are examined in terms of the recent APL data on the velocity⁴⁷ and CO_2 concentration⁴⁸ fields.

4.5.1 Centerline Variation of the Mean and rms Axial Velocity Fields

The normalized profiles of the centerline mean and rms axial velocity components for three different CO₂ flow rates are shown in Figures 20 through 22. The predictions were based upon the (41 x 34) computational grid, the "hybrid" upwind differencing scheme and the "standard" k- ϵ model. The value of λ was 0.5556 for the case of zero CO₂ flow and 0.3333 for the other two cases.

The experimental data for the mean axial velocity for the CO₂ flow rates of 0, 6 and 16 kg/hr differ from the previous results.¹⁰ The locations of the rear stagnation point are at a z/D of 1 in Figure 20, slightly greater than 1 in Figure 21 and slightly less than 1 in Figure 22. The measurements in Figure 22 for 16 kg/hr also indicate that for $0.75 < z/D < 0.975$ the centerline-flow reversal is present. The earlier results,^{10,43} on the other hand, indicated that the rear stagnation point was at a z/D of 0.9 (e.g., see Figure 16) and that the minimum centerline mean axial velocity at 16 kg/hr was a finitely large positive value (e.g., see Figure 19). Thus, the newer experimental results show better agreement with the present predictions and those of Reference 6.

The agreement between the measurement and prediction for the mean velocity is generally good upstream of the rear stagnation point, except for the underprediction in Figures 20 and 21 between the location of the peak negative velocity and the rear stagnation point. Because of the very small region of flow reversal in Figure 22, there is much less disagreement at the highest CO₂ flow rate. Indeed, a comparison of Figures 19 and 22 reveals that the predictions with and without curvature effects at 16 kg/hr do not differ significantly. This should not be surprising since the central jet essentially "breaks through" the recirculation region and consequently does not suffer the large

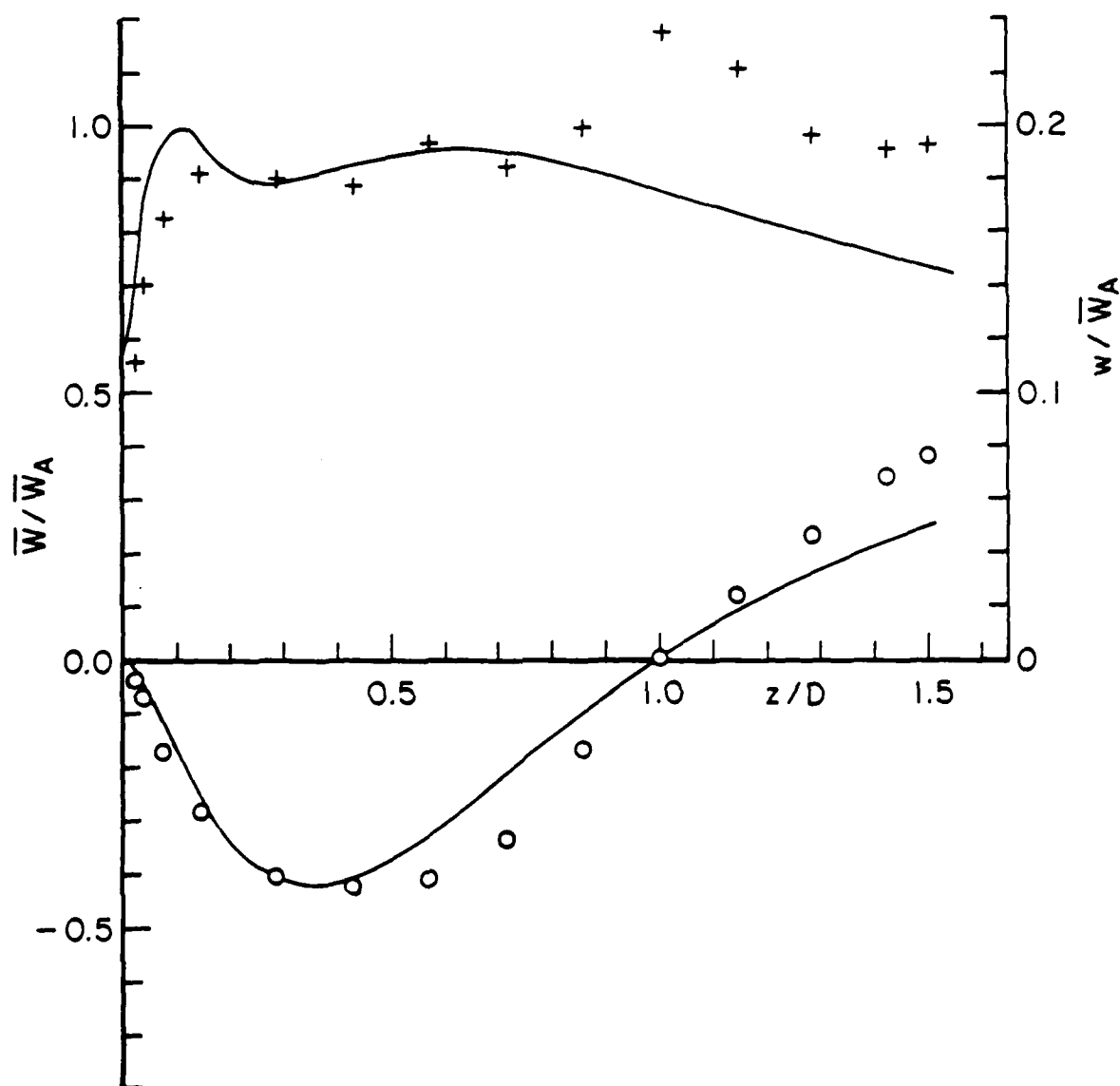


Figure 20. Centerline Mean and rms Axial Velocity Profiles for 2 kg/s Air Flow and Zero CO₂ Flow. Measurement (Ref. 47) O: Mean +: rms Prediction —: Standard k- ϵ Model.

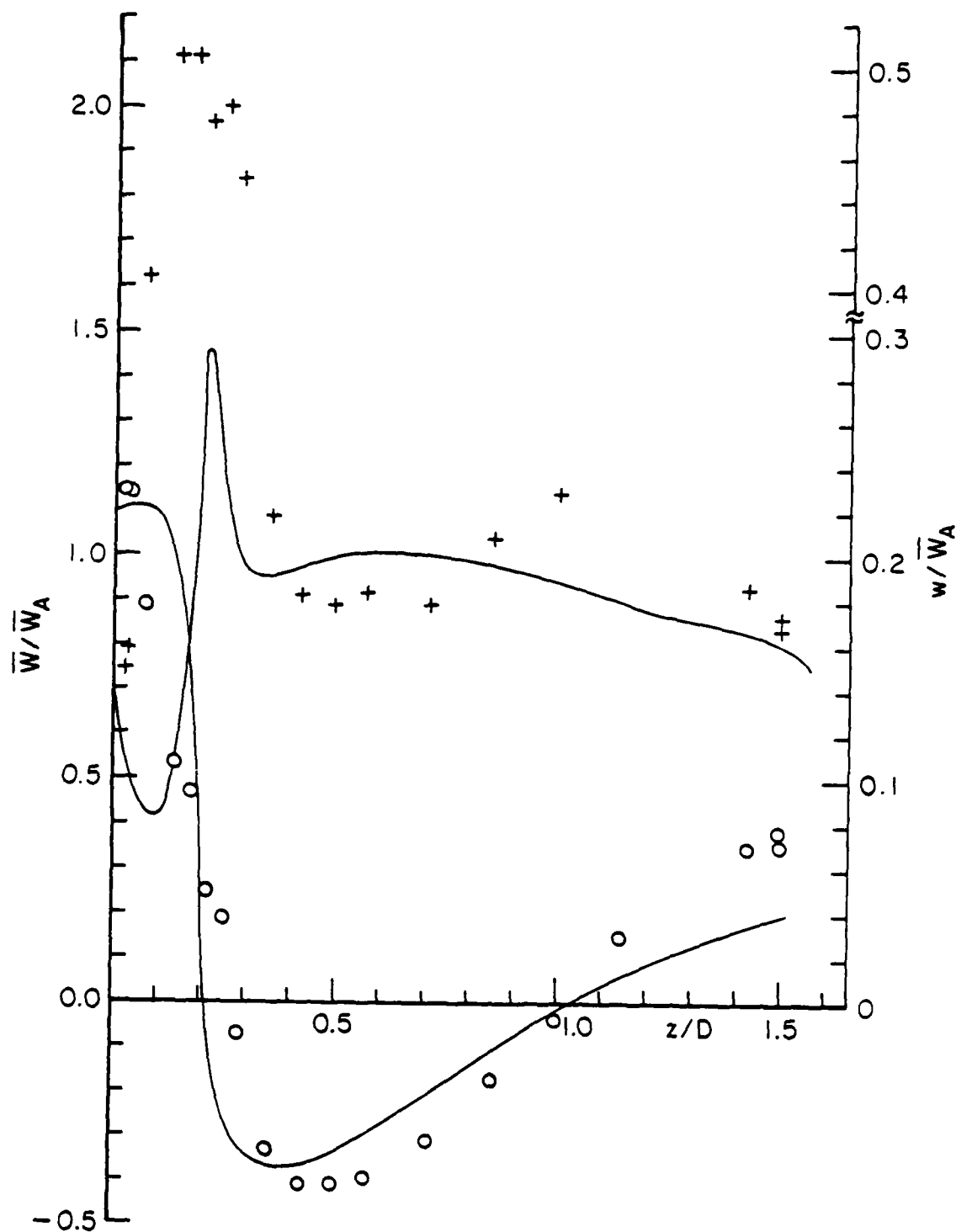


Figure 21. Centerline Mean and rms Axial Velocity Profiles for 2 kg/s Air Flow and 6 kg/hr CO₂ Flow. See Figure 20 for Legend.

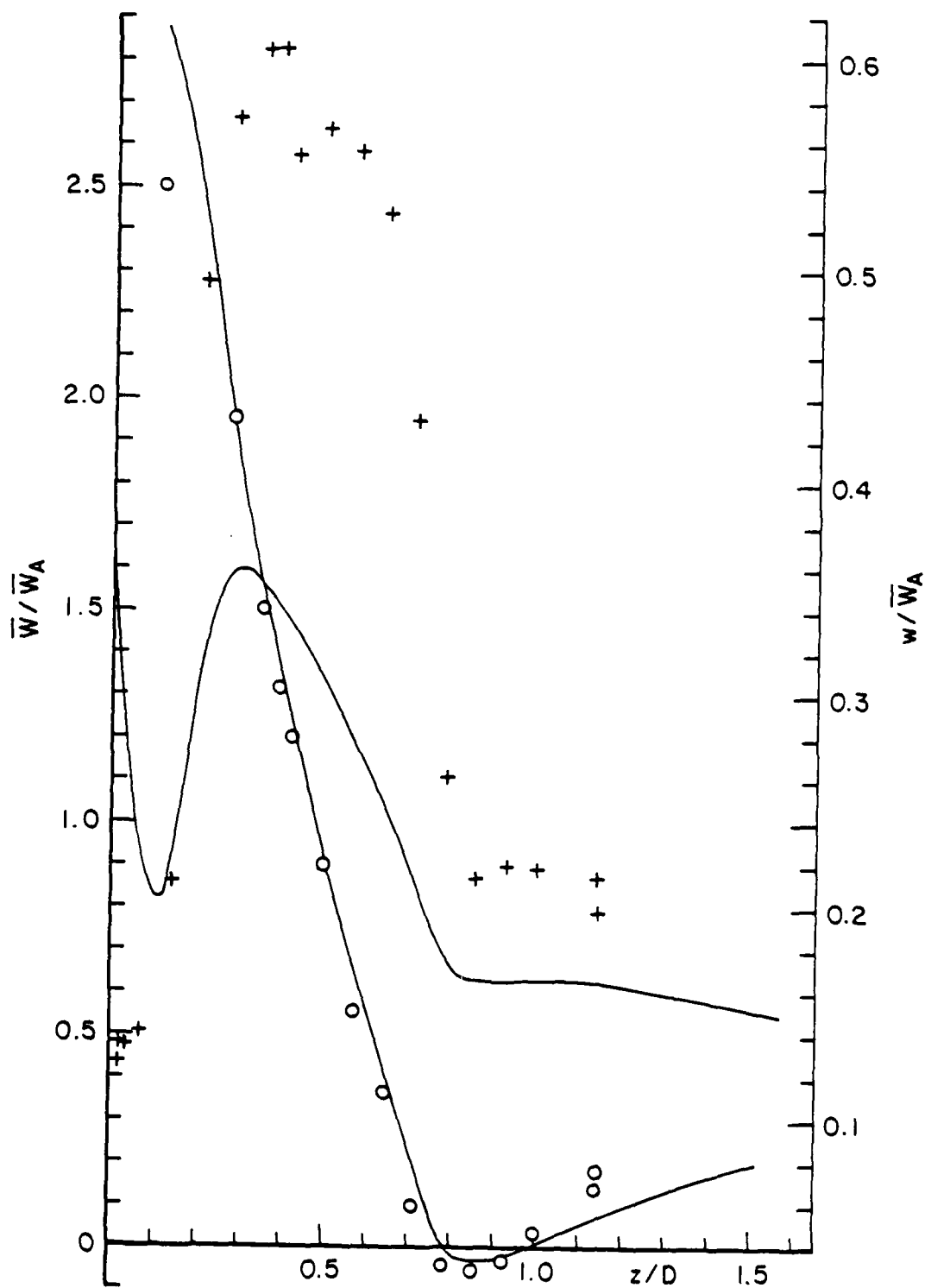


Figure 22. Centerline Mean and rms Axial velocity Profiles for 2 kg/s Air Flow and 16 kg/hr CO₂ Flow. See Figure 20 for Legend.

streamline curvature effects associated with the recirculating flow. Finally, the measured recovery of the mean axial velocity downstream of the rear stagnation point is greater than that given by the prediction for all the three CO₂ flow rates. This feature seems to be characteristic of the "standard" k-ε model, presumably reflecting that the isotropy assumption in the model may be invalid and that the curvature effects may be significant. This difference between the measured and predicted recovery rate is also consistent with the difference noted between the measured and predicted rms axial velocity component in Figures 20 and 21. The experimental results show a peaking and a subsequent more rapid decay of the turbulence intensity, while the predicted results indicate a continuously decreasing trend at a slower rate.

Figure 21 shows that the measured forward stagnation point occurs at $z/D = 0.28$. Although the calculation still underpredicts this location, the recent measurement shows better agreement with the present predictions and those of Reference 6. For example, according to the earlier measurement¹⁰ (see Figure 16), the forward stagnation point at 6 kg/hr occurred at a $z/D \sim 0.4$ which indicated considerable underprediction by the calculations. The much closer agreement between the predictions and the recent measurement may be attributed, at least in part, to the crucial difference in the central-jet exit configuration in the two measurements. The recent experiments employed a well-designed nozzle with a contraction ratio of 2.56 (e.g., see Figure 16 in Part I of this report), thereby ensuring a nearly uniform exit-velocity profile and thus conforming more closely to the assumed uniform profile in the calculations. The earlier experiments⁴³, however, involved a straight tube 15 diameters in length upstream of the exit plane, thereby resulting in a nonuniform exit-velocity profile. Clearly, the latter configuration leads to a larger centerline axial velocity than the former (under identical mass flow rates) and consequently to

a larger value for the location of the forward stagnation point. While this difference in the central-jet geometry accounts for the appreciable decrease in the location of the forward stagnation point, it is unlikely to have contributed to the observed increase in the location of the rear stagnation point.

The quantitative agreement between the measurement and prediction for the rms axial velocity in Figures 20 through 22 is generally poorer than for the mean velocity. For all three CO₂ flow rates, the predictions show the observed trend (except for the peaking near the rear stagnation point in Figures 20 and 21). For example, in Figure 21 we see that both measurement and prediction show the sharp peak in the rms component in the vicinity of the forward stagnation point. Likewise, in Figure 22 there is reasonable agreement for the location of the sharp peak (indicating, perhaps, the transition to turbulence) between the prediction and measurement. As noted earlier, the assumed isotropic turbulence and lack of accounting for curvature effects in the turbulence model, among other things, suggest that the agreement between the prediction and measurement of the turbulence structure in the centerbody flowfield is unlikely to be as good as that noted for the mean velocity field.

4.5.2 Centerline Variation of CO₂ Concentration

Figures 23 and 24 show the comparison of the predicted centerline mole fraction of CO₂ with the APL (intrusive) gas sampling measurements.⁴⁸ The agreement between the prediction and measurement for the overall trend in both CO₂ flow rates is good. The quantitative agreement for 16 kg/hr is better than that for 6 kg/hr. This behavior appears consistent with that noted for the mean axial velocity in Figures 21 and 22.

We note that the earlier anticipated trends⁵ of the centerline CO₂ concentrations showing a rapid decay first and an equally rapid approach to uniform values subsequently in the

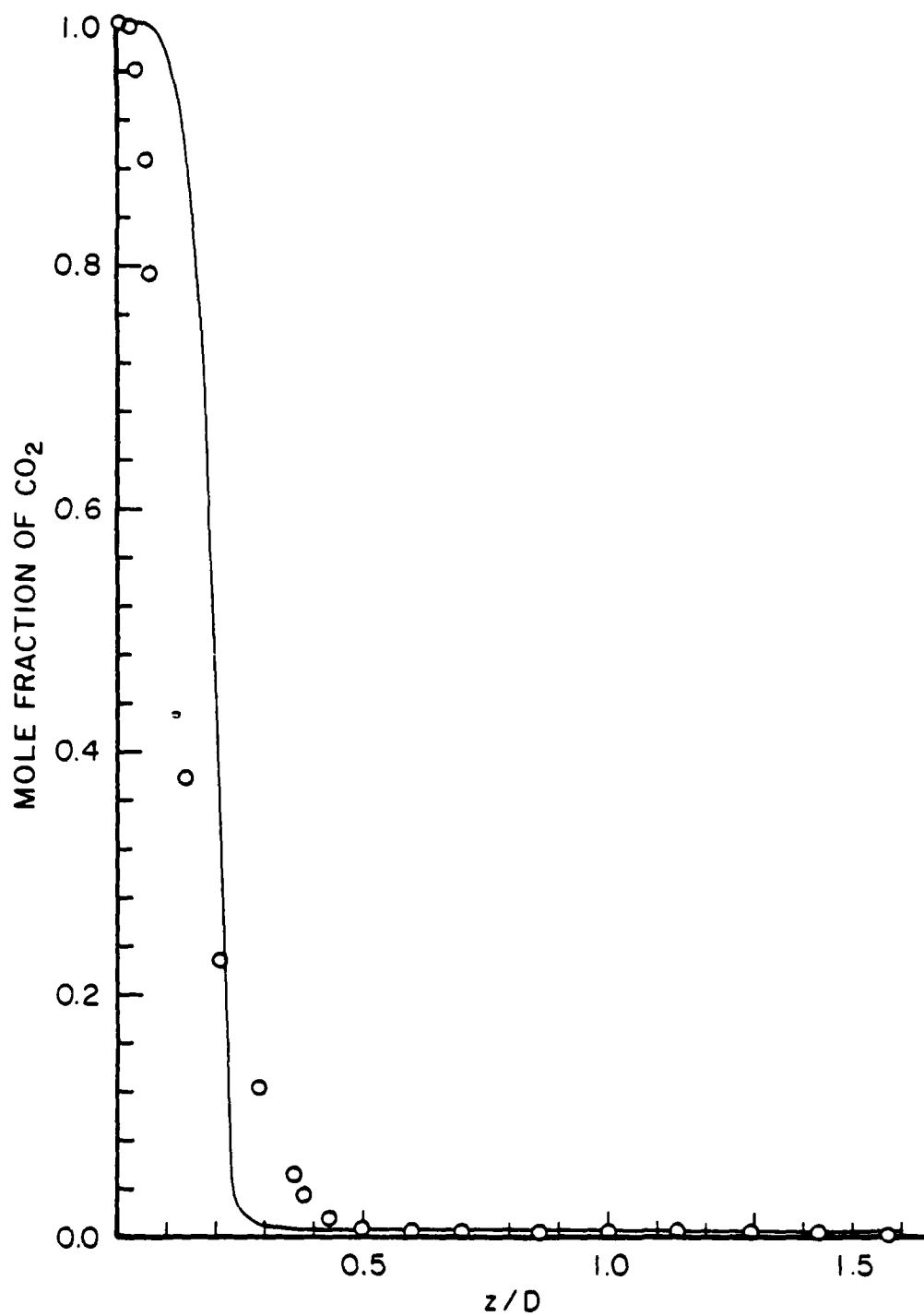


Figure 23. Centerline CO₂ Mole Fraction for 2 kg/s Air Flow and 6 kg/hr CO₂ Flow. O: Measurement (Ref. 48)
— Prediction: Standard k- ϵ Model.

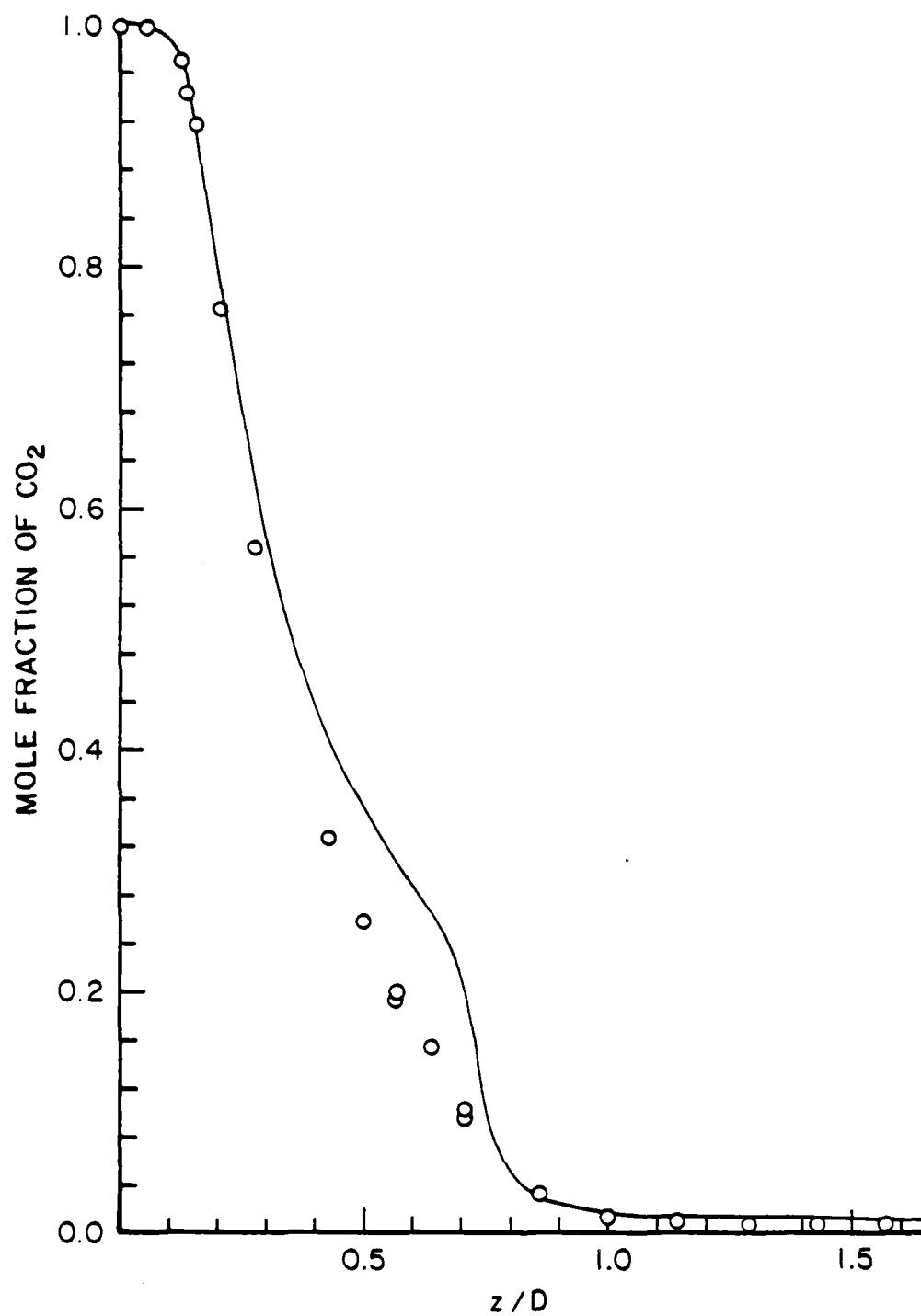


Figure 24. Centerline CO_2 Mole Fraction for 2 kg/s Air Flow and 16 kg/hr CO_2 Flow. See Figure 23 for Legend.

annular-flow dominant condition have been confirmed by the present predictions and measurements.⁴⁸ Furthermore, as can be seen by comparing Figures 21 and 23, and 22 and 24, the points of intersection obtained by extrapolating the portions of the profiles that denote the rapid decay and the approach to uniformization in Figures 23 and 24 fall very close to the forward stagnation points of Figures 21 and 22 respectively. In view of the rationale presented in Reference 5 for expecting the turning of the centerline concentration profile to occur in the vicinity of the forward stagnation point, the internal consistency demonstrated by both the predictions and measurements is gratifying.

4.5.3 Comparison of the Measured and Predicted Streamlines

It is instructive to examine the time averaged contours⁴⁹ of the normalized stream function shown in Figure 25. The normalization is with respect to the inlet annular air mass flow of 2 kg/s. The contour labelled 11 denotes the zero stream-function contour which separates from the centerbody surface and meets the centerline at the rear stagnation point. The contours (outside the separated streamline) labelled 1 through 10 denote the (nonrecirculating) annular stream. The closed contours labelled 12 through 18, confined between the centerline, the centerbody face and the zero stream-function contour, represent the time-averaged recirculating vortex.

The upper part of Figure 25 corresponds to the measured contours, reproduced from Figure 30 of Part I of this report. Unlike the smooth contours of Figure 30, the contours in Figure 25 were obtained by AFWAL/POSF through computer graphics.⁴⁹ The lower part of Figure 25 corresponds to the predicted contours obtained from the TEACH-Code computations performed on the MODCOMP computer system at AFWAL/POSF by Mr. J. S. Stutrud.⁴⁹

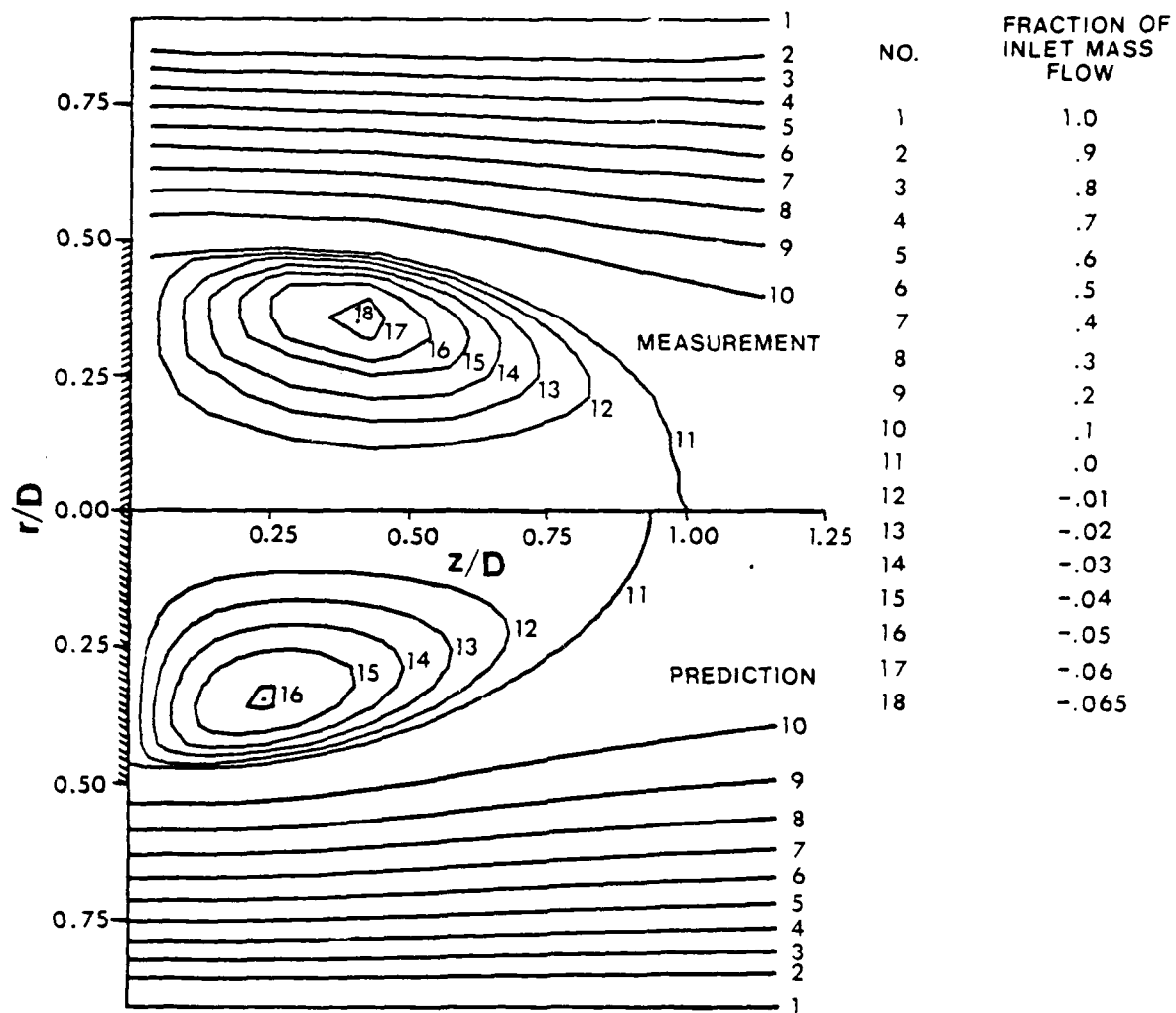


Figure 25. Streamline Contours for 2 kg/s Air Flow and Zero CO₂ Flow.

The comparison of the measured and predicted contours reveal several interesting features. The axial extent of the recirculation region is slightly underpredicted. This conforms to the earlier experience of several investigators. There is a progressive degree of underprediction of the reverse-mass flow contours. The strength of the vortex expressed in terms of the peak negative mass flow is measured to be 6.5% of the inlet mass flow (the contour labelled 13 is taken to represent the vortex center which corresponds to the negative maximum). The predicted value is about 5.1% of the inlet mass flow. The FREP-Code calculations (which employed a constant eddy-viscosity model) in Reference 5 predicted the strength of the vortex to be 5.87%. This indicates that the "standard" $k-\epsilon$ model tends to underpredict the strength of the vortex. Since Figure 19 shows that the prediction accounting for streamline curvature effects results in a higher peak negative axial velocity (and consequently a higher vortex strength), it would seem that the interior of the recirculating region is significantly influenced by curvature effects.

The above conclusion is also borne out by an examination of the location of the vortex center. The measurement in Figure 25 indicates that the axial and radial coordinates (normalized by the centerbody diameter D) of the vortex center are respectively 0.43 and 0.35. The predicted results from Figure 25 are 0.26 and 0.35. The predicted values reported in Reference 5 are 0.3 and 0.35. The very good agreement seen in Figure 25 between the predicted and measured radial coordinate is surprising, especially when there is significant underprediction of the axial coordinate. Also, the identical value predicted by the constant eddy-viscosity model⁵ and by the more realistic $k-\epsilon$ turbulence model here implies that the details of turbulence model do not have much effect on how far the vortex center is radially displaced from the centerline. Indeed, as noted in Reference 5, the radial coordinate in terms of the duct diameter is 0.19 and

this is quite close to the value of 0.18 reported by Ko and Chan⁴⁴ for their unconfined annular jet. In view of their observation that the radial position of the vortex center is essentially independent of the momentum flux of the annular jet (and thus the pressure available for entrainment behind the centerbody face), it appears that the radial coordinate is determined more by the geometry than by the flowfield details.

The disagreement noted for the axial coordinate (between the measurement and prediction in Figure 25 as well as between the previous⁵ and present predictions), however, indicates that the axial coordinate does depend on the flowfield structure. A possible line of speculation in this regard is suggested by the results of Ko and Chan⁴⁴ which show that the axial coordinate decreases with increasing nondimensional momentum flux of the annular jet and consequent increasing entrainment behind the centerbody face. The present discussion is not concerned with the variation in the annular momentum flux. Nevertheless, we speculate here that the predictions overestimate the entrainment by the annular jet as compared to the measurement. Likewise, the present k- ϵ model overpredicts the entrainment when compared to the eddy-viscosity model.⁵ Extending this line of speculation further, it would seem that the streamline curvature correction to the k- ϵ model tends to diminish the entrainment and thereby move the axial coordinate of the vortex center further downstream. This conjecture can be verified when the entrainment characteristics of the flowfield are examined through measurement and prediction.

Before concluding this discussion, it is worth mentioning that there are some differences between the MODCOMP predictions⁴⁹ seen in Figure 25 and the predictions seen in Figures 20 through 22. For example, the calculations⁴⁹ employed a (41 x 39) computational grid, a computational domain of 60 cm in the axial direction, power-law differencing scheme and a value of 0.5556 for λ . Accordingly, Figure 20 for the case of zero CO₂ flow

shows a larger value than Figure 25 for both the axial coordinate of the vortex center (which is close to the axial location of the centerline peak negative mean axial velocity) and the rear stagnation point. However, the underprediction (with respect to the measurement in Figure 25) of the axial coordinate remains and our speculative arguments still hold.

SECTION 5

CONCLUSIONS AND RECOMMENDATIONS

In this section the major conclusions from the numerical flowfield modeling of the centerbody configuration are presented, followed by recommendations for further research.

5.1 CONCLUSIONS

a. The numerical modeling has successfully demonstrated the capability of the TEACH-T computer program to provide physically correct predictions of the isothermal turbulent recirculating flowfields of the centerbody combustor configuration.

b. The performance of the "standard" $k-\epsilon$ turbulence model in the TEACH code has been free from the numerical convergence difficulties with the FREP code in earlier modeling activities. Thus, the present modeling avoids any arbitrariness inherent in the assumption of a constant eddy viscosity model.

c. The numerical calculations of the flowfields in both the APL and UCI configurations predict flowfield features that conform to the experimental observations.

d. The present predictions of the APL configuration are in good agreement with the numerical results of this flowfield reported in the literature.

e. In the annular-flow dominant regime where two stagnation points occur on the centerline, the present predictions show much better agreement with the measured results of stagnation points than do the FREP predictions. As in the case of the predicted data available in the literature, the underprediction of the forward stagnation point and the overprediction of the rear stagnation are present to a small extent. This appears to be due to the "standard" $k-\epsilon$ turbulence model which does not include the effects of streamline curvature and the "hybrid" upwind

differencing scheme which retains diffusive effects only for cell Peclet numbers less than or equal to 2.

f. In the central-jet dominant regime (when the annular air flow is very small or when it is completely absent), the centerline decay of the mean axial velocity resembles that of a free jet. Both the normalized velocity data and CO₂ mass fraction data reduce to a single curve which has the characteristic slope of -1, when displayed on a log-log plot. The distinction between small annular flow and zero annular flow in the FREP calculations is not observed in the present work.

g. The present study shows that the radial distributions of the mean axial velocity field exhibit self-similarity when Abramovich-type normalizations of the axial velocity and radial distance are employed. This behavior is noted for both the UCI and APL configurations, for different annular and central jet flow rates (when either the annular jet is dominant, or the central jet is dominant, or neither jet is dominant), and for a range of axial locations (within and without the recirculating region). This similarity is also observed for the measured velocity data in the APL configuration, the unconfined annular jet configuration (Ko and Chan⁴⁴), and the unconfined flow downstream of a disk (Durao and Whitelaw⁴⁵). Although the similarity may remain incomplete in certain cases due to other factors (such as the nonvanishing mean radial velocity component at the inlet for the flow past a disk), it does appear that the measured and predicted results exhibit the tendency toward similarity. We believe that this flowfield similarity may well be a necessary condition for the correctness of the measured and predicted data.

h. With the nonuniform grid spacing adopted for the 41 axial x 34 radial grid-point distribution and the exit plane of the computational domain located at least more than twice the

centerbody diameter from the inlet plane, the present results generally appear to be grid-independent. Sensitivity tests involving grid spacings that are 50% larger and exit plane location that is 50% farther have resulted in centerline stagnation point predictions that vary by less than 10%.

i. Sensitivity tests for the influence on the predicted results of boundary-layer thickness in the inlets, turbulence intensity in the inlets, and the Schmidt number for the dissipation equation do not appear to result in significant variations in the parametric range tested.

j. Sensitivity tests for the influence of the inlet turbulence length scales and the $k-\epsilon$ turbulence model constant c_μ show that the predicted results of the centerline stagnation points are greatly affected by the assumed values of the inlet length scales and c_μ .

k. Modifications of the TEACH code implemented in the present program by the replacement of the "hybrid" upwind differencing with the power-law differencing scheme result in improved numerical predictions, in the limited parametric testing completed.

l. Ad hoc modifications to the "standard" $k-\epsilon$ model for incorporating the effects of streamline curvature through the introduction of a curvature-corrected and hence nonconstant c_μ appear to result in predictions that show better agreement with the experimental data than the predictions with the "standard" $k-\epsilon$ model.

5.2 RECOMMENDATIONS FOR FURTHER ACTIVITY

Based on the foregoing conclusions, we offer the following recommendations for future research in numerical modeling.

a. For isothermal flowfield modeling with the TEACH code, additional improvements in the differencing schemes (e.g., the skew-upwind differencing scheme and the quadratic, upstream-weighted differencing scheme) are possible, and this aspect deserves study.

b. In view of the ad hoc nature of the streamline curvature correction to the "standard" $k-\epsilon$ model implemented in the present program, a more systematic approach and rigorous formulation for including the effects of streamline curvature must be investigated.

c. Isothermal flowfield calculations of the APL and UCI configurations must be carried out with the viewpoint of establishing scaling criteria.

d. Isothermal flowfield calculations of the APL configuration must be performed to establish the influence of annular flow rates and blockage ratios on the location of the vortex centers and the strength of the recirculation region.

e. Modification of the presently available version of the TEACH code or the use of any refined version, if available, must be considered for the modeling of reacting flowfields.

f. When the reacting flowfield predictions are available, the implication of the vortex center on flame stabilization must be studied.

g. Time-dependent flowfield calculations must be performed to investigate the temporal characteristics of the centerbody configuration.

REFERENCES

1. Development of Combustor Flow Analysis, Part I: Theoretical Studies; Part II: Experimental Studies, Air Force Aero Propulsion Laboratory, Air Force Systems Command, Wright-Patterson Air Force Base, Ohio, AFAPL-TR-73-96, January 1974.
2. A. D. Gosman and W. M. Pun "The Calculation of Recirculating Flows," Imperial College Report HTS/74/2, 1974.
3. L. Krishnamurthy, Discussion and Verification of FREP Code, Report M/WPAFB/COMB/78-1, School of Mechanical Engineering, Purdue University, West Lafayette, Indiana, July 1978.
4. L. Krishnamurthy, Combustor Modeling Assessment Studies, UDR-TR-79-111, University of Dayton Research Institute, Dayton, Ohio, December 1979.
5. L. Krishnamurthy, Isothermal Flowfield Predictions of Confined Coflowing Turbulent Jets in an Axisymmetric Bluff-Body Near Wake, Aero Propulsion Laboratory, Air Force Wright Aeronautical Laboratories, Wright-Patterson Air Force Base, Ohio, AFWAL-TR-81-2036, May 1981.
6. G. J. Sturgess and S. A. Syed, "Widely-Spaced Co-Axial Jet Diffusion Flame Combustor: Calculation Using the Two-Equation Turbulence Model," AIAA-82-0113, AIAA 20th Aerospace Sciences Meeting, Orlando, Florida, January 1982.
7. L. Krishnamurthy, D. J. Wahrer, and H. S. Cochran, "On a Class of Confined, Isothermal, Recirculating Turbulent Flowfields Exhibiting Similarity," AIAA 8th Annual Minisymposium, Air Force Institute of Technology, Wright-Patterson Air Force Base, Ohio, March 1982.
8. G. J. Sturgess and S. A. Syed, "Multi-Specie Isothermal Flow Calculations of Widely-Spaced Co-Axial Jets in a Confined Sudden Expansion, With the Central Jet Dominant," AIAA-82-1136, AIAA/SAE/ASME 18th Joint Propulsion Conference, Cleveland, Ohio, June 1982.
9. W. M. Roquemore, R. P. Bradley, J. S. Stutrud, C. M. Reeves, and L. Krishnamurthy, "Preliminary Evaluation of a Combustor for Use in Modeling and Diagnostics Development," ASME-80-GT-93, Twenty-fifth Annual International Gas Turbine Conference, The American Society of Mechanical Engineers, New Orleans, Louisiana, March 1980.

10. A. J. Lightman, R. D. Richmond, P. D. Magill, L. Krishnamurthy, W. M. Roquemore, R. P. Bradley, J. S. Stutrud, and C. M. Reeves, "Velocity Measurements in a Bluff-Body Diffusion Flame," AIAA-80-1544, AIAA 15th Thermophysics Conference, Snowmass, Colorado, July 1980.
11. W. M. Roquemore, AFWAL/POSF, Private Communication, 1980.
12. AFWAL/POSF Centerbody Combustor, First Data Set, 1980.
13. H. C. Mongia, Garrett/AIRESEARCH, Private Communication, 1980.
14. R. W. Claus, NASA/Lewis Research Center, Private Communications, 1980-1981.
15. A. D. Gosman and F. J. K. Ideriah, "TEACH-T: A General Computer Program for Two-Dimensional Turbulent Recirculating Flows," Imperial College, Department of Mechanical Engineering Report, June 1976.
16. A. D. Gosman, E. E. Khalil, and J. H. Whitelaw, "The Calculation of Two Dimensional Turbulent Recirculating Flows," in Turbulent Shear Flows I, F. Durst, B. E. Launder, F. W. Schmidt and J. H. Whitelaw (Eds), pp. 237-255. Springer-Verlag, Berlin, 1979.
17. P. Hutchinson, E. E. Khalil, J. H. Whitelaw, and G. Wigley, "The Calculation of Furnace Flow Properties and Their Experimental Verification," J. Heat Transfer 98, 276-283, 1976.
18. P. Hutchinson, E. E. Khalil, and J. H. Whitelaw, "Measurement and Calculation of Furnace Flow Properties," J. Energy 1, 210-221, 1977.
19. E. E. Khalil and J. H. Whitelaw, "The Calculation of Turbulent Reacting Flows," Acta Astronautica 6, 1011-1015, 1979.
20. R. R. Craig, AFWAL/PORT, Private Communication, 1981.
21. R. D. Brum, L. M. Ikioka, and G. S. Samuelson, "Axial Flowfield Characteristics of Reacting and Nonreacting Flows in a Centerbody Configuration," WSS/CI 81-34, Fall Meeting of the Western States Section of the Combustion Institute, Tempe, Arizona, October 1981.

22. ibid., "Assessment of Candidate Combustor Configurations as Test Beds for Modeling Complex Flow," ASME-82-HT36, AIAA/ASME 3rd Joint Thermophysics, Fluids, Plasma, & Heat Transfer Conference, St. Louis, Missouri, June 1982.
23. G. S. Samuelson, Private Communication, July 1982.
24. S. V. Patankar and D. B. Spalding, "A Calculation Procedure for Heat, Mass and Momentum Transfer in Three-Dimensional Parabolic Flows," International Journal of Heat and Mass Transfer 15, pp. 1787-1806, 1972.
25. L. S. Caretto, A. D. Gosman, S. V. Patankar and D. B. Spalding, "Two Calculation Procedure for Steady, Three-Dimensional Flows with Recirculation," Third International Conference on Numerical Methods in Fluid Dynamics, Springer-Verlag, Berlin, pp. 60-68, 1972.
26. E. E. Khalil, "Numerical Computations of Turbulent Reacting Combustor Flows," in Numerical Methods in Heat Transfer, R. W. Lewis, K. Morgan, and O. C. Zienkiewicz (Eds.) pp. 489-509, 1981.
27. S. A. Syed and G. J. Sturgess, "Validation Studies of Turbulence and Combustion Models for Aircraft Gas Turbine Combustors," ASME Winter Annual Meeting, Chicago, November 1980.
28. B. E. Launder and D. B. Spalding, Mathematical Models of Turbulence, Academic Press, New York, 1972.
29. B. E. Launder and D. B. Spalding, "The Numerical Computation of Turbulent Flows," Comp. Meth. Applied Mech. and Engr. 3, 1974, pp. 269-289.
30. S. Elghobashi, "Studies in the Prediction of Turbulent Diffusion Flames," in Studies in Convection: Vol. 2, B. E. Launder (Ed.), pp. 141-189, Academic Press, New York, 1977.
31. S. V. Patankar, "Numerical Prediction of Three-Dimensional Flows," in Studies in Convection 1, B. E. Launder (Ed.), pp. 1-78, Academic Press, New York, 1975.
32. P. Bradshaw, "Effects of Streamline Curvature on Turbulent Flow," AGARDograph No. 169, 1973.
33. M. A. Leschziner and W. Rodi, "Calculation of Annular and Twin Parallel Jets Using Various Discretization Schemes and Turbulence-Model Variations," Trans. A.S.M.E., J. Fluids Engr. 103, 1981, pp. 352-360.

34. J. A. C. Humphrey and F. Pourahmadi, A Generalized Algebraic Relation for Predicting Developing Curved Channel Flow with a k- ϵ Model of Turbulence, Lawrence Berkeley Laboratory Report LBL-12009 Rev. June 1981.
35. R. M. C. So, Discussion on Reference 33, Trans. ASME, J. Fluids Engineering 104, pp. 263-265, 1982.
36. M. M. Gibson, "An Algebraic Stress and Heat-Flux Model for Turbulent Shear Flows with Streamline Curvature," Int. J. of Heat & Mass Transfer 21, pp. 1609-1617, 1978.
37. B. E. Launder, G. J. Reece, and W. Rodi, "Progress in the Development of a Reynolds-Stress Turbulence Closure," J. of Fluid Mechanics 68, pp. 537-566, 1975.
38. D. B. Spalding, "A Novel Finite-Difference Formulation for Differential Expressions Involving both First and Second Derivatives," Int. J. of Numerical Methods in Engineering 4, pp. 551-559, 1972.
39. A. K. Runchal, "Convergence and Accuracy of Three Finite-Difference Schemes for a Two-Dimensional Conduction and Convection Problem," Int. J. of Numerical Methods in Engineering 4, pp. 541-550, 1972.
40. S. V. Patankar, Numerical Heat Transfer and Fluid Flow, Hemisphere Publishing Corp., McGraw-Hill, New York, 1980.
41. S. V. Patankar, "A Calculation Procedure for Two-Dimensional Elliptic Situations," Numerical Heat Transfer 4, pp. 409-425, 1981.
42. N. Abramovich, The Theory of Turbulent Jets, M.I.T. Press, 1963.
43. Velocity Measurements in Confined Dual Coaxial Jets Behind an Axisymmetric Bluff Body: Isothermal and Combusting Flows, Aero Propulsion Laboratory, Air Force Wright Aeronautical Laboratories, Wright-Patterson Air Force Base, Ohio, AFWAL-TR-81-2018, April 1981.
44. N. W. M. Ko and W. T. Chan, "The Inner Regions of Annular Jets," J. Fluid Mech. 93, (3), pp. 549-554, 1979.
45. D. F. G. Durao, and J. H. Whitelaw, "Velocity Characteristics of the Flow in the Near Wake of a Disk," J. Fluid Mech. 85, (2), pp. 369-385, 1978.

46. S. Fujii and K. Eguchi, "A Comparison of Cold and Reacting Flows Around a Bluff-Body Flame Stabilizer," Trans. A.S.M.E. 103, pp. 328-334, 1981.
47. A. J. Lightman, P. D. Magill and R. J. Andrews, "Laser Diagnostic Development and Measurement and Modeling of Turbulent Flowfields of Jets and Wakes," Part II: Two-Dimensional Laser Doppler Anemometer Measurements of Isothermal Flowfields in a Ducted Centerbody Combustor. Aero Propulsion Laboratory, Air Force Wright Aeronautical Laboratories, Wright-Patterson Air Force Base, Ohio, AFWAL-TR-83-2044, June 1983.
48. R. P. Bradley, W. M. Roquemore, J. S. Stutrud, C. M. Reeves, and C. A. Obringer, "Second Data Set for APL Research Combustor," AFWAL/POSF, 1982.
49. W. M. Roquemore, AFWAL/POSF, Private Communication, June 1983.

END

FILMED

12483

DTIC